Universitat Politècnica de Catalunya
Departament d'Enginyeria Civil i Ambiental

A framework for 3D nonlinear analysis of reinforced concrete frames under general loading

Doctoral Program in Construction Engineering
Doctoral Thesis by:

Mauro Poliotti

Supervisors:

Prof. Jesús-Miguel Bairán García
Prof. Oscar Möller

Barcelona, September 2020

Summary

Modern guidelines for design and assessment of reinforced concrete structures under seismic and other extreme loads require nonlinear analysis. In particular, performance-based methods rely on a realistic representation of the structural behavior. The complex structural response can be obtained by means of three-dimensional finite element models, although its application is limited due to their high computational cost. Alternatively, if the structure can be assimilated by line elements, as it is the case of most structures composed by beams and columns, the structure can be simulated by means of frame elements. These formulations have demonstrated to be robust and efficient. The main drawback of most of the beam-column models, is that they neglect or consider in an oversimplified way the interaction between axial and transverse internal forces. Furthermore, they only take into account longitudinal reinforcement while they neglect or consider in an oversimplified way the presence of transverse reinforcements. Consequently, most frame models are not able to trace different failure modes in reinforced concrete elements such as shear or torsional failures. Besides, the simplifications made in those models affect also their ability to reproduce even common failure modes such as flexural or axial failures.

The main goal of this thesis is to develop a robust and efficient numerical tool capable of reproducing different failure modes of reinforced concrete frame elements. It is also desired that the model is able to reproduce complex phenomena such as passive confinement in an objective way for reinforced concrete elements of generic geometry and reinforcements. The developed tool is aimed to be used in the design or assessment of full scale structures under gen-

eral loading conditions. In order to accomplish this objective, the problem is dealt by means of a multilevel framework.

At the constitutive level, a new plastic-damage model for concrete that incorporates a variable dilatancy parameter is developed. It is demonstrated that dilatancy affects the free expansion of concrete, the softening behavior under shear stresses and the response of passively confined elements. The model is based on a well-known plastic-damage model which is modified by means of a dilatancy parameter that depends on the plastic-damage and stress states.

At the sectional level, a new model that introduces an efficient numerical technique is developed. The new model is based on a total interaction sectional model that reproduces the kinematic behavior of the cross-section by means of a two-component displacement field. One component of the displacements satisfies the traditional hypothesis of Euler-Bernoulli while the complementary field reproduces warping and distortion. This last field, enables the model to obtain the triaxial stress and strain tensors on each point of the cross-section domain. Thus, the interaction between all the possible internal forces is reproduced. Considering distortion enables the model to reproduce explicitly the contribution of transverse reinforcement in both the confinement and shear strength mechanisms. The complementary displacement field is obtained by considering the inter-fiber three-dimensional equilibrium. In order to do so, spatial discretization of the equations is required. The displacement field is expressed by means of a set of b-spline functions predefined on the cross-section domain. Thus, a significant reduction on the degrees of freedom involved on the cross section state determination is obtained compared against a finite element solution. This makes the model suitable of its implementation at the element level.

Further, at the element level a force-based formulation is used. The model strictly satisfies the equilibrium between nodal and sectional forces. On each integration point of the elements the higher order sectional model described earlier can be used to represent the sectional behavior. Alternatively, the sectional model can be used

only where high interaction of the internal forces is expected while on the remaining integration points, a classic fiber model can be used. In this way, it is possible to optimize the computational effort making the model suitable for large scale simulations. The models are implemented into an open-source collaborative finite element software focused on the nonlinear seismic analysis of structures.

The presented models are validated, both separately and jointly, by comparison of numerical results with experimental tests available in the literature. Validation includes a wide range of concrete strengths, reinforcing materials, section geometries and types and arrangements of reinforcements. Several loading conditions are simulated making emphasis on the ability of the model to represent different failure modes such as shear, torsion and coupled modes. A study of confinement of sections with generic geometry and different confining materials is carried out. Last but not least, the simulation of a real full-scale bridge is done to test the capabilities of the proposed model.

Finally, the conclusions of the present research, as well as recommendations for future works are drawn.

Keywords

Concrete plastic-damage model; Dilatancy; Confinement; Nonlinear sectional analysis; Reinforced concrete; B-splines; Shear; Torsion; Force-based element; OpenSees.

Acknowledgments

Once I read that a thesis is not about a particular topic but about the person who wrote it. I will allow myself to correct that phrase. A thesis is not about a particular topic but about the people that supported and encouraged the author during the process of the doctorate. Here, I will express my gratitude to all of them.

First of all I would like to thank my supervisors Prof. Jesús Bairán and Oscar Möller. I would like to thank to Prof. Bairán for his guidance and for sharing his knowledge with me during all this years. I want to thank Prof. Möller for being my mentor and for introducing me on the research world and to the field of nonlinear analysis of structures. Both of them are not only great teachers but also great persons.

I would like to express my gratitude the structural concrete research group at UPC. A special thank to Prof. Antonio Marí for his support and for sharing his passion to the profession. Also I would like to thank Prof. Eva Oller, to Ulric Celada and to Montserrat Bernaus . I would like to thank also to Noemi Duarte for her friendship.

I am grateful to all my friends, to those here and in Rosario, for their constant support. A special thank to those who have become my second family here in Barcelone and that have lived this dream at my side.

I want to thank my father Gabriel and my brother Nicolás for their unconditional love and support in all my projects. Also I want to express my gratitude to my family that encouraged me in every step of my life.

Finally, I would like to express my endless gratitude and my

love to my life partner Raquel who was at my side in all the ups and downs during all this years.

This thesis was carried out with the financial support of *Agència de Gestió d'Ajuts Universitaris i de Recerca* of the Catalan Government and the Social European Fund thorough the FI scholarship 2017-FI-00152.

Barcelona, September 2020
Mauro Poliotti

Contents

List of Tables

List of Figures

Chapter 1

Introduction and objectives

1.1 Motivation

In the last three decades, the structural engineering field has been in the course of modifying its design philosophy from a *deem-to-satisfy* procedure to a *performance-based-design* (PBD) philosophy. The first approach consists on a set of rigid prescriptions that the structure has to satisfy, for instance the strength design criterion where a structure is designed to provide a certain strength greater than the prescribed loads. Conversely, the PBD philosophy involves the satisfaction of certain performance objectives under different scenarios with different probabilities of occurrence. Performance objectives may be addressed in the form of serviceability conditions, strength criteria, damage states, economical conditions, among others.

The PBD approach can be applied to a broad range of design processes, in the particular case of structural engineering it has been first applied to the design of structures under extreme events like earthquakes or tsunamis. Nowadays, this philosophy is spreading to other types of loads and procedures. For example, in structural wind design or in the life-cycle assessment of existing structures.

In the case of seismic PBD, the way to comply with the performance objectives is through damage control. This implies that under certain conditions the structure is on the nonlinear range. Current guidelines and procedures for the design or assessment of

reinforced concrete structures require different types of nonlinear analysis of those structures. For instance, pseudo-static pushover or complex time-history analysis has to be made for several loading scenarios. An important aspect of the PBD philosophy is that it relies directly on a realistic representation of the structural behavior. This means that all the possible failure modes of the structure have to be taken into account.

Reproducing the nonlinear behavior of reinforced concrete structures while considering different failures modes is a challenging problem that can only be faced by means of complex numerical tools. Solid three-dimensional finite elements (FE) simulate the structural behavior obtaining the complete stress and strain tensors on each point of the structure. Furthermore, they consider explicitly the presence of longitudinal and transverse reinforcements and its interaction with concrete. In this way, solid FE models, if used with a robust constitutive model, are able to reproduce the coupling between all the internal forces as well as reproducing different failure modes such as shear, flexural, torsional and axial modes. The main disadvantage of this type of models is their high computational cost. Therefore, three-dimensional solid FE models are mostly used to study local effects in zones of load applications, beam-column connections, geometric discontinuities, among others.

Most of the structural elements such as beams, columns or bridge girders have one dimension much larger than the others. Therefore, they can be assimilated as line elements. One-dimensional elements such as beam-column elements are the most used among practicing engineers due to their robustness and their ease on the pre- and post-processing tasks. In addition, frame elements are closely related to the engineers reasoning and most of the current codes and provisions are oriented to the design or assessment of one-dimensional elements. Their ability to reproduce nonlinear behavior relies directly on the proper cross-sectional domain representation.

The sectional model integrates the material behavior of each point on the cross-section obtaining the internal forces, axial load,

bending moments, shear loads and torsion. The sectional model connects the material response with the element response. The most common and widely used sectional model is the so-called fiber model. It relies on the plane section hypothesis that obtains directly the longitudinal displacement of each fiber from the axial elongation and bending curvatures. Each fiber is characterized by its representative area and a uniaxial constitutive law. The fibers can represent concrete or steel material points. The fiber cross-sectional model is capable of capturing coupled axial and bending failure modes and also reproduces the interaction between concrete and longitudinal reinforcements. The main drawback of the cross-sectional fiber model is that it neglects the coupling between shear and axial forces. Consequently it is not capable of reproducing shear or torsional failure modes. Also, as it only considers explicitly the longitudinal reinforcements, it is not capable of reproducing confinement in an objective way. Several fiber frame elements have been proposed to incorporate shear or torsion failure modes. To do so, different approaches such as decoupled shear springs, or higher order sectional models have been followed. In the following chapter a review of these models is addressed.

The nonlinear response and the capability of reproducing different failure modes of both three-dimensional FE models or beam-column elements depend directly on the constitutive model used. In the case of shear or torsional failure modes, an important aspect of the material behavior is the accurate reproduction of softening under shear stresses.

The need of a robust frame model capable of reproducing different failure modes with the same level of accuracy as well as being able to reproduce other three-dimensional effects such as confinement in an objective way, motivated this work. This thesis presents the development of a new frame element. The problem is addressed at three levels: the frame element, the cross-sectional level and the concrete constitutive level.

1.2 Objectives

1.2.1 General objective

The main objective of this thesis is to develop a numerical tool capable of simulating the complex nonlinear response of three-dimensional reinforced concrete frame structures under general coupled loading and in both monotonic and cyclic conditions. It is aimed to capture different failures modes, such as shear, torsion, flexural and axial modes, without re-calibration of material parameters and with similar degrees of accuracy. It is desired to obtain a robust model suitable for the analysis of full scale structures that can be used in both the design or assessment process.

1.2.2 Specific objectives

In order to achieve the main goal of this thesis the work is carried out at three different levels: material, section and element models. The following set of specific objectives are stated:

- To develop a triaxial constitutive model for concrete, capable of tracing the nonlinear response of the material making emphasis on the shear softening and passive confinement behaviors.

- To develop a robust sectional model that reproduces the full coupling between the six internal forces in a general 3D case while considering explicitly the contribution of longitudinal and transverse reinforcement.

- To use a reduced number of degrees of freedom involved in the sectional computation in comparison with a finite element solution.

- To incorporate both the sectional and constitutive models into a force-base frame element that ensures equilibrium between nodal and sectional forces.

- To implement the models into a finite element program for the nonlinear dynamic or static analysis of structures.
- To evaluate the accuracy and capabilities of the proposed models.
- To study the behavior of reinforced concrete frame elements and structures under general loading conditions.

1.3 Research significance

The problem of capturing the complex nonlinear behavior of three-dimensional reinforced concrete structures under general coupled loading in monotonic or dynamic conditions has been investigated in this thesis. The problem is tackled in a multilevel level scheme: the element level, the sectional level, and the material level. Each one is addressed separately, in this way the frame formulation can include different sectional models within the same element to allow the optimization of the computational effort. Besides, the sectional model is formulated considering a general material, so the cross-sectional model may include not only concrete but also steel, fiber-reinforced-polymers (FRP), wood, composite materials, among other. Finally, the concrete model is a general multiaxial constitutive law that may be used in 3D finite element models.

In particular, at the constitutive level the concrete behavior under multiaxial stress states has been investigated making emphasis on the dilatant behavior. The proper representation of dilatancy proves to be essential as it affects the shear behavior as well as the transverse expansion of the material when submitted to compressive stresses. Hence, dilatancy also has great influence on passively confined elements. In this thesis, a new concrete material model that incorporates a variable dilatancy parameter is developed. At the sectional level, a new numerical integration technique is investigated in order to reduce the computational demand of a complete finite element solution. This approach allows a significant reduction on the degrees of freedom involved at the cross-sectional level

making the model more suitable for the analysis of full scale structures.

The main contribution of this thesis is the development of a new numerical tool that incorporates into a force-based frame element, complex sectional analysis and a three-dimensional constitutive law for concrete. Even though elements that incorporate different degrees of coupling between internal forces exists on the current literature, to the author knowledge none is capable of capturing different failure modes without recalibration of sectional or material parameters. Furthermore, the constitutive and sectional models are independently original contributions of this work.

1.4 Contents of the document

This thesis is divided into six chapters. The current introduction is the first of them. The second chapter consists on a brief review of the state of the art. Constitutive models for concrete are reviewed making emphasis on their ability to simulate multiaxial states. A review of fiber beam-column elements is presented highlighting their capabilities to reproduce coupled loading and different failure modes. Furthermore, current cross-sectional models that incorporate in different ways inter-fiber equilibrium are presented.

In the third chapter a new constitutive model for concrete is presented. The model is based on a plastic-damage formulation and incorporates a new evolutive dilatancy parameter. This is done to enhance the modeling of the transverse expansion of concrete under axial load which affects the behavior of passively confined concrete. Furthermore, dilatancy affects the softening shear behavior of the material. The evolution of dilatancy is made dependent on the plastic-damage and stress states. Validation of the model is carried out performing the simulation of experimental studies involving free expansion of concrete, passive confinement, and shear behavior of reinforced concrete elements.

Chapter four presents a new cross-sectional model that enhances the kinematics of the classic plane-section hypothesis by means of

a complementary displacement field that incorporates warping and distortion. This field is obtained by considering inter-fiber equilibrium which enables the model to capture the full coupling between all possible internal forces. The model incorporates both longitudinal and transverse reinforcements and their interaction with concrete mass. The numerical integration of the sectional model is made by means of a spatial discretization of the equations using b-spline functions defined on the cross-section domain. This numerical technique reduces significantly the number of degrees of freedom involved in the solution in comparison with a finite element model. The model is validated comparing the numerical response obtained with the proposed model against experimental results of reinforced concrete sections under different loading conditions.

In chapter five, a multilevel scheme for the analysis of reinforced concrete elements is presented. The sectional and constitutive models are incorporated to a force-based frame element. The joint use of these models constitutes the numerical tool developed in the thesis. The equilibrium at the element level is ensured by means of proper force interpolation functions, the inter-fiber equilibrium is considered at the sectional level and the constitutive model describes the material behavior. The proposed model is validated first at the element level by performing the simulation of beams and columns under monotonic and cyclic conditions. Finally to show the capabilities of the proposed framework, the nonlinear seismic analysis of a full scale bridge is made.

Finally, in chapter six a summary of the study is done and conclusions are drawn. In addition, recommendations for future researches that could lead to an improvement of the proposed models are addressed.

Chapter 2

State of the art

2.1 Frame elements

Frame finite elements are widely used because of their robustness, efficiency and their ease on the pre- and post-processes. Furthermore, they are directly related to the design or assessment processes as current guidelines and code procedures such as AASHTO (2011); ACI Committee 318 (2014); ACI Committee 341 (2007); EN CEN (2005); CEB-FIB (2010); CALTRANS (2019) are mostly oriented to frame structures.

Two beam theories stand out on the kinematic representation of line elements: the Euler-Bernoulli and Timoshenko beam theories. The first one, assumes that plain sections remain plane and orthogonal to the deformed axis of the element, in this way no shear deformations are considered. In the Timoshenko beam theory, the plane sections remain plane but not necessarily orthogonal, this leads to a simplified consideration of the shear deformations as it only reproduces a constant distribution of shear strains. Higher order theories have been also proposed, for instance in Reddy (1997); Reddy et al. (1997) a two and third order beam theories were proposed, using two and third order polynomials to approximate the shear strain profile.

In a finite element framework, frame elements can be formulated following two main approaches: displacement- or force-based

elements. Stiffness or displacement-based elements involve the use of predefined displacement interpolation functions that relate the nodal displacements with the inner element displacements. Equilibrium is verified in a weak form by means of the virtual work principle. On the other hand, flexibility or force-based elements consists on force interpolation functions that relate nodal forces with internal forces on each cross-section of the element, Roca et al. (1994, 1995). This approach ensures the equilibrium of the element while it only considers compatibility on a weak form. Neuenhofer, Filippou (1997); Scott et al. (2004) demonstrated that force-based formulations required fewer elements than displacement-based elements to adjust the nonlinear behavior of beams. Furthermore mixed elements have also been proposed which interpolate both displacement and force fields Lee (2008); Taylor et al. (2003); Saritas (2006); Saritas, Filippou (2009a).

Beam models can be also classified by how the nonlinear behavior is considered. Two main approaches exist: lumped and distributed models. The first one considers that the nonlinear behavior of the element is concentrated on discrete and predefined points, most usually on the elements ends Fenves, Filippou (2004). Distributed models consider that nonlinear behavior can take place on any point of the element and it can spread on the element length. In both cases, the nonlinear behavior can be represented by means of predefined moment-curvature relationships and envelopes. The main drawback of this approach is the calibration of the parameters of this type of models. Alternatively, the nonlinear response can be represented by numerical integration of the material behavior on the cross-section domain. Sectional models are detailed in the next section being the so-called fiber model the most common Spacone et al. (1996a); Taucer et al. (1991); Spacone et al. (1996b); Kang, Scordelis (1980); Mari (1984). There the sectional domain is discretized into fibers, each one is characterized by its area, position and its behavior is represented by means of a uniaxial constitutive law. These models, are able to trace the nonlinear response of elements that are mainly subjected to axial loads and bending

moments.

Force-based elements with distributed nonlinearity and fiber representation of the cross-section have shown to be robust and efficient in the nonlinear representation of structures that fail due to combination of axial load and bending moments Spacone et al. (1996a); Taucer et al. (1991); Spacone et al. (1996b); Kang, Scordelis (1980). Their main drawback is that the coupling between shear and axial internal forces is neglected. Thus, these models cannot reproduce other failure modes such as shear, torsion or coupled modes. The robustness of fiber-beam elements, and the increasing need of reproducing complex failure modes that involve the coupling between normal and tangential internal forces, have motivated researchers to extend the classical fiber-beam models to include different degrees of interaction between internal forces. Extended state of the art reviews can be found in Ceresa et al. (2007) and Bairán, Marí (2007b).

Different approaches have been followed to incorporate shear deformation to fiber-beam models. One way is to consider the nonlinear shear behavior uncoupled from the bending and axial responses, Marini, Spacone (2006); Ibarra et al. (2005). Alternatively, formulations that consider predefined shear stress or strain profiles Petrangeli et al. (1999); Petrangeli (1999); Papachristidis et al. (2010); Ceresa et al. (2009); Mazars et al. (2006); Gregori et al. (2007); Saritas (2006); Kagermanov, Ceresa (2018) have been proposed. These models have shown to be relatively simple and robust, their main drawback is that they neglect inter-fiber equilibrium during the analysis. This leads to difficulties when reproducing different failures modes in an objective way. Sectional models that consider the inter-fiber equilibrium have been also proposed and they are described in the following section.

2.2 Sectional models

Sectional models relate the material behavior of each point on the cross-sectional domain with the element level by means of numeri-

cal integration. Different sectional models have been proposed with different levels of accuracy and complexity. The most common method to represent the cross-section response is the so-called fiber model Spacone et al. (1996a); Taucer et al. (1991); Spacone et al. (1996b); Kang, Scordelis (1980); **?**. As it was previously mentioned, fiber models are able to reproduce the coupling between bending moments and axial load. Also they consider the interaction between concrete and longitudinal reinforcements. As they neglect the inter-fiber equilibrium, they are not able to reproduce coupling between shear and axial forces. Furthermore, as they neglect distortion and transverse equilibrium, they are not able to incorporate the presence of transverse reinforcements. Cross-sectional models based on inter-fiber equilibrium showed to be able to accurately reproduce different failure modes Bairán, Marí (2007b); Le Corvec (2012); Mohr et al. (2010); Di Re (2017). In the following, sectional models that considers inter-fiber equilibrium are addressed.

Vecchio, Collins (1988) developed a *dual-section analysis* for the case of 2D frame elements. The coupling between longitudinal and transverse stresses is obtained by explicitly considering the equilibrium between fibers, which involves the analysis of two adjacent cross-sections to approximate the longitudinal stress gradient. The dual-section model is a non-local model, as it needs information from adjacent points, so an ad-hoc element formulation is needed. To overcome this problem, Bentz (2000) introduced the *Longitudinal Stiffness Method*, where the longitudinal stress gradient was calculated locally considering equilibrium equations at the beam level. This method is a local sectional model, but only for 2D elements.

Later, Bairán, Marí (2006a,b, 2007a) presented a sectional model called TINSA (*Total Interaction Nonlinear Sectional Analysis*). It is based on the enhancement of the kinematic field of the Navier-Bernoulli theory by means of a *warping-distortion* displacement field which is obtained by solving the inter-fiber equilibrium in the section domain with a 2D FE model. The warping-distortion field considered is independent of the x-coordinate neglecting its varia-

tion along the beam length, this leads to a sectional model that is completely independent of the frame formulation, thus there is no need for additional degrees of freedom at the beam level. A consequence of this assumption is that the effect of non-uniform warping and shear lag effects are neglected, but this is relevant in thin-walled sections rather than in compact cross sections as is the case of most reinforced concrete beams and columns. This formulation proved to capture the interaction between the six possible internal forces in sections of any shape and takes into account both longitudinal and transverse reinforcements explicitly. Its main drawback is the higher computational demand compared with traditional beam models.

Mohr et al. (2010), presented a modification of the TINSA model for the case of 2D frames. The complementary displacement field is calculated as a weighted sum of Taylor's polynomials defined in the section height. This method avoids the FE solution, reducing the computational cost of the original model. The sectional model was implemented on a flexibility-based frame element and tested in beams with bending moment and shear. As it was developed for 2D frames, no torsion or bidirectional shear flows can be analyzed with this model.

Le Corvec (2012) and Di Re (2017) presented 3D frame elements based also on the displacement decomposition. As an additional hypothesis to the original formulation, they presented a complementary displacement field, which only produces warping neglecting the distortion of the cross-section. The out of plane displacement is obtained by interpolation over the section domain but also on the beam length, this allows the model to capture non-uniform warping and shear lag effects. As interpolation function over the cross section domain, Le Corvec (2012) used Lagrange's polynomials, while Di Re (2017) included Hermite's polynomials. Both models were implemented in 3D force-based elements based on the Hu-Washizu variational principle. These models can capture the interaction of the internal forces in a tri-dimensional element, but the hypothesis of considering a complementary field with only warping has the

drawback that distortion of the section is not captured, so transverse reinforcement is not considered explicitly. Besides, as the complementary field is interpolated on the beam length, a special frame formulation is developed with more degrees of freedom at the beam level that have to be considered or properly condensed.

2.3 Concrete constitutive models

Concrete behavior exhibits a wide range of non-linear phenomena: different responses under tension and compression, large differences in the peak strengths, anisotropy induced by cracking, damage due to the development of micro-cracks, irreversible strains, stiffness recovery upon loading reversals, dilatancy, enhancement in strength and ductility under the effect of confinement, rate dependency, among others.

A large variety of constitutive models for concrete is available on literature with different degrees of approximation and complexity. Most of them are formulated using one or a combination of approaches, such as nonlinear elasticity Elwi, Murray (1979), plasticity Simo et al. (1988); Chen (2007); Vermeer, de Borst (1983), damage or fracture mechanics Bažant, Gambarova (1984); Lemaitre (1985a); Mazars (1986); Bazant (1983); Bažant, Oh (1983); Luccioni, Oller (2003); Mazars et al. (2015); Faria et al. (2004); Červenka, Papanikolaou (2008), and empirically based models Mander et al. (1988b); Vecchio (1992, 1999); Vecchio, Collins (1982, 1988, 1986); Vecchio, Selby (1991).

Models with coupled plasticity and damage have shown to be able of reproducing the main characteristic of concrete behavior in a robust manner Lemaitre (1985b); Lubliner et al. (1989); Lee, Fenves (1998, 2001); Alfarah et al. (2017); Moharrami, Koutromanos (2016); ABAQUS (2012); Luccioni et al. (1996); Luccioni, Rougier (2005); Wu et al. (2006). However, they require especial calibration in those cases where dilatancy is important. For instance, the estimation of the shear strength in reinforced elements, and the simulation of passively confined elements.

In particular, dilatancy can be described as the volume change of a granular material when it is submitted to shear strains. This phenomenon plays an important role in the shear behavior of concrete as well as in the increase of strength and ductility due to confinement. This is why its proper representation becomes of especial interest in the evaluation of earthquake-resistant structures.

A coupled plastic-damage model for concrete was firstly introduced by Lubliner et al. (1989). There, the classical hardening variable of plasticity theory was replaced by a *plastic-damage* variable. This was defined as a measure of the energy dissipated during the inelastic process. In a tensile case the dissipated energy is the fracture energy, and in a compressive case is known as the crushing energy, see Coleman, Spacone (2001). Both energies are normalized to avoid mesh-sensitivity by means of a localization length, see Bazant (1983); Oliver (1989). The model introduced a new yield function and a stiffness degradation variable. The elastoplastic response and the stiffness degradation process were presented in a coupled manner. The single plastic-damage variable enabled the model to reproduce monotonic loading conditions.

Different variants of that model have been developed Lee, Fenves (1998, 2001); Alfarah et al. (2017); Moharrami, Koutromanos (2016); ABAQUS (2012); Luccioni et al. (1996); Luccioni, Rougier (2005); Wu et al. (2006). Furthermore, it has been applied to the simulation of reinforced concrete elements Saritas, Filippou (2009b); Genikomsou, Polak (2015); Earij et al. (2017); Nzabonimpa et al. (2017) showing its capabilities.

In particular, Lee, Fenves (1998, 2001) presented a modified version of the plastic-damage model in order to include cyclic loading. Two plastic-damage variables, one for tension κ_t and other for compression κ_c, were introduced. An isotropic stiffness degradation variable was also proposed. In this model, the elastoplastic and stiffness degradation responses (damage) were decoupled. In addition, the control of the tensile and compressive strengths was made by means of the plastic-damage variables. A non-associative flow rule was proposed to control the dilatancy by means of a linear

Drucker-Prager function.

This widespread model proved to be able to capture many of the main aspects of the concrete cyclic response. It reproduces plastic deformations, stiffness degradation, crack opening and closing, and different strengths in the tensile and compressive case. It has been implemented in commercial codes, such as ABAQUS (2012). However, the model controls dilatancy with a single parameter α_p which is held constant. A wide range of values for this parameter was used in literature.

In Lee, Fenves (1998), the effect of the α_p parameter in the free expansion of concrete was shown in a biaxial compressive test. It was shown that small values of α_p produced significantly smaller values of the out-of-plane strain. This implied that this parameter might need specific calibration for different applications.

One example where this was evidenced is in the research of Genikomsou, Polak (2015). There, the model was applied to the simulation of punching shear in reinforced concrete slabs. In order to fit the experimental data, a parametric study with different values of the dilatancy parameter was carried out. A strong influence in the shear strength and ductility was reported in that research.

Saritas, Filippou (2009b) simulated the effect of confinement in concrete specimens using the plastic-damage model. Simulations of reinforced concrete beams under both shear and bending were made in the same work. They reported difficulties in the assessment of the strength increase and the post-peak behavior of passively confined elements. To overcome this issue, calibration of the compressive fracture energy was made in that work.

In a different research, Earij et al. (2017) performed a parametric study of the dilatancy parameter in the simulation of reinforced concrete beams. A significant loss of ductility for lower values of α_p was shown.

Nzabonimpa et al. (2017) presented the simulation of concrete beam-column joints using the plastic-damage model. They reported that low values of the dilatancy parameter were not able to fit experimental results.

The need to overcome the previous reported difficulties with a consistent physical approach motivates a closer study of the dilatancy phenomenon.

Chapter 3

A new concrete plastic-damage model with an evolutive dilatancy parameter

Typical plastic-damage models for concrete use a constant dilatancy parameter. On problems sensitive to confinement and shear softening, this parameter needs ad hoc calibration to fit experimental observations. This makes the model not objective for general applications. To overcome this issue, in this chapter, a constitutive plastic-damage model with evolutive dilatancy is proposed for concrete. The evolution of dilatancy is made dependent on the plastic-damage and stress states. The proposed evolution law is validated by comparison of numerical simulations with available experimental results. The validation includes: concrete specimens under uniaxial compression measuring the free expansion, passively confined concrete specimens with different confining materials, and reinforced concrete panels under in-plane shear. It is concluded that the model accurately reproduces concrete lateral expansion through different nonlinear states. Proper modeling of concrete nonlinear expansion proves essential for capturing the response in a number of situations: softening under high shear stresses, confinement, and

ductility assessment.

3.1 Introduction

The assessment of existing structures requires simulation methods able to reproduce serviceability and safety conditions in a precise manner. In the case of reinforced concrete structures in seismic zones, material modeling of concrete is crucial for seismic performance assessment.

Within the same earthquake-resistant structure, there are elements under axial loads with high degrees of confinement and other elements with high shear demands. This requires of material models capable of reproducing a wide range of stress states in an objective manner.

Concrete behavior exhibits a wide range of non-linear phenomena: different responses under tension and compression, large differences in the peak strengths, anisotropy induced by cracking, damage due to the development of micro-cracks, irreversible strains, stiffness recovery upon loading reversals, dilatancy, enhancement in strength and ductility under the effect of confinement, rate dependency, among others.

In particular, dilatancy can be described as the volume change of a granular material when it is submitted to shear strains. This phenomenon plays an important role in the shear behavior of concrete as well as in the increase of strength and ductility due to confinement. This is why its proper representation becomes of especial interest in the evaluation of earthquake-resistant structures.

A large variety of constitutive models for concrete is available on literature with different degrees of approximation and complexity. Most of them are formulated using one or a combination of approaches, such as elasticity, plasticity, damage, and fracture mechanics. Models with coupled plasticity and damage have shown to be able of reproducing the main characteristic of concrete behavior

in a robust manner. However, they require especial calibration in those cases where dilatancy is important. For instance, the estimation of the shear strength in reinforced elements, and the simulation of passively confined elements.

This research focuses on the study of plastic-damage models for concrete, especially on the treatment of the dilatancy phenomenon. The development of a plastic-damage model with variable dilatancy for the objective simulation of elements in shear and under confinement is pursued in this chapter.

In the following, first a review of the main aspects of the classical plastic-damage model is made. Further, simulations and comparison with experimental data available in literature are carried out with different values of the dilatancy parameter. A novel plastic-damage model with variable dilatancy is proposed to improve the capabilities of the model. The validation of the proposed modifications is made by means of numerical simulation of experimental tests. Three experimental campaigns available in the literature which showed to be significantly affected by concrete dilatancy are reproduced. Finally, conclusions are drawn.

3.2 Plastic-damage model with constant dilatancy for concrete

3.2.1 Basic features

Plasticity theories are based in the decomposition of the strain tensor $\boldsymbol{\varepsilon}$ into elastic $\boldsymbol{\varepsilon^e}$ and plastic parts $\boldsymbol{\varepsilon^p}$, where only the elastic part of strains produces stresses.

$$\begin{aligned} \boldsymbol{\varepsilon} &= \boldsymbol{\varepsilon}^e + \boldsymbol{\varepsilon}^p \\ \boldsymbol{\varepsilon}^e &= \boldsymbol{E}^{-1}\boldsymbol{\sigma} \\ \boldsymbol{\sigma} &= \boldsymbol{E} : (\boldsymbol{\varepsilon} - \boldsymbol{\varepsilon}^p) \end{aligned} \tag{3.1}$$

where $\boldsymbol{E}$ is the elastic rank four tensor.

This formulation includes the definition of a single stiffness degra-

dation variable ($0 \leq D \leq 1$), which allows transformation between stresses and effective stresses $\bar{\boldsymbol{\sigma}}$ spaces. It represents the stiffness degradation process.

$$\begin{gathered} \bar{\boldsymbol{\sigma}} = \frac{1}{(1-D)} \boldsymbol{I} : \boldsymbol{\sigma} = \frac{1}{(1-D)} \boldsymbol{\sigma} = \boldsymbol{E}_0 : (\boldsymbol{\varepsilon} - \boldsymbol{\varepsilon}^p) \\ \boldsymbol{E} = (1-D)\boldsymbol{E}_0 \end{gathered} \tag{3.2}$$

being $\boldsymbol{I}$ the rank four identity tensor, and $\boldsymbol{E}_0$ the un-degraded elastic rank four tensor.

Evolution of the plastic strains is made by a flow rule defined through a plastic potential function Φ. The elastoplastic response is decoupled from the stiffness degradation, so the plastic evolution can be defined in the effective stress space as follows

$$\dot{\boldsymbol{\varepsilon}}^p = \dot{\lambda} \frac{\partial \Phi}{\partial \bar{\boldsymbol{\sigma}}} (\bar{\boldsymbol{\sigma}}) \tag{3.3}$$

where λ is the plastic consistency parameter.

Two additional internal variables, which are the plastic-damage in tension and compression $\boldsymbol{\kappa} = (\kappa_t, \kappa_c)$ are introduced to play the role of hardening variables. Their evolution law is given by

$$\dot{\boldsymbol{\kappa}} = \dot{\lambda} \boldsymbol{H} (\bar{\boldsymbol{\sigma}}, \boldsymbol{\kappa}) \tag{3.4}$$

where $\boldsymbol{H}$ will be defined later in Section 3.2.2.

The plasticity model is completed by a yield function. It is defined in the effective stress space and it depends on the plastic-damage variables which controls the evolution of the surface. The yield function can be written in a general form as

$$F (\bar{\boldsymbol{\sigma}}, \boldsymbol{\kappa}) \leq 0 \tag{3.5}$$

Finally, the Kuhn-Tucker and consistency conditions are used to represent the loading/unloading conditions as follows

$$\begin{gathered} \dot{\lambda} \geq 0 \\ \dot{\lambda} F = 0 \\ F \leq 0 \end{gathered} \tag{3.6}$$

3.2.2 Damage Variable

The plastic damage variable is defined as the relative measure of energy dissipated during an inelastic process. In a uniaxial process $\aleph$, which can be either tension or compression $\aleph \in (t, c)$, the strain-stress curves can be obtained. Assuming that the plastic strain-stress diagrams can be derived, the plastic-damaged variable is defined as follows

$$\kappa_{\aleph} = \frac{1}{g_{\aleph}} \int_0^{\varepsilon^p} \sigma_{\aleph} \left(\varepsilon^p\right) d\varepsilon^p \tag{3.7}$$

where $g_{\aleph}$ is the normalized total energy that can be dissipated during the inelastic process which is assumed to be finite.

$$g_{\aleph} = \int_0^{\infty} \sigma_{\aleph} \left(\varepsilon^p\right) d\varepsilon^p \tag{3.8}$$

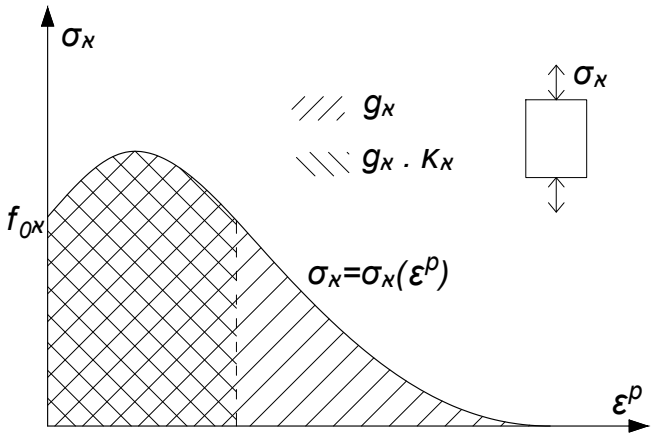

Figure 3.1: Uniaxial curve $(\sigma_{\aleph}, \varepsilon^p)$

The normalized total energy $g_{\aleph}$ is derived from the material properties: the fracture energy G_t, in the tension case, and its counterpart in the compression case G_c. Normalization is made by means of a characteristic length l_{ch} which is defined as the localization zone size. Extensive work has been made to overcome the mesh dependency problem Oliver (1989); Bazant (1976, 1983). As

a result, regularization can be made by relating the total energy, fracture energy and characteristic length through Eq. (3.9).

$$g_{\aleph} = \frac{G_{\aleph}}{l_{ch}} \tag{3.9}$$

Taking into account Eq.(3.7), the evolution of the plastic-damage variable in an uniaxial case can be written as follows

$$\dot{\kappa_{\aleph}} = \frac{1}{g_{\aleph}} f_{\aleph}\left(\kappa_{\aleph}\right) \dot{\varepsilon^{p}} \tag{3.10}$$

where $f_{\aleph}$ is the uniaxial strength function which is determined explicitly from $\kappa_{\aleph}$.

In the former, only uniaxial tension and compression cases were considered. To extend the model to multiaxial loading a scalar definition of the plastic-strain rate is given as:

$$\dot{\varepsilon^{p}} = \delta_{t\aleph}\, r\left(\hat{\bar{\boldsymbol{\sigma}}}\right) \hat{\dot{\varepsilon}}^{\,p}_{max} + \delta_{c\aleph}\left[1 - r\left(\hat{\bar{\boldsymbol{\sigma}}}\right)\right] \hat{\dot{\varepsilon}}^{\,p}_{min} \tag{3.11}$$

where δ is the Kronecker's delta, $\hat{\dot{\varepsilon}}^{\,p}_{max}$ and $\hat{\dot{\varepsilon}}^{\,p}_{min}$ are respectively the maximum and minimum eigenvalues of the plastic strain tensor.

The weight factor $r\left(\hat{\bar{\boldsymbol{\sigma}}}\right)$ in Eq.(3.11) depends on the eigenvalues of the effective stress tensor $\hat{\bar{\boldsymbol{\sigma}}}$ and its equal to zero for triaxial compression and equals to one for triaxial tension.

$$r\left(\hat{\bar{\boldsymbol{\sigma}}}\right) = \begin{cases} 0 & if\ \hat{\bar{\boldsymbol{\sigma}}} = \mathbf{0} \\ \dfrac{\sum_{i=1}^{3} \langle \hat{\bar{\sigma}}_i \rangle}{\sum_{i=1}^{3} |\hat{\bar{\sigma}}_i|} & otherwise \end{cases} \tag{3.12}$$

In which $\langle x \rangle = (x + |x|)/2$ is the Macaulay bracket function.

By substitution of Eq.(3.11) into Eq.(3.10) the evolution of the plastic-damage variables in a multiaxial load case is given by

$$\dot{\boldsymbol{\kappa}} = \boldsymbol{h}\left(\hat{\bar{\boldsymbol{\sigma}}}, \kappa\right) : \hat{\dot{\boldsymbol{\varepsilon}}}^{\boldsymbol{p}} \tag{3.13}$$

where

$$\boldsymbol{h}\left(\hat{\bar{\boldsymbol{\sigma}}},\kappa\right)=\begin{bmatrix} r\left(\hat{\bar{\boldsymbol{\sigma}}}\right)f_t\left(\kappa_t\right)/g_t & 0 & 0 \\ 0 & 0 & \left(1-r\left(\hat{\bar{\boldsymbol{\sigma}}}\right)\right)f_c\left(\kappa_c\right)/g_c \end{bmatrix} \tag{3.14}$$

Substituting the flow rule Eq.(3.3) into Eq.(3.13) the evolution of the plastic-damage variables can be rewritten as follows

$$\dot{\boldsymbol{\kappa}}=\dot{\lambda}\boldsymbol{h}\left(\hat{\bar{\boldsymbol{\sigma}}},\kappa\right)\cdot\frac{\partial\Phi}{\partial\hat{\bar{\boldsymbol{\sigma}}}}\left(\hat{\bar{\boldsymbol{\sigma}}}\right) \tag{3.15}$$

Finally comparing Eq.(3.15) and Eq.(3.4), $\boldsymbol{H}$ is defined as

$$\boldsymbol{H}=\boldsymbol{h}\left(\hat{\bar{\boldsymbol{\sigma}}},\kappa\right)\cdot\frac{\partial\Phi}{\partial\hat{\bar{\boldsymbol{\sigma}}}}\left(\hat{\bar{\boldsymbol{\sigma}}}\right) \tag{3.16}$$

3.2.3 Stiffness Degradation

The stiffness degradation due to micro-cracking is decoupled from the elastoplastic response and is represented using a single variable D. In cyclic loading cases, crack opening and closing causes the recovery of the stiffness when the load changes from tension to compression. However, stiffness is not recovered when the inverse load problem takes place; i.e., when load changes from compression to tension. To capture this phenomenon in ABAQUS (2012) the following definition of the stiffness degradation variable is made:

$$\begin{gathered} D=D\left(\bar{\boldsymbol{\sigma}},\boldsymbol{\kappa}\right)=1-\left[1-s_c\left(\bar{\boldsymbol{\sigma}}\right)D_t\left(\kappa_t\right)\right]\left[1-s_t\left(\bar{\boldsymbol{\sigma}}\right)D_c\left(\kappa_c\right)\right] \\ 0\leq\left(s_t,s_c\right)\leq 1 \\ s_t\left(\bar{\boldsymbol{\sigma}}\right)=1-w_t\ r\left(\hat{\bar{\boldsymbol{\sigma}}}\right) \\ s_c\left(\bar{\boldsymbol{\sigma}}\right)=1-w_c\left(1-r\left(\hat{\bar{\boldsymbol{\sigma}}}\right)\right) \end{gathered} \tag{3.17}$$

where D_t and D_c are the stiffness degradation variables in tension and compression, which are explicit functions of the corresponding plastic-damage variables. The stiffness recovery factors, w_t and w_c, control the crack opening and closing. In order to do so $w_t=0$ and $w_c=1$ are taken.

3.2.4 Yield Function

The yield function, known as the Barcelona Model, was first introduced by Lubliner et al. (1989). Then, it was further modified by Lee, Fenves (1998) to include the cyclic load case. It can be written under the following form in the effective stress space

$$\begin{aligned} F\left(\bar{\boldsymbol{\sigma}}, \boldsymbol{\kappa}\right) = & \frac{1}{1-\alpha}\left[\alpha \bar{I}_1 + \sqrt{3\bar{J}_2}\right. \\ & \left. + \beta\left(\boldsymbol{\kappa}\right)\left\langle \hat{\bar{\sigma}}_{max}\right\rangle - \gamma\left\langle -\hat{\bar{\sigma}}_{max}\right\rangle\right] - c_c\left(\boldsymbol{\kappa}\right) \leq 0 \end{aligned} \tag{3.18}$$

where $\bar{I}_1 = tr\left(\bar{\boldsymbol{\sigma}}\right)$, $\bar{J}_2 = \left(\bar{\boldsymbol{s}} : \bar{\boldsymbol{s}}\right)/2$, in which $\bar{\boldsymbol{s}}$ is the deviatoric effective stress, and $\hat{\bar{\sigma}}_{max}$ is the algebraically maximum effective stress .

The dimensionless constants α and γ are defined to control the yield surface shape. α is calculated to match the experimental enhancement in the yield stress that concrete exhibits in biaxial compression compared with the uniaxial case. In this work $\alpha = 0.12$ is set, as recommended in Lubliner et al. (1989). γ is calculated to give proper relation between the maximum octahedral radius in tension and compression, in this work it was taken as $\gamma = 3$, following the proposed value in Lubliner et al. (1989).

The β function adjusts the relation between the uniaxial strength in tension and compression and is calculated as

$$\beta = \frac{c_c\left(\boldsymbol{\kappa}\right)}{c_t\left(\boldsymbol{\kappa}\right)}\left(1-\alpha\right) - \left(1+\alpha\right) \tag{3.19}$$

where c_c and c_t are the compressive and tensile cohesion which are explicit functions of the internal variables $\boldsymbol{\kappa}$.

3.2.5 Plastic Potential

The non associative flow of the model presented by Lee, Fenves (1998) uses the linear version of the Drucker-Prager surface in the effective stress space as plastic potential surface

$$\Phi\left(\bar{\boldsymbol{\sigma}}\right) = \sqrt{2\bar{J}_2} + \alpha_p \bar{I}_1 \tag{3.20}$$

As this function exhibits singularities in the triaxial isotropic tension point, ABAQUS (2012) and Omidi, Lotfi (2010) used hyperbolic versions of the Drucker-Prager model to overcome this issue

$$\Phi\left(\bar{\boldsymbol{\sigma}}\right) = \sqrt{\left(\varepsilon_1 \alpha_p f_{t0}\right)^2 + 2\bar{J}_2} + \alpha_p \bar{I}_1 \tag{3.21}$$

where ε_1 is the eccentricity parameter, f_{t0} is the uniaxial tensile strength, and α_p is the dilatancy parameter which can be calculated as $\tan\left(\psi\right)$, being ψ the dilatancy angle.

The α_p parameter, is held constant during the whole analysis. This implies, as they are related, a constant dilatancy angle.

3.2.6 Numerical Integration

The numerical integration of the model is made following Lee, Fenves (2001) where the backward-Euler integration scheme is used. A spectral return-mapping algorithm was introduced producing an efficient integration of the model.

The tangent stiffness matrix is calculated numerically by the perturbation method as presented in Martinez et al. (2008). Central finite difference method is used instead of the forward one in order to improve convergence in the cyclic case.

3.2.7 Dilatancy control

The dilatancy of the plastic-damage model is controlled through the plastic potential function. A single and constant parameter α_p is used for this aim. It can be calculated as follows:

$$\alpha_p = \tan\left(\psi\right) \tag{3.22}$$

being ψ the dilatancy angle. A constant α_p implies a constant dilatancy angle.

Different values of the dilatancy parameter have been proposed in the literature. The tests performed by Lee, Fenves (1998) required a value of $\alpha_p = 0.2$. Similarly, Oller et al. (1988) recommended a maximum $\psi = 13°$ which is equivalent to $\alpha_p = 0.23$, hence it was consistent with the value used in Lee, Fenves (1998).

Later Genikomsou, Polak (2015), in their applications to model punching shear of reinforced concrete slabs, used a dilatancy angle of $\psi = 40°$ which is equivalent to $\alpha_p = 0.84$. This value is much bigger than the recommended in Lee, Fenves (1998); Oller et al. (1988); however, it was needed to capture the shear failure induced by punching.

Earij et al. (2017) applied the plastic-damage model to perform 3D simulations of reinforced concrete beams. A sensitivity analysis on this parameter was performed comparing results for $\psi = 20°,\ 30°,\ 40°,\ 50°$. The conclusion reported in that research was that low values of ψ produced a loss of ductility, so $\psi = 40°$ was chosen to fit experimental results.

Nzabonimpa et al. (2017), in their simulations of beam-column joints, used a dilatancy angle of $\psi = 56°$, equivalent to $\alpha_p = 1.48$, to conform the experimental observation in their specimens.

Saritas, Filippou (2009b), in the modeling of reinforced concrete beams and concrete specimens laterally reinforced, used a constant value of $\alpha_p = 0.2$. However, in order to adequate the response to the experimental data, these authors used different values of the compressive fracture energy for different amounts of transverse reinforcement. The value of the compressive fracture energy used for the biggest ratio of transverse reinforcement was four times bigger than the compressive fracture energy used in the unconfined concrete.

It can be seen that a wide range of values have been used in previous studies. Values between $\alpha_p = 0.2$ ($\psi = 13°$) and $\alpha_p = 1.48$ ($\psi = 56°$) have been used in the literature. The applications where only plain concrete was modeled tend to use lower values of the dilatancy parameter (α_p). While, the cases where interaction with reinforcements was simulated needed greater values to properly fit

the experimental results. This is inconsistent with the definition of a material parameter, which should be independent of the type of the load configuration.

3.2.8 Parametric analysis

To investigate the influence of the dilatancy parameter, three different types of tests are simulated and compared against experimental data available in literature. Simulations are carried out using the original plastic-damage model introduced by Lee, Fenves (1998, 2001), with four different values of the dilatancy parameter: $\alpha_p = 0.1,\ 0.2,\ 0.4$ and 0.6.

The first test belongs to an experimental campaign carried out by Osorio et al. (2017). There, a uniaxial monotonic compression tests was done measuring the transverse deformation, see Fig.(3.2). The second test is a passively confined concrete cylinder with a GFRP jacket under uniaxial monotonic loading tested by Aire (2002), see Fig.(3.3). The last experimental data set is obtained from a reinforced concrete panel subjected to in-plane shear tested by Vecchio, Collins (1982), see Fig.(3.4).

By analyzing the numerical results, several remarks can be made. It is noteworthy that each test is best fitted with a different value of the dilatancy parameter. In the first test, low values of α_p underestimate the post-peak transverse strains, while greater values tend to overestimate transverse strains near the peak. The dilatancy parameter that, on average, best fits the experimental data is $\alpha_p = 0.4$. In the second test, where passive confinement is provided, a value of $\alpha_p = 0.1$ is needed to adjust the experimental results. Finally, in the third test, the value that is needed to capture the shear strength is $\alpha_p = 0.6$. Low values of the dilatancy parameter underestimate the shear strength.

One phenomenon that introduces disagreement between experimental and simulation is the presence of confinement. A confining pressure tends to reduce the effect of the dilatancy in concrete Osorio et al. (2017). Thus, the cases where passive confinement is

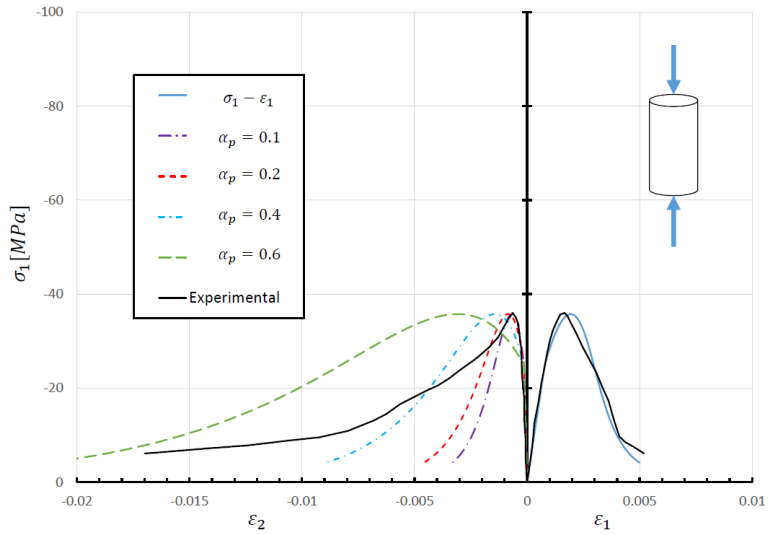

Figure 3.2: Longitudinal stress σ_1 vs. longitudinal ε_1 and transverse ε_2 strains - Uniaxial Test. Experimental results by Osorio et al. (2017)

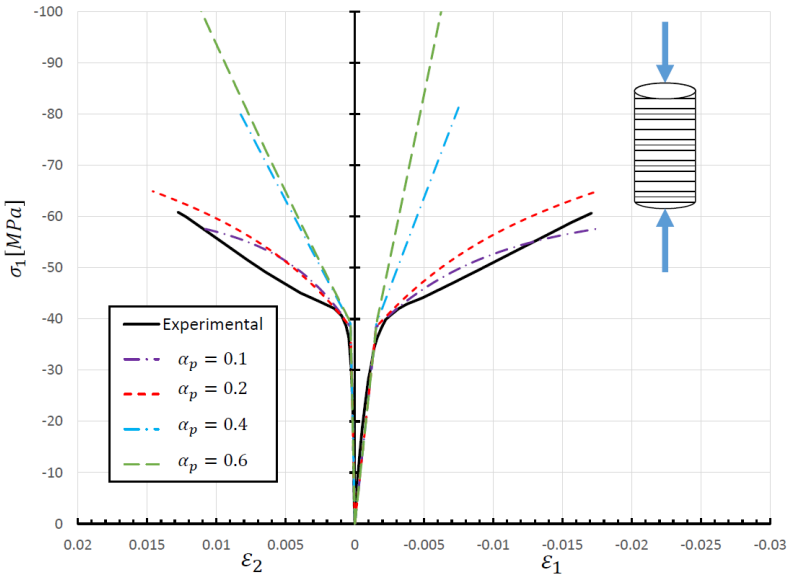

Figure 3.3: Longitudinal stress σ_1 vs. longitudinal ε_1 and transverse ε_2 strains - Uniaxial Confined Test. Experimental results by Aire (2002)

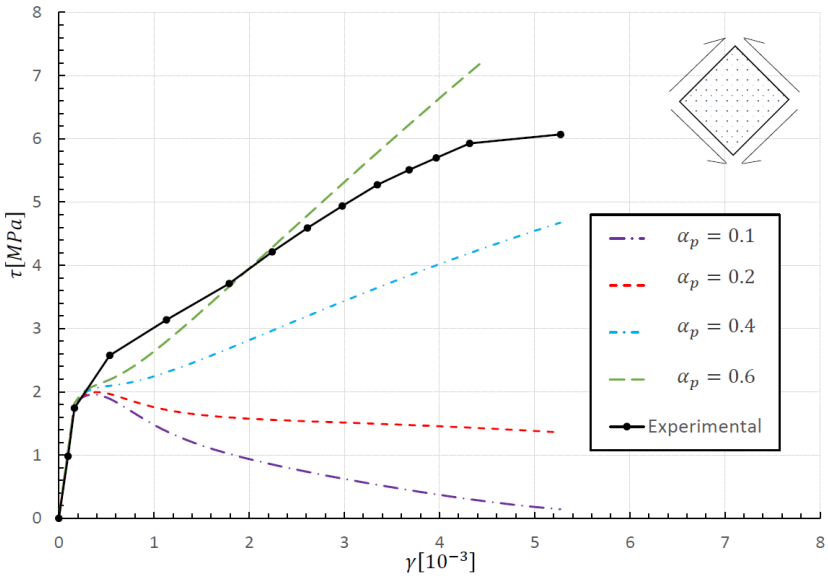

Figure 3.4: Shear stress τ vs. shear strain γ - Shear Panel Test. Experimental results by Vecchio, Collins (1982)

present are strongly dependent on the dilatancy parameter. Such dependence can be explained because small changes in the transverse expansion may cause variations on the confining pressure and consequently on the dilatancy. Another source of difference results from the evolution of damage. In the shear dominant cases, damage occurs in both tensile and compressive directions. This produces a quick evolution of the concrete expansion and, consequently, large values of the dilatancy parameter are needed.

As commented above, in previous researches, ad hoc calibration of this parameter was needed for different loading cases. This leads to a loss of objectivity that needs to be reviewed. In addition, it can be seen that a constant parameter is not consistent with the experimental evidence.

3.3 Proposed model

The evolution of dilatancy in inelastic processes has been studied before in the field of soils and rock mechanics Alejano, Alonso

(2005); Rahjoo, Eberhardt (2016); Detournay (1986); Zhao, Cai (2010). Nevertheless, when it comes to concrete, studies are scant. Some models exist focusing on the effect of variable volumetric expansion due to dilation Pantazopoulou, Mills (1995); Pantazopoulou (1995); Moharrami, Koutromanos (2016). However, to the knowledge of the author, the role in the shear strength and other structural performances has not been investigated.

Vermeer, de Borst (1983) proposed a dilatancy angle that depends on plastic strains. Oller et al. (1988) introduced an explicit function of plastic-damage variables to control the evolution of the dilatancy angle. In the case of rock mechanics, Detournay (1986); Alejano, Alonso (2005); Zhao, Cai (2010); Rahjoo, Eberhardt (2016) reported that the dilatancy parameter not only depends on the plastic state but also depends on the stress state, especially on confining stresses.

Based on the previous review and on the parametric analysis performed in section 3.2.8, it can be concluded that the dilatancy phenomena is affected by the confining pressure and the plastic-damage state. In consequence, the dilatancy angle is here proposed to be an explicit function of the plastic-damage and stress states. Taking into account Eq.(3.22), the α_p parameter can be written, in general terms, as follows, see Eq.(3.23).

$$\alpha_p = \alpha_p\left(\boldsymbol{\kappa}, \bar{\boldsymbol{\sigma}}\right) = \tan\psi\left(\boldsymbol{\kappa}, \bar{\boldsymbol{\sigma}}\right) \tag{3.23}$$

In the following, the evolution of the dilatancy angle proposed in this work is presented. First, the evolution of the dilatancy parameter with the plastic-damage state will be addressed independently of the stress state. Later, the effect of stresses on the dilatancy angle will be presented.

3.3.1 Evolution with the plastic-damage state

The plastic-damage state of the material is expressed through two variables, one for tension κ_t and other for compression κ_c. Both are defined for uniaxial processes. In order to establish the evolution

law, first, the definition of a plastic-damage variable for multiaxial states needs to be defined. In order to develop this task, the following physical aspects should to be taken into account.

The effect of dilatancy is greater and evolves quickly in those cases where the material is subjected to shear stresses, as in Fig.(3.4). Further, on an hypothetical case where the material is first damaged in tension and then subjected to compression, dilatancy would evolve quicker than in a pure compressive case. This is due to the development of microcracks in tension. When compression is later applied, the microcracks cannot be perfectly closed because the surface of the cracks had suffered small displacements. This increases the dilatancy and the volumetric expansion.

Bearing in mind the mentioned behavior, a scalar plastic-damage variable k_m for multiaxial cases is proposed, see Eq.(3.24)

$$(1-\kappa_m) = [1-\{1+\eta\ r\,(\bar{\boldsymbol{\sigma}})\}\ \kappa_t]\cdot[1-\{1-r\,(\bar{\boldsymbol{\sigma}})\}\ \kappa_c] \qquad (3.24)$$

where η is a constant which value is set equal to 20 to give more importance to the tensile plastic-damage. This factor is proposed to fit experimental data. $r\,(\bar{\boldsymbol{\sigma}})$ is the weight factor defined in Eq.(3.12).

In triaxial compression, the variable defined in Eq.(3.24) is equal to $\kappa_m = 1-(1-\kappa_t)(1-\kappa_c)$. It can be seen that it takes into account the previous tensile plastic-damage.

The evolution of the dilatancy angle can be explained by considering concrete as a granular material. During inelastic processes, particles slide past each other on the surface of microcracks. This increases both the internal friction and the total volume. Thus, the evolution of the dilatancy angle ψ is related to the evolution of the internal friction angle ϕ. The following evolution for both angles is proposed as in Oller et al. (1988), see Eqs.(3.25) and (3.26).

$$\psi = \begin{cases} 0 & if\ \phi \leq \phi_{cv} \\ \arcsin\left(\dfrac{\sin\phi - \sin\phi_{cv}}{1 - \sin\phi \sin\phi_{cv}}\right) & if\ \phi > \phi_{cv} \end{cases} \tag{3.25}$$

$$\sin\phi = \begin{cases} \dfrac{2\sqrt{\kappa_m}}{1+\kappa_m} \sin\phi^{peak} & if\ \ \kappa_m \leq 1 \\ \sin\phi^{peak} & if\ \kappa_m > 1 \end{cases} \tag{3.26}$$

where ϕ^{peak} and ψ^{peak} are the values of the dilatancy and friction angles when the material is fully damaged. ϕ_{cv} is the internal friction angle at constant volume and is calculated as in Eq.(3.27). It can be interpreted as the value of the friction angle when dilatancy begins.

$$\sin\phi_{cv} = \frac{\sin\phi^{peak} - \sin\psi^{peak}}{1 - \sin\phi^{peak}\sin\psi^{peak}} \tag{3.27}$$

The proposed evolution of the dilatancy parameter with the plastic-damage variable is plotted in Fig.(3.5).

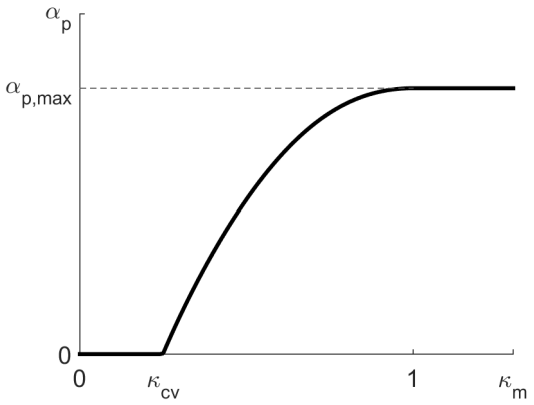

Figure 3.5: Dilatancy parameter vs. damage

In soils, dilatancy at early stages has a negative value, but this effect is not evidenced in concrete Vermeer, de Borst (1983). First, the dilatancy parameter remains equal to zero until plastic-damage

reaches the value of κ_{cv}. This is the value of the plastic-damage variable at constant volume when $\phi = \phi_{cv}$. Later, α_p increases up to its maximum value $\alpha_{p,max} = \tan \psi^{peak}$ when the material is fully damaged $\kappa_m = 1$.

Up to this point, the dilatancy parameter depends only on the plastic-damage state. The evolution is controlled by two parameters ψ^{peak} and ϕ^{peak}. In Oller et al. (1988), they were considered as constant material properties. In the current research, it is proposed to vary ψ^{peak} and ϕ^{peak} as a function of the stress state, to consider the effect of confinement.

3.3.2 Influence of the stress state

The experimental observations indicates that the presence of confinement reduces significantly the effect of dilatancy, as it was shown in section (3.2.8). Further, the maximum dilatancy is observed in the cases dominated by high shear stresses.

Therefore, in this research, it is proposed to affect the peak values of the internal friction and dilatancy angles by a term that depends on the stress state, see Eqs.(3.28) and (3.29).

$$\phi^{peak} = \phi^{peak}\left(\bar{\boldsymbol{\sigma}}\right) = \phi^{max} e^{-a(1+b)\ \bar{I}_1} \tag{3.28.1}$$

$$\psi^{peak} = \psi^{peak}\left(\bar{\boldsymbol{\sigma}}\right) = \psi^{max} e^{-a(1+b)\ \bar{I}_1} \tag{3.28.2}$$

$$a = \frac{1}{f_c}\ ;\ b = \frac{\bar{I}_1}{\sqrt{3\bar{J}_2}} \tag{3.29}$$

where ϕ^{max} and ψ^{max} are material properties and are the maximum internal friction and dilatancy angles, respectively. f_c is the uniaxial concrete strength. A similar term was proposed by Moharrami, Koutromanos (2016) to modify the evolution of plastic-damage variables in presence of confinement. Here, it is used to modify the dilatancy and internal friction peak angles.

It can be seen that in the isotropic compression and tension cases, the exponent in Eq.(3.28) is not defined. However, in the

compressive direction this is not relevant as the yield function is open in the hydrostatic axis. In the isotropic tensile point, the exponential term is taken equal to one to overcome this issue.

In Fig.(3.6) three curves are plotted for the evolution of the dilatancy parameter. Each one corresponds to a theoretical process for different degrees of constant confinement.

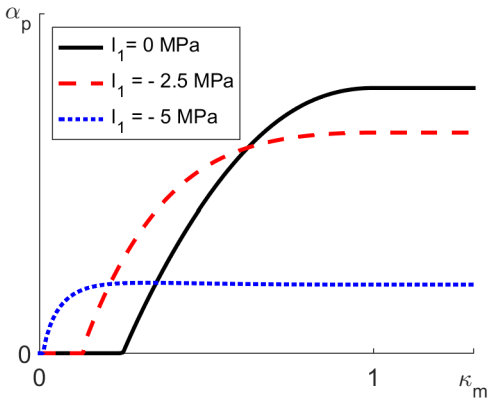

Figure 3.6: Dilatancy parameter vs. damage for different confining pressures

As can be observed in Fig.(3.6), in the proposed model, the presence of a higher confinement produces a reduction on the peak value of the dilatancy parameter. Moreover, it produces an early onset of dilatancy.

3.4 Validation

The proposed model is validated by the simulation of three different sets of experimental data which are representative of very different failure modes.

The first set consists in uniaxial compressive tests of concrete cylinders performed by Osorio et al. (2017). Four different concrete mixes were used from normal to high strength concrete. The transverse strains were measured in order to study the free expansion of the unconfined concrete.

The second experimental campaign, performed by Aire (2002), involves six uniaxial compressive tests of concrete cylinders passively confined by different types of FRP jackets. Three different amounts of transverse reinforcements were tested using glass and carbon fibers. As FRP do not show yielding stress, modeling the confinement response is more sensitive to the adequate simulation of concrete expansion than in the case of steel confinement reinforcement.

Finally, fifteen reinforced concrete panels, tested by Vecchio, Collins (1982), are simulated. The panels were subjected to in-plane shear, and each one had different amounts of reinforcement as well as different concrete strengths.

The material parameters in the three tests are obtained from available data. If a material parameter is not reported in the original publication then, the corresponding value is estimated using Eqs.(3.30) as recommended in Alfarah et al. (2017); CEB-FIB (2010).

$$E = 10000\left(0.8 + 0.2\frac{f_c+8}{88}\right)\sqrt[3]{f_c+8} \qquad [MPa] \qquad (3.30.1)$$

$$f_t = 0.302{f_c}^{2/3} \qquad [MPa] \qquad (3.30.2)$$

$$G_t = 0.073{f_c}^{0.18} \qquad [N/mm] \qquad (3.30.3)$$

$$G_c = \left(\frac{f_c}{f_t}\right)^2 G_t \qquad [N/mm] \qquad (3.30.4)$$

$$\nu = 0.2 \qquad (3.30.5)$$

The calibration of the stiffness degradation response is made by means of the two following material parameters.

$$\bar{D}_c = 0.423\left(1 - \frac{f_c}{\varepsilon_0 E}\right) \;;\; \bar{D}_t = 0.5 \qquad (3.31)$$

where $\bar{D}_c$ is the value of the stiffness degradation at the maximum compressive stress f_c, and ε_0 is the peak strain. The constant on the first expression in Eq.(3.31) is obtained from cyclic com-

pressive tests in Osorio et al. (2017). The tensile counterpart $\bar{D}_t$, is defined as the stiffness degradation at a stress equals to the half of the maximum tensile stress.

The values of the maximum internal friction and dilatancy angles in Eq.(3.28) control the evolution of dilatancy. The following values are used in all the simulations.

$$\phi^{max} = 65^\circ \; ; \; \psi^{max} = 32^\circ \tag{3.32}$$

3.4.1 Unconfined concrete

In this section, four concrete mixes, with different values of strength, are numerically tested and compared against experimental data from Osorio et al. (2017). The parameters, based on the material properties models shown in the set of Eqs.(3.30) and (3.31) are determined from the compressive strength of each test : $f_c = 35,\ 45,\ 60$ and $80\ MPa$. The characteristic length is set as $l_{ch} = 175\ mm$, which is obtained as the cubic root of the volume of the test sample.

Figure (3.7) presents experimental and numerical results for each one of the concrete mixes. Two numerical curves are traced, one obtained with the original model of Lee, Fenves (1998, 2001) with a constant dilatancy parameter equal to $\alpha_p = 0.2$, and the other calculated with the proposed model. In Fig.(3.7), ε_1 and σ_1 are the strain and stress in the load direction respectively, and ε_2 is the transverse strain.

It can be observed, in Fig.(3.7), that a fine agreement between numerical and experimental results is obtained with the proposed model. Particularly, it should be noticed that the lateral expansion, represented by ε_2, is well traced by the proposed model while the constant dilatancy control model underestimates the transverse strains. The main differences appear in the case of high strength concrete ($f_c = 80\ MPa$), where the experimental data presents a snap-back behavior after the peak load, which is not manifested in the simulation. However, considering the complexity of the control

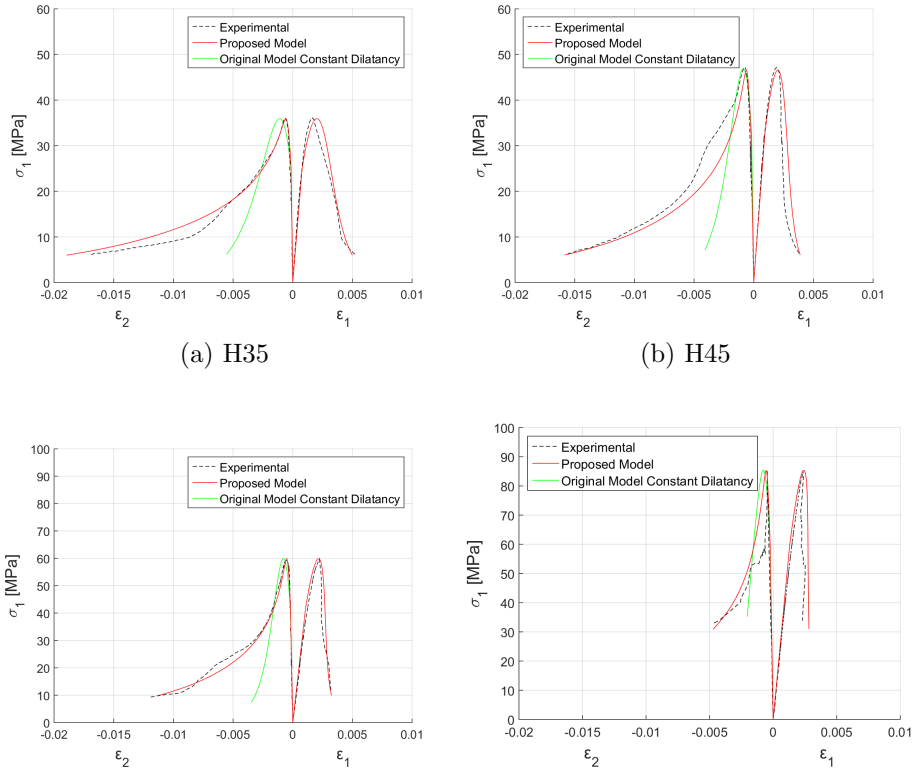

(a) H35 (b) H45

(c) H60 (d) H80

Figure 3.7: $\sigma_1 - \varepsilon_1$ and $\sigma_1 - \varepsilon_2$ curves for different concrete mixes. Experimental results by Osorio et al. (2017)

of the test, particularly in the case of high strength specimens as reported in Osorio et al. (2017), this difference is considered acceptable.

3.4.2 Confined concrete with different confining materials

The simulation of six passively confined concrete specimens is presented in this section. The transverse reinforcement consists of glass and carbon FRP jackets using 1, 3 or 6 plies of each material. Jackets are simulated in this validation by means of its transverse reinforcement ratios in the direction transverse to the load applica-

tion, as can be seen in the equilibrium equation (3.33).

$$\sigma_{tr} + \rho_r \sigma_r = 0 \tag{3.33}$$

where σ_{tr} is the transverse stress in concrete, ρ_r is the reinforcement ratio, which, in the case of jackets, is calculated as its thickness divided by the radius of the concrete specimen. σ_r is the stress in the reinforcement. Perfect bond is assumed between the jacket and the concrete mass.

Material properties of the GFRP and CFRP reported in Aire (2002) are summarized in Table 3.1.

	e [mm]	E [GPa]	f_u [GPa]
Glass	0.149	65	3.0
Carbon	0.117	240	3.9

Table 3.1: FRP properties of 1 ply

The concrete properties used in the six tests were determined from Eqs. (3.30) and (3.31) using $f_c = 42\ MPa$ and $\varepsilon_0 = 0.00239$. The deformation modulus of concrete is taken as $E = 25\ GPa$, as reported in Aire (2002). The characteristic length for the CFRP specimens is $l_{ch} = 20\ mm$, while in the case of GFRP $l_{ch} = 10\ mm$ is used. Both values correspond to the base length of the strain gauges used to measure transverse strains in the physical test.

Fig.(3.8) compares the numerical and experimental results, obtained for each confinement material and for the different amounts of confining reinforcement.

It can be seen that the enhancement in both strength and ductility of the passively confined specimens is well captured. In the case of GFRP jackets, a 5-8 % loss of strength is predicted by the model. The main differences appear in the case of CFRP with 3 layers of reinforcement, where transverse strain is overestimated. The confined strength is adequately captured in all the cases.

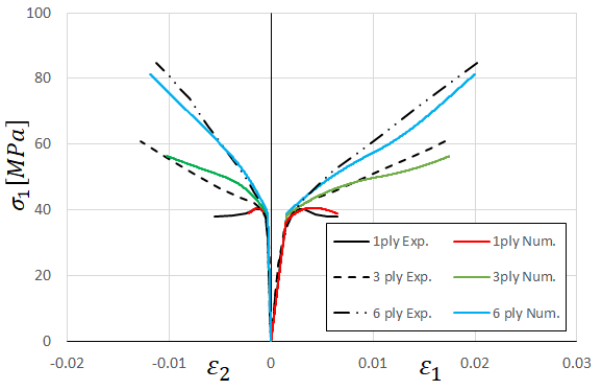

(a) GFRP

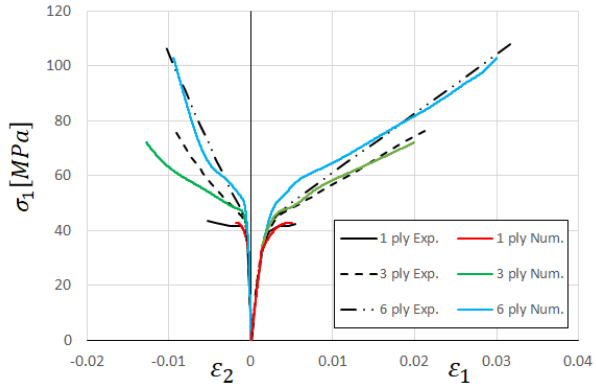

(b) CFRP

Figure 3.8: $\sigma_1 - \varepsilon_1$ and $\sigma_1 - \varepsilon_2$ curves for (a) Glass and (b) Carbon FRP jackets. Experimental results by Aire (2002)

3.4.3 Shear tests

In this section, fifteen reinforced concrete panels subjected to pure in-plane shear load, with different amounts of reinforcement and concrete strengths, are numerically reproduced. These panels belong to a larger experimental campaign Vecchio, Collins (1982) that included specimens under combined axial and shear loads. Here, only the pure shear tests are considered to study the effect of dilatancy in the predicted shear capacity of the proposed model.

The longitudinal and transverse reinforcement are included by means of the corresponding reinforcement ratios, similarly as in Eq.(3.33). The transverse reinforcement ratio is considered as elastic-

perfectly plastic and perfectly bonded to the concrete mass. Ratios and yield stress of the reinforcement steel as well as the concrete properties are summarized in Table 3.2.

Panel	f_c[MPa]	ε_0	f_{yl}[MPa]	ρ_l	f_{yt}[MPa]	ρ_t
PV3	26.6	0.0023	662	0.00483	662	0.00483
PV4	26.6	0.0025	242	0.01056	242	0.01056
PV6	29.8	0.0025	266	0.01785	266	0.01785
PV9	11.6	0.0028	455	0.01785	455	0.01785
PV10	14.5	0.0027	276	0.01785	276	0.00999
PV11	15.6	0.0026	235	0.01785	235	0.01306
PV12	16	0.0025	469	0.01785	269	0.00446
PV13	18.2	0.0027	248	0.01785	-	0
PV16	21.7	0.002	255	0.0074	255	0.0074
PV18	19.5	0.0022	431	0.01785	412	0.00315
PV19	19	0.00215	458	0.01785	299	0.00713
PV20	19.6	0.0018	460	0.01785	297	0.00885
PV21	19.5	0.0018	458	0.01785	302	0.01296
PV22	19.6	0.002	458	0.01785	420	0.01524
PV27	20.5	0.0019	442	0.01785	442	0.01785

Table 3.2: Panels reinforcement ratios and material properties

The material parameters are calculated using Eqs.(3.30) and (3.31). In panels PV3, 4, 6, 9, 11 and 16, the tensile strength is determined using the following expression suggested in the original publication Vecchio, Collins (1982)

$$f_t = 0.33\sqrt{f_c} \tag{3.34}$$

The characteristic length used in the tests is $l_{ch} = 140\ mm$, which corresponds to the cubic root of the measured volume.

Figures (3.9) to (3.23) present the results of the fifteen panels. For each panel, three curves are shown in each figure: the shear stress-strain $\tau - \gamma$, the normalized principal compressive stress-strain $\sigma_d/f_c - \varepsilon_d/\varepsilon_0$ and the normalized principal tensile stress-strain $\sigma_{dt}/f_t - \varepsilon_{dt}$. Numerical results are obtained with the proposed model and with the original model by Lee, Fenves (1998, 2001) with a constant dilatancy parameter equal to $\alpha_p = 0.2$.

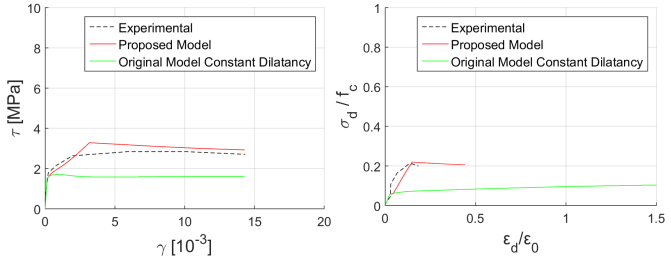

(a) Shear (b) Principal compression

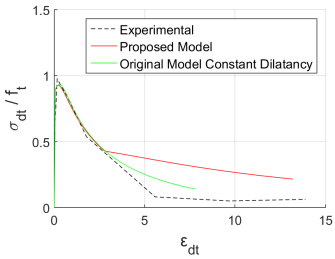

(c) Principal tension

Figure 3.9: Stress-strain plots of panel PV4. Experimental results by Vecchio, Collins (1982)

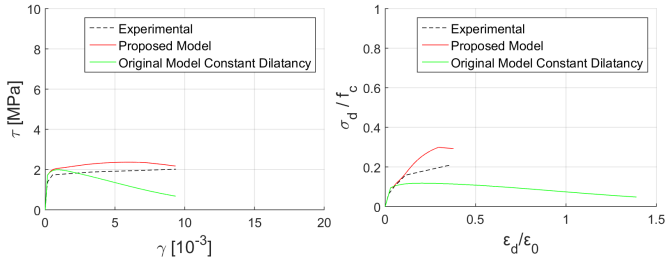

(a) Shear (b) Principal compression

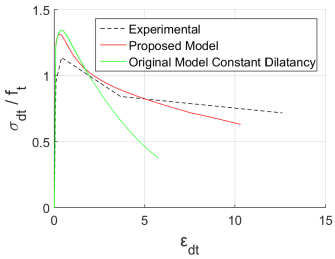

(c) Principal tension

Figure 3.10: Stress-strain plots of panel PV13. Experimental results by Vecchio, Collins (1982)

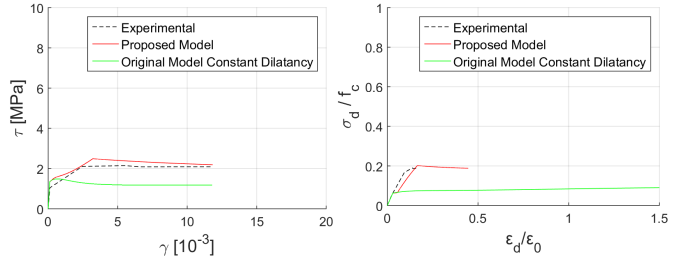

(a) Shear (b) Principal compression

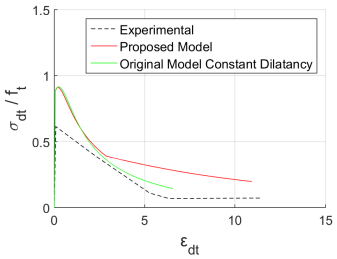

(c) Principal tension

Figure 3.11: Stress-strain plots of panel PV16. Experimental results by Vecchio, Collins (1982)

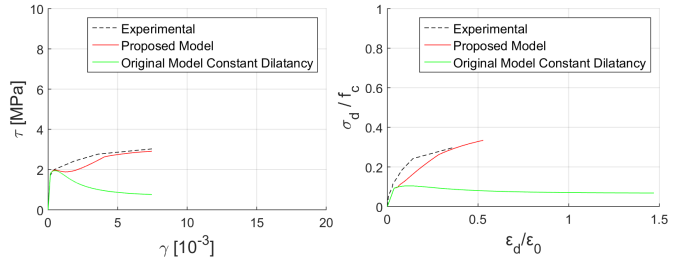

(a) Shear (b) Principal compression

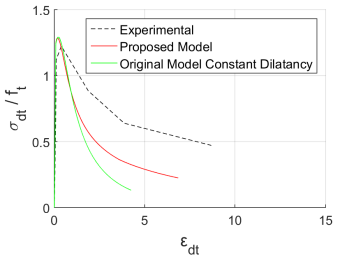

(c) Principal tension

Figure 3.12: Stress-strain plots of panel PV18. Experimental results by Vecchio, Collins (1982)

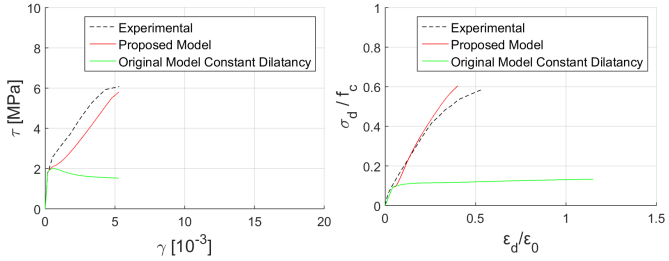

(a) Shear (b) Principal compression

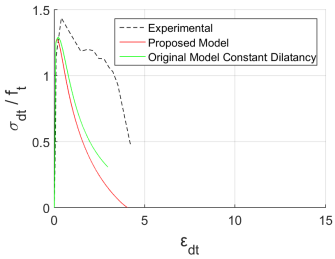

(c) Principal tension

Figure 3.13: Stress-strain plots of panel PV22. Experimental results by Vecchio, Collins (1982)

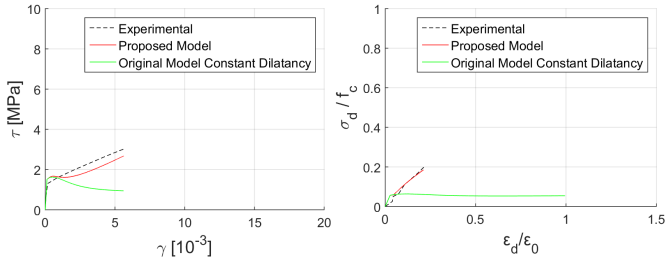

(a) Shear (b) Principal compression

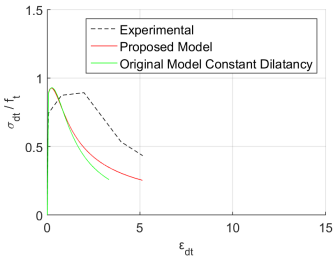

(c) Principal tension

Figure 3.14: Stress-strain plots of panel PV3. Experimental results by Vecchio, Collins (1982)

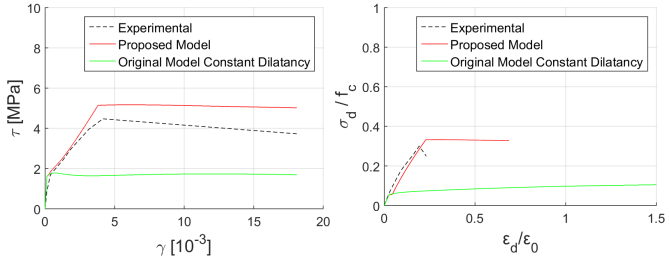

(a) Shear (b) Principal compression

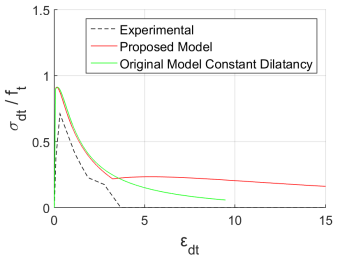

(c) Principal tension

Figure 3.15: Stress-strain plots of panel PV6. Experimental results by Vecchio, Collins (1982)

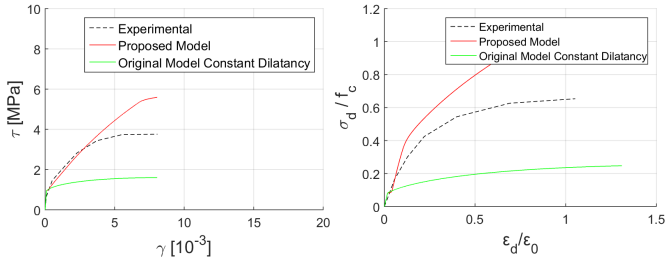

(a) Shear (b) Principal compression

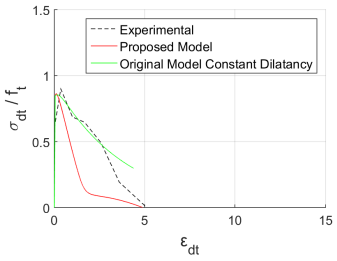

(c) Principal tension

Figure 3.16: Stress-strain plots of panel PV9. Experimental results by Vecchio, Collins (1982)

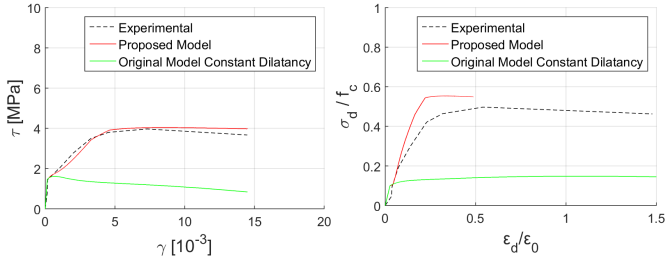

(a) Shear (b) Principal compression

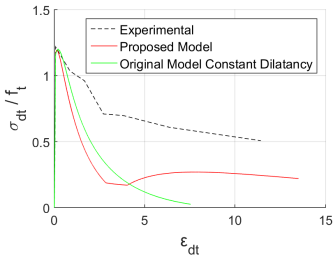

(c) Principal tension

Figure 3.17: Stress-strain plots of panel PV10. Experimental results by Vecchio, Collins (1982)

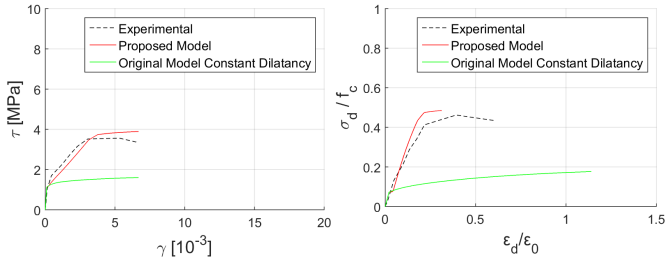

(a) Shear (b) Principal compression

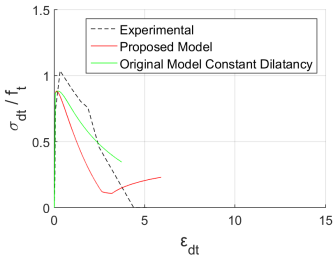

(c) Principal tension

Figure 3.18: Stress-strain plots of panel PV11. Experimental results by Vecchio, Collins (1982)

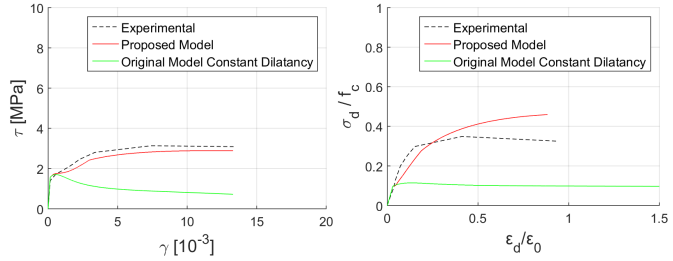

(a) Shear (b) Principal compression

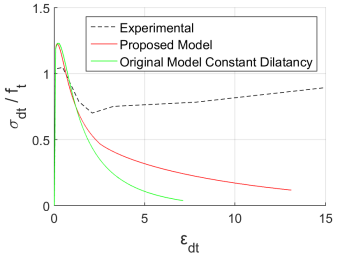

(c) Principal tension

Figure 3.19: Stress-strain plots of panel PV12. Experimental results by Vecchio, Collins (1982)

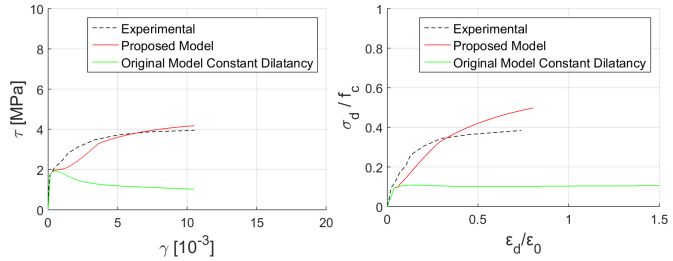

(a) Shear (b) Principal compression

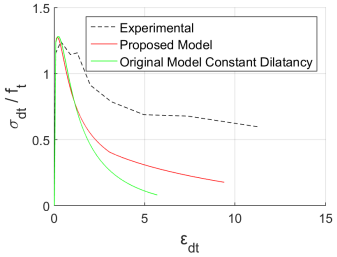

(c) Principal tension

Figure 3.20: Stress-strain plots of panel PV19. Experimental results by Vecchio, Collins (1982)

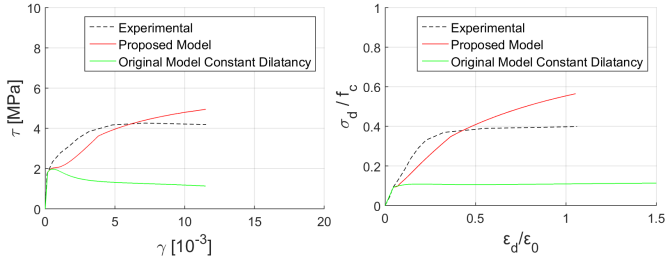

(a) Shear (b) Principal compression

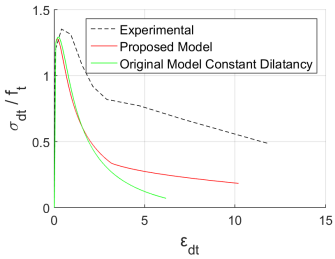

(c) Principal tension

Figure 3.21: Stress-strain plots of panel PV20. Experimental results by Vecchio, Collins (1982)

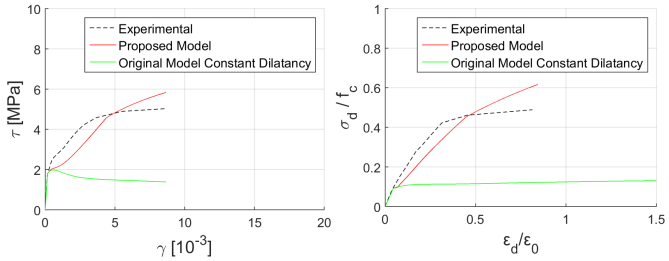

(a) Shear (b) Principal compression

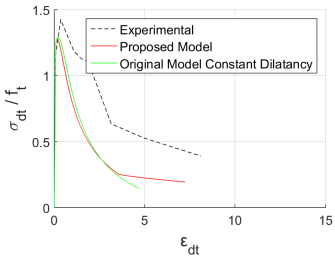

(c) Principal tension

Figure 3.22: Stress-strain plots of panel PV21. Experimental results by Vecchio, Collins (1982)

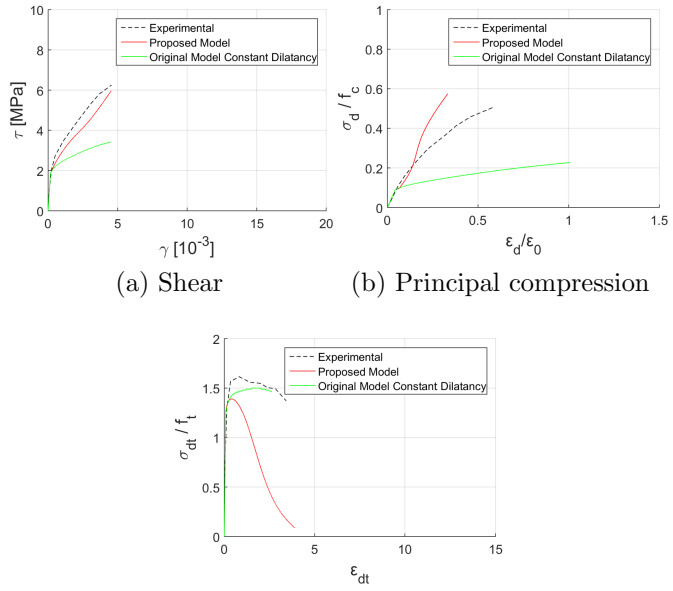

(a) Shear (b) Principal compression

(c) Principal tension

Figure 3.23: Stress-strain plots of panel PV27. Experimental results by Vecchio, Collins (1982)

As can be seen in Figs.(3.9-3.23), the shear response of the panels is well estimated by the present model. An improvement with regard to the constant dilatancy model is appreciated as the original constant dilatancy model tends to predict larger material softening and less shear capacity, in general.

The studied panels exhibit different failure modes; including specimens showing yielding of both longitudinal and transverse reinforcement, yielding of transverse reinforcement prior to concrete failure and concrete failure without yielding of the reinforcements. The model shows to be able to capture different modes of failure adequately without a recalibration of the dilatancy or the fracture energy parameters.

3.5 Sensitivity analysis

The evolution of the dilatancy parameter is controlled by means of two material properties as presented in Eq. (3.28). To study

the influence of these two parameters in the behavior of concrete, a sensitivity analysis is carried out in the following. Three numerical tests are performed with different values of both ψ^{max} and ϕ^{max}.

The first test is a uniaxial cyclic compressive test. Material properties remain the same for all specimens. Three different values (10°, 30°, 40°), of the maximum dilatancy angle are studied. Also three different values of the maximum internal friction angle are used (30°,50°, 70°). Combinations of these values give a total of eight tests, as the case where ϕ^{max} is smaller than ψ^{max} is discarded. In Figs.(3.24) to (3.26) stress and both axial and transverse strains curves are presented.

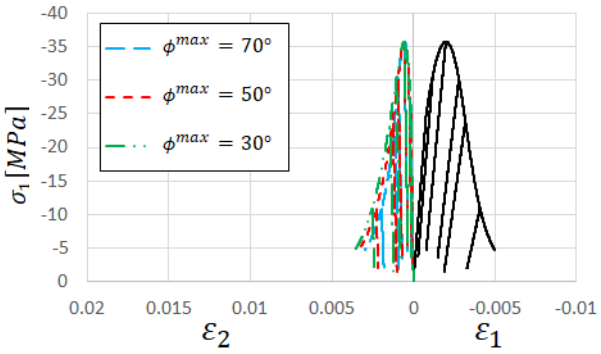

Figure 3.24: $\sigma_1 - \varepsilon_1$ and $\sigma_1 - \varepsilon_2$ for $\psi^{max} = 10°$

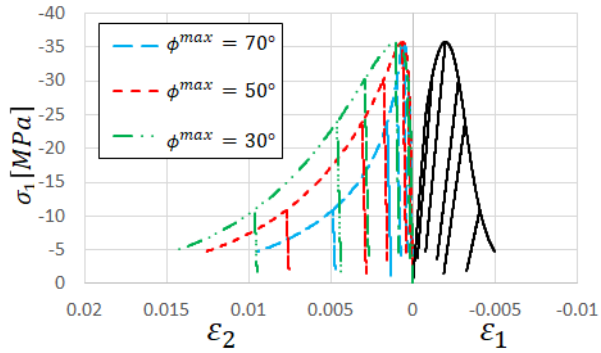

Figure 3.25: $\sigma_1 - \varepsilon_1$ and $\sigma_1 - \varepsilon_2$ for $\psi^{max} = 30°$

Results show that a greater dilatancy angle produces larger transverse strains. When it comes to the internal friction angle,

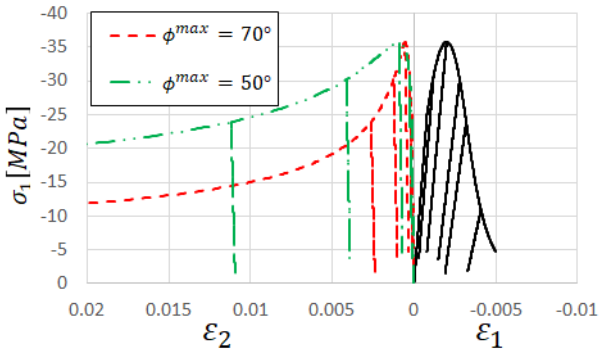

Figure 3.26: $\sigma_1 - \varepsilon_1$ and $\sigma_1 - \varepsilon_2$ for $\psi^{max} = 40°$

larger values of ϕ^{max} delays the onset of the dilatancy phenomenon producing smaller values of the transverse strain.

The second test involves the uniaxial compressive test of passively confined concrete. Steel is used as confinement material, with a transverse reinforcement ratio of 1% and a yield stress of $400MPa$, and the same combinations of ψ^{max} and ϕ^{max} are used.

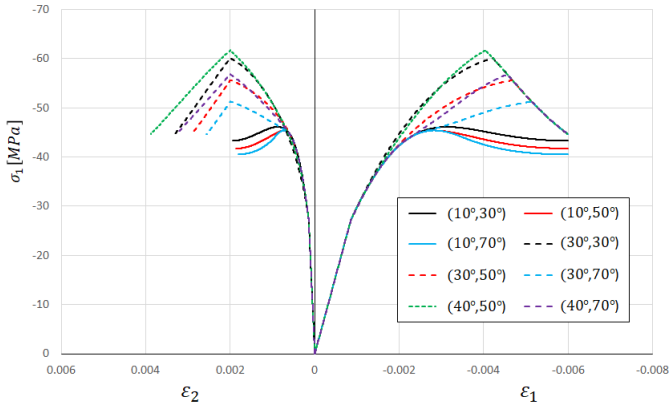

Figure 3.27: $\sigma_1 - \varepsilon_1$ and $\sigma_1 - \varepsilon_2$ curves for different values of (ψ^{max},ϕ^{max})

Figure (3.27) presents the results obtained with the present model. Consequently with the first test, a greater dilatancy angle produces an increase in the concrete strength. Also, as ϕ_{max} becomes greater, a slower increase in the concrete strength is obtained.

Finally, to study the influence of these two parameters in the concrete shear strength, a reinforced concrete panel is analyzed modifying ψ^{max} and ϕ^{max}. The shear stress-strain curve and the principal compressive stress versus the principal tensile strains curve are traced in Fig.(3.28).

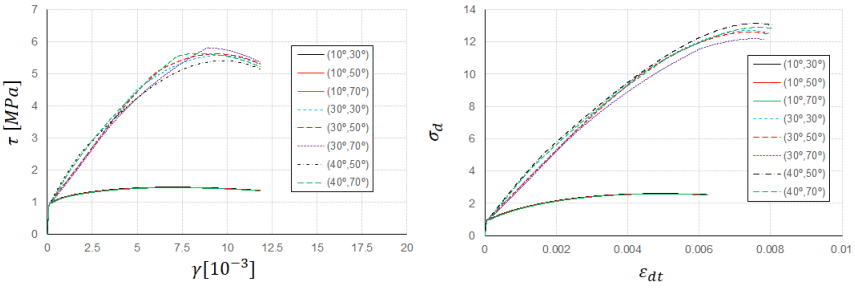

Figure 3.28: $\tau - \gamma$ and $\sigma_d - \varepsilon_{dt}$ curves for different values of (ψ^{max},ϕ^{max})

It can be seen that the lowest value of the dilatancy angle, $\psi^{max} = 10°$, predicts considerably lower values of the shear strength. However, small differences are observed for ψ_{max} between 30° and 40°. The influence of the maximum internal friction angle is rather small but it also demonstrates that the greater ϕ^{max} is taken the later the onset of dilatancy appears.

3.6 Closure

A constitutive plastic-damage model for concrete with evolutive dilatancy is proposed. The model is based on the original model of Lee, Fenves (1998, 2001) which in turns relies on the model of Lubliner et al. (1989). The original model has a constant dilatancy parameter. In this chapter, it is demonstrated that a constant value of the dilatancy parameter is not adequate to accurately predict the free expansion of concrete. Consequently, the original model has difficulties to trace the response under passive confinement or shear stresses.

A new constitutive plastic-damage model is here developed incorporating the variability of the dilatancy and friction angle pa-

rameters as explicit functions of the plastic-damage and stress states. This function produces the maximum dilatancy for uniaxial compression and pure shear states. The resulting dilatancy is automatically reduced when the confinement stresses increase.

The evolution of the dilatancy is controlled by two material properties, the maximum dilatancy and internal friction angles. These properties may be obtained through tests where different confinement stresses are considered. In this research, values of 32° for the maximum dilatancy angle and 65° for the maximum inner friction angle are proposed. These values are used in the validation of the proposed model obtaining good agreement with experimental results.

The validation of the proposed model is carried out by simulating several experimental campaigns producing different modes of failure and phenomenological responses of concrete. Ordinary to high strength concrete samples were considered along the validation tests, ranging from 11 to 80 MPa.

The model shows to be capable of accurately trace the volumetric expansion of concrete in uniaxial compressive tests including softening and confinement. It is also shown to be capable of capturing the enhancement in strength and ductility when passive confinement is applied by means of different confining materials. Good estimation of concrete shear strength and softening behavior is obtained. The model response is objective on different modes of failure with the same material parameters.

The adequate control of the dilatant behavior of concrete is shown to be of paramount importance as it controls the volumetric expansion and, consequently, affects the strength and ductility of confined concrete as well as the shear strength and softening.

The proposed dilatancy model contributes to extend the capabilities of the plastic-damage model in the simulation of reinforced concrete elements and structures in a consistent manner for different types of load and failure modes.

Chapter 4

B-spline sectional model for general 3D effects in reinforced concrete elements

In this chapter, an efficient sectional model for the nonlinear analysis of reinforced concrete elements sensible to 3D stress-components effects is presented. The classic plane-sections kinematic hypothesis is enhanced with a warping-distortion displacement field, which enables the model to reproduce the interaction between normal and tangential forces. The complementary field is obtained explicitly considering the inter-fiber equilibrium. This is solved using b-splines interpolation on the cross-section domain. The proposed method significantly reduces the number of unknowns compared with a finite element solution. The model is able to reproduce the interaction of longitudinal and transverse reinforcement with the concrete matrix. The validation shows that the presented model reproduces accurately complex failure modes as pure shear and coupling between bending and torsion. Further, as the transverse reinforcement is considered explicitly, confinement can be simulated in an objective manner. The presented model is an efficient tool for nonlinear analysis of reinforced concrete sections under general

loading.

4.1 Introduction

Structural elements where one dimension is much larger than the others can be assimilated as linear elements, this is the case of most slender beams and columns. The overall element behavior can be obtained by integration of the sectional response on each cross section along the elements axis Carol, Murcia (1989); Mari (1984); Spacone et al. (1996a). This type of elements allows a simple representation of complex structural systems and lead to efficient pre- and post-processing compared with the alternative solid three-dimensional models. Further, 1D elements are closer to the engineering practice, as most codes and provisions EN CEN (2005); CEB-FIB (2010); ACI Committee 318 (2014) are orientated to the design or assessment of one dimensional elements as beams or columns, and its cross section domain. Guidelines on the design of structural elements under 3D states are scant.

The accuracy of 1D elements depends on the proper representation of the behaviour of each cross section. Traditionally, the plane-section kinematic hypothesis of Navier-Bernoulli is made in conjunction with uniaxial fiber discretization of the cross-section Taucer et al. (1991); Spacone et al. (1996a,b). This enables the model to efficiently reproduce the interaction between bending moments and the axial load. Robust beam models were developed following this approach Kang, Scordelis (1980); Mari (1984); Taucer et al. (1991); Spacone et al. (1996a,b), and were applied to the analysis of reinforced concrete structures where the failure was principally due to axial loads or bending moments.

The main shortcoming of this type of models is that the interaction between normal (axial load and bending moments) and tangential (shear loads and torsion) forces is neglected Ranzo, Petrangeli (1998); Ceresa et al. (2007); Bairán, Marí (2007b). This causes a loss of accuracy in elements with high shear forces or torsional moment, especially if anisotropic materials are involved. It

has also been shown in Balduzzi et al. (2019); Karttunen, Hertzen von (2016) that anisotropy leads to an explicit dependency of axial stresses on the shear force. In particular, in this chapter the applications are focused on the problem of cracked-induced anisotropy of concrete, which controls the interaction between normal and shear stresses, as described in Onsongo (1978); Hsu (1984); Park, Paulay (1975); Bairán, Marí (2007b).

Moreover, classic fiber-beam models only consider longitudinal fibers. In typical reinforced concrete sections they represent the concrete mass and longitudinal reinforcements, and do not consider transverse elements, as stirrups or jackets. These transverse elements provide different shear strength mechanisms. Further, they constrain the concrete transverse expansion in compressive cases, providing a confining pressure, which increases both the strength and ductility of concrete. In classic-fiber-beam models Taucer et al. (1991); Spacone et al. (1996a,b), the transverse reinforcements is accounted for at the material level by means of reinforcement ratios in empirically based 1D constitutive laws.

The need of reproducing different failure modes, as shear or torsional failures, as well as capturing the role of transverse reinforcements, became of special interest the last years with the assessment and reinforcement of existing structures and with the increasing demand of nonlinear analysis by the new codes and provisions Ceresa et al. (2007). This motivated several researchers to study the coupling between normal and tangential forces and to develop models that take into account different degrees of interaction, Ceresa et al. (2007); Vecchio, Collins (1988); Bentz (2000); Bairán, Marí (2006a,b, 2007a); Mohr et al. (2010); Le Corvec (2012); Di Re (2017); Kagermanov, Ceresa (2018).

In this chapter, the sectional model proposed by Bairán, Marí (2006a,b, 2007a) is modified using a novel numerical technique, which substantially improves the computational performance and requires less number of internal degrees of freedom for a similar accuracy. Here, a complementary displacement field which enables the model to reproduce the total interaction, is obtained as

a weighted sum of b-splines functions defined in the cross-section domain. In this way, the number of degrees of freedom involved is significantly reduced in comparison with a finite element (FE) solution. The presented model is then validated through a series of tests cases where the capabilities to reproduce tangential forces are shown. Further, the model is applied to study confinement in reinforced concrete sections where the interaction between concrete and transverse reinforcements is essential. Finally, main conclusions are drawn.

4.2 Multiaxial interaction in frame elements

The robustness of fiber-beam elements, and the increasing need of reproducing complex failure modes that involve the coupling between normal and tangential internal forces, have motivated researchers to extend the classical fiber-beam models to include different degrees of interaction between internal forces. Extended state of the art reviews can be found in Ceresa et al. (2007) and Bairán, Marí (2007b). Here, only models based on inter-fiber equilibrium are briefly reviewed as they showed to be able to accurately reproduce different failure modes.

Vecchio, Collins (1988) developed a *dual-section analysis* for the case of 2D frame elements. The coupling between longitudinal and transverse stresses is obtained by explicitly considering the equilibrium between fibers, which involves the analysis of two adjacent cross-sections to approximate the longitudinal stress gradient. The dual-section model is a non local model, as it needs information from adjacent points, so an ad-hoc element formulation is needed. To overcome this problem, Bentz (2000) introduced the *Longitudinal Stiffness Method*, where the longitudinal stress gradient was calculated locally considering equilibrium equations at the beam level. This method is a local sectional model, but only for 2D elements.

Later, Bairán, Marí (2006a,b, 2007a) presented a sectional model called TINSA (*Total Interaction Nonlinear Sectional Analysis*). It is based on the enhancement of the kinematic field of the Navier-Bernoulli theory by means of a *warping-distortion* displacement field which is obtained by solving the inter-fiber equilibrium in the section domain with a 2D FE model. The warping-distortion field considered is independent of the x-coordinate neglecting its variation along the beam length, this leads to a sectional model that is completely independent of the frame formulation, thus there is no need for additional degrees of freedom at the beam level. A consequence of this assumption is that the effect of non-uniform warping and shear lag effects are neglected, but this is relevant in thin-walled sections rather than in compact cross sections as is the case of most reinforced concrete beams and columns. This formulation proved to capture the interaction between the six possible internal forces in sections of any shape and takes into account both longitudinal and transverse reinforcements explicitly. Its main drawback is the higher computational demand compared with traditional beam models.

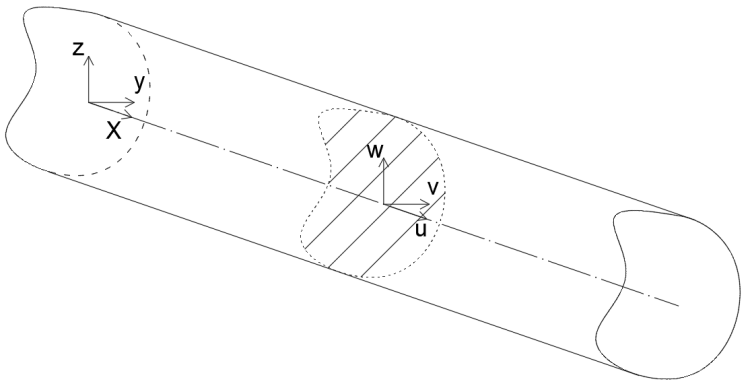

Figure 4.1: Coordinate system

Mohr et al. (2010), presented a modification of the TINSA model for the case of 2D frames. The complementary displacement field is calculated as a weighted sum of Taylor's polynomials defined in the section height. This method avoids the FE solution,

reducing the computational cost of the original model. The sectional model was implemented on a flexibility-based frame element and tested in beams with bending moment and shear. As it was developed for 2D frames, no torsion or bidirectional shear flows can be analysed with this model.

Le Corvec (2012) and Di Re (2017) presented 3D frame elements based also on the displacement decomposition. As an additional hypothesis to the original formulation, they presented a complementary displacement field, which only produces warping neglecting the distortion of the cross-section. The out of plane displacement is obtained by interpolation over the section domain but also on the beam length, this allows the model to capture non uniform warping and shear lag effects. As interpolation function over the cross section domain, Le Corvec (2012) used Lagrange's polynomials, while Di Re (2017) included Hermite's polynomials. Both models were implemented in 3D force-based elements based on the Hu-Washizu variational principle. These models can capture the interaction of the internal forces in a tri-dimensional element, but the hypothesis of considering a complementary field with only warping has the drawback that distortion of the section is not captured, so transverse reinforcement is not considered explicitly. Besides, as the complementary field is interpolated on the beam length, a special frame formulation is developed with more degrees of freedom at the beam level that have to be considered or properly condensed.

Kagermanov, Ceresa (2018), presented a 3D frame element based on the Timoshenko beam theory that accounts for warping effects with the Saint-Venant theory of torsion. There, the warping sectional function was obtained by means of solving the boundary value problem with a FE sectional model. The model is able to capture interaction between the internal forces, but it relies on a fixed strain pattern so it neglects inter-fiber equilibrium.

Based on the previous analysis, the following aspects on the enhanced 1D elements for non-linear concrete analysis are still open; their robustness and computational demand, their ability to trace different failure modes, such as shear and confinement failures, in

an objective manner for different geometries and reinforcement arrangements. This motivates the development of a new sectional model.

4.3 Proposed model formulation

4.3.1 Basic features

In the following, the sectional model proposed by Bairán, Marí (2006a,b, 2007a) is modified by the introduction of a novel numerical technique in order to reduce its computational demand. The problem is focused on a frame element where the x coordinate coincides with the frame axis and the cross-section is defined on the y-z plane. The proposed model neglects the boundary effects, so the hypothesis that the domain is far enough of the discontinuity regions is made. The main hypothesis is the decomposition of the displacement field into two parts: a displacement field that follows the plane-sections kinematic hypothesis of the Navier-Bernoulli theory ($\boldsymbol{u}_{ps}$), and a complementary field that captures the sections distortion and warping ($\boldsymbol{u}_{w}$). Thus, the total displacement field is obtained as follows:

$$\boldsymbol{u} = \boldsymbol{u}_{ps} + \boldsymbol{u}_{w} = \left\{ \begin{array}{c} u_{ps} \\ v_{ps} \\ w_{ps} \end{array} \right\} + \left\{ \begin{array}{c} u_{w} \\ v_{w} \\ w_{w} \end{array} \right\} \tag{4.1}$$

This decomposition can be done straightforwardly in strains, as small strains are assumed, see Eq.(4.2). Regarding stresses, in the case of nonlinear materials, the same decomposition is valid in an incremental format, and after the integration along the load steps the decomposition can be done without losing generality as in Eq.(4.3).

$$\boldsymbol{\varepsilon} = \boldsymbol{\varepsilon}_{ps} + \boldsymbol{\varepsilon}_{w} \tag{4.2}$$

$$\boldsymbol{\sigma} = \boldsymbol{\sigma}_{ps} + \boldsymbol{\sigma}_{w} \tag{4.3}$$

As it was previously stated, to obtain the complementary field, the inter-fiber equilibrium is considered explicitly. To do so, first the 3D equilibrium equation of a beam is posed in its weak form, as in Eq.(4.4). Then, the equilibrium residual of a differential element $R(x)$ can be identified, see Eq.(4.5)

$$\iiint_{\Omega} div\,(\boldsymbol{\sigma})\ \ \delta\boldsymbol{u}\ d\Omega = 0 \tag{4.4}$$

intended

$$\int_0^L \left(\iint_A div\,(\boldsymbol{\sigma})\ \ \delta\boldsymbol{u}\ dA \right) dx = \int_0^L R\,(x)\,dx = 0 \tag{4.5}$$

The projection of the residual into both displacements fields allows the identification of two equilibrium levels: the beam level represented by the projection of the residual in the plane-section displacement field R_{ps}, and the sectional level which implies the projection of the residual in the complementary field R_w.

$$R_{ps}\,(x) = \iint_A div\,(\boldsymbol{\sigma})\ \ \delta\boldsymbol{u}_{ps}\ dA = 0 \tag{4.6}$$

$$R_{w}\,(x) = \iint_A div\,(\boldsymbol{\sigma})\ \ \delta\boldsymbol{u}_{w}\ dA = 0 \tag{4.7}$$

In order to solve the system in Eqs.(4.6) and (4.7), first $R_w = 0$ is posed at each cross-section of the beam, and then the beam equilibrium $R_{ps} = 0$ is solved. Solving the equilibrium in this way, leads to the full 3D stress tensor, taking into account explicitly the inter-fiber equilibrium.

The main unknown of the sectional model is the warping-distortion displacement field ($\boldsymbol{u}_w$). To assure the uniqueness of the solution, it is established that the two types of displacement fields should be orthogonal to each other Bairán, Marí (2006a). In order to approximate the complementary field, an additional hypothesis is made; namely, the warping-distortion field is independent of the x-coordinate neglecting its variation along the beam length, see Eq.(4.8).

$$\boldsymbol{u}_w = \boldsymbol{u}_w\left(y,z\right) = \left\{ \begin{array}{c} u_w(y,z) \\ v_w(y,z) \\ w_w(y,z) \end{array} \right\} \tag{4.8}$$

This enables the definition of a cross-sectional model that can be used as a response model of any standard 1D frame formulation. The model solves the sectional equilibrium, Eq.(4.7), and relates the generalized beam strains with the internal forces, or generalized stresses, see Eq.(4.9).

$$\boldsymbol{\epsilon}_s = \left\{ \begin{array}{c} \varepsilon_0 \\ \gamma_y \\ \gamma_z \\ \phi_x \\ \phi_y \\ \phi_z \end{array} \right\} \Leftrightarrow \boldsymbol{s}_s = \left\{ \begin{array}{c} N \\ V_y \\ V_z \\ T_x \\ M_y \\ M_z \end{array} \right\} \tag{4.9}$$

Once the sectional equilibrium is achieved, the full stress tensor is obtained on each material point of the cross-section. To obtain the internal forces $\boldsymbol{s}_s$, the integration of stresses on the section domain is made considering the virtual work principle. This definition assures that the obtained generalized stresses are energetically conjugated to the generalized strains, see Eq.(4.10).

$$\boldsymbol{s}_s = \iint_A \boldsymbol{B}_{ps}^T \boldsymbol{\sigma} dA + \boldsymbol{\Omega}^T \boldsymbol{\Xi}^T \boldsymbol{A}^{*T} \iint_A \boldsymbol{B}_w^T \boldsymbol{\sigma} dA \tag{4.10}$$

Where $\boldsymbol{B}_{ps}$ and $\boldsymbol{B}_w$ are strain interpolation matrix that relate the generalized beam strains with the strains on each material point of the section, see Eq.(4.11). $\boldsymbol{A}^*$, $\boldsymbol{\Xi}$ and $\boldsymbol{\Omega}$ are transformation matrices that stands for internal equilibrium conditions, condensation of redundant degrees of freedom and definition of generalized shear strains, respectively. A detailed derivation of the matrices for the general case of non-isotropic materials can be found in Bairán, Marí (2006a, 2007a).

$$\begin{aligned} \boldsymbol{\varepsilon}_{ps} &= \boldsymbol{B}_{ps}\boldsymbol{\epsilon}_s \\ \boldsymbol{\varepsilon}_{w} &= \boldsymbol{B}_{w}\boldsymbol{\epsilon}_s \end{aligned} \tag{4.11}$$

The use of the sectional model as a response model on any point of a beam needs the definition of a sectional stiffness matrix $\boldsymbol{K}_s$, which is computed as in Eq.(4.12). Where $\boldsymbol{D}$ is a general material constitutive matrix.

$$\begin{aligned} \boldsymbol{K}_s = &\iint_A \boldsymbol{B}_{ps}^T \boldsymbol{D} \boldsymbol{B}_{ps} dA + \left(\iint_A \boldsymbol{B}_{ps}^T \boldsymbol{D} \boldsymbol{B}_{w} dA \right) \boldsymbol{A}\boldsymbol{\Xi}\boldsymbol{\Omega} \\ &+ \boldsymbol{\Omega}^T \boldsymbol{\Xi}^T \boldsymbol{A}^{*T} \left(\iint_A \boldsymbol{B}_{w}^T \boldsymbol{D} \boldsymbol{B}_{ps} dA \right) \\ &+ \boldsymbol{\Omega}^T \boldsymbol{\Xi}^T \boldsymbol{A}^{*T} \left(\iint_A \boldsymbol{B}_{w}^T \boldsymbol{D} \boldsymbol{B}_{w} dA \right) \boldsymbol{A}\boldsymbol{\Xi}\boldsymbol{\Omega} \end{aligned} \tag{4.12}$$

4.3.2 Numerical solution

Solving the sectional problem needs a proper space discretization. The original model proposed by Bairán, Marí (2006a), solved the problem using a standard 2D FE model, where bidimensional elements represented the solid matrix, linear elements represented transverse reinforcements and point element represented longitudinal reinforcements. The FE solution involves a high number of degrees of freedom (DOF) to solve the sectional problem in most applications, increasing the computational demand. A different approach is proposed here to reduce the DOF involved in the solution.

The warping-distortion complementary field in Eq.(4.8) is approximated by a weighted sum of predefined functions, see Eq.(4.13). This reduces significantly the number of degrees of freedom involved to solve the sectional problem compared with the FE solution.

$$\boldsymbol{u}_w = \left\{ \begin{array}{c} u_w \\ v_w \\ w_w \end{array} \right\} = \left\{ \begin{array}{c} \sum a_i F_i(y,z) \\ \sum b_i F_i(y,z) \\ \sum c_i F_i(y,z) \end{array} \right\} \tag{4.13}$$

The weight factors (a_i,b_i,c_i) represent the unknowns of the prob-

lem. The most classical interpolation functions relies on Lagrange's functions. For a given interpolation grid, the interpolation is performed first independently on each geometric coordinate, then the surface in the section domain is obtained by the tensor product. This method produces one function for each point of the interpolation grid. However, when the number of points of the interpolation grid increases, the order of the Lagrange polynomial increases as well. This may lead to high order polynomials in practical cases, introducing undesired oscillations augmenting the interpolation error locally.

In order to overcome this issue, piecewise polynomials are used which allows controlling the order of the polynomial in spite the number of grid points. A family of these polynomials are known as splines, they account for continuity conditions in the boundary of the intervals defined by the interpolation grid, and has proven to be efficient and robust Farin (1999). Thanks to that, their use in FE element frameworks has increased in the last years Wei et al. (2017); Hughes et al. (2014); Höllig, Hörner (2015).

B-splines (basis splines) are constructed from a knot vector which contains their coordinates in increasing order, $\boldsymbol{Z} = \{\zeta_1, \zeta_2, \ldots, \zeta_{n+p+1}\}$, where p is the polynomial order and $n+1$ is the number of basis functions. In Eq.(4.14) the recursive form proposed by De Boor (2001) is formulated for the i-th basis function.

$$
\begin{aligned}
N_{i,p}(\zeta) &= \frac{\zeta - \zeta_i}{\zeta_{i+p} - \zeta_i} N_{i,p-1}(\zeta) + \frac{\zeta_{i+p+1} - \zeta}{\zeta_{i+p+1} - \zeta_{i+1}} N_{i+1,p-1}(\zeta) \\
N_{i,0} &= \begin{cases} 1 \; if \; \zeta_i \leq \zeta < \zeta_{i+1} \\ 0 \; otherwise \end{cases}
\end{aligned}
\tag{4.14}
$$

If the value of a function in the boundaries of the knot vector is to be interpolated, an open knot vector with multiplicity of the first and last value is needed. In this work, cubic polynomials are used. Then, for an interpolation grid of n non-repeated elements $n+2$ basis functions can be constructed on each coordinate. Further, the interpolation surface is obtained by the tensor product, see

Eq.(4.15).

$$F_{ij,pq}(y,z) = \boldsymbol{P}_{ij} N_{i,p}(y) M_{j,q}(z) \tag{4.15}$$

For a given cross-section geometry, a number of points has to be selected in order to build the interpolation grid. The b-spline functions are constructed using Eq.(4.14). The set of b-spline functions constitutes the shape functions defined over the cross section. Fig.(4.2) shows the grid point selected for a square section and one of the basis functions used in the interpolation. This process is done for each component of the complementary displacement field.

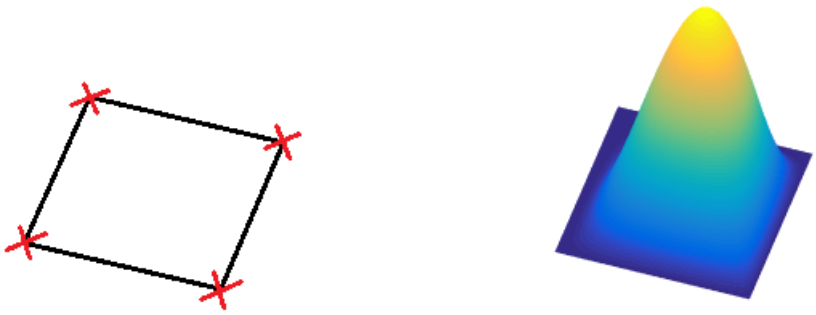

(a) (b)

Figure 4.2: Bspline Interpolation a) Interpolation grid, b) Basis function

The midpoint integration rule is used to solve the sectional problem as in classical fiber-beam models. Each integration point represents a material point or a fiber. The solid part of the cross section is represented by fibers with 3D constitutive laws and are defined by their geometrical coordinates (y, z) and their projected area on the section. The transverse and longitudinal reinforcements are represented by fibers with uniaxial constitutive laws. Furthermore, fibers are defined by their position, their projected area in the cross-section plane, and by their inclination with respect to the beam axis. This allows the model to include inclined transverse or longitudinal bars indistinctly.

4.3.3 Sectional Algorithm

The structure of the algorithm that computes the sectional state is shown in Fig.(4.3). The value of the force tolerance used in all numerical cases is equal (in Newtons) to $tol = 0.001A_c$, where A_c is the area of the cross-section.

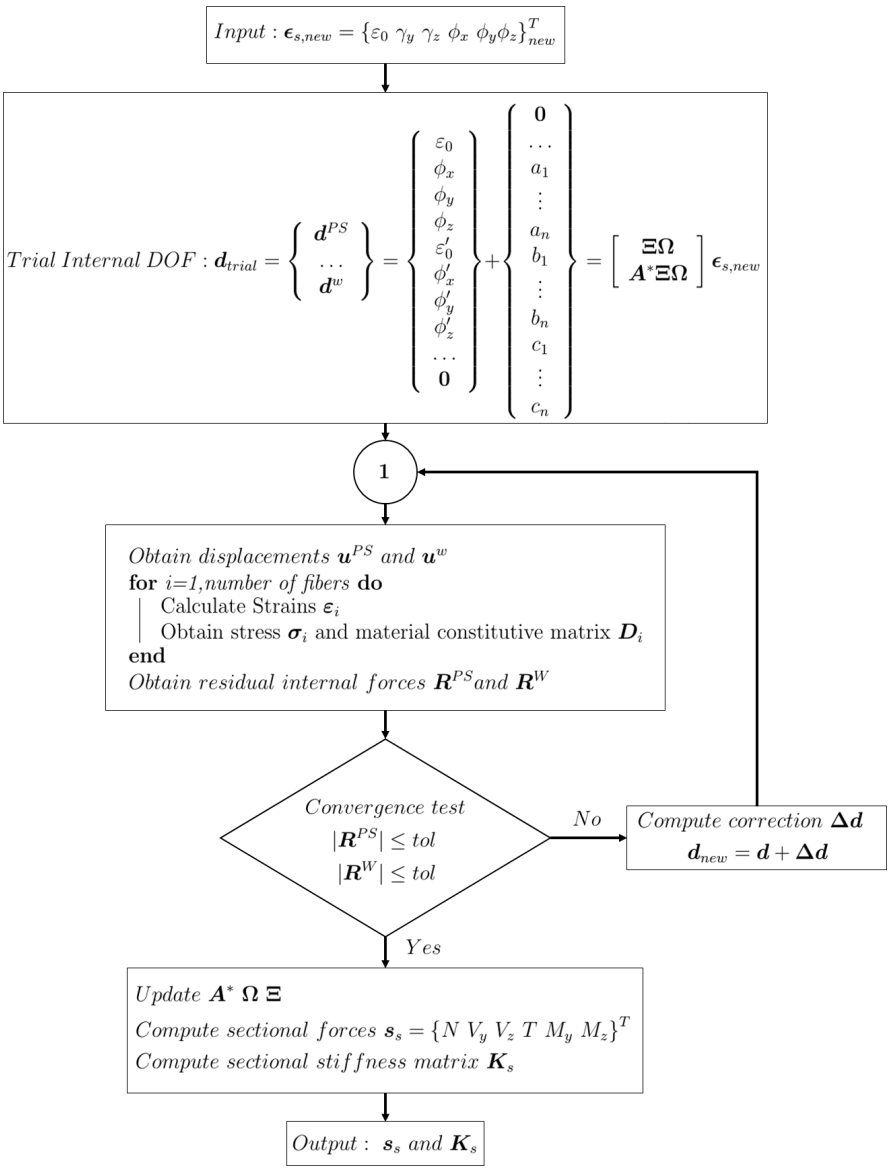

Figure 4.3: Sectional model flow chart

4.4 Validation

In order to verify the accuracy and test the capabilities of the proposed model, two validation sets are presented in the following. The first validation set involves three sections under tangential forces, namely: a triangular elastic section in pure torsion, a reinforced concrete section tested in pure shear and a reinforced concrete box section under combined bending and torsion moments. These three cases are numerically simulated with the proposed model. The FE solution with the TINSA model Bairán, Marí (2006a) is also presented. In the case of the elastic triangle in torsion, the obtained response is compared against a theoretical result. In both reinforced concrete sections, experimental results available in literature are contrasted with the numerical simulations.

The second set of validation comprises four sections under axial loading with different confining materials and transverse reinforcement arrangements. First, a reinforced concrete circular section winch is transversally reinforced by a steel spiral is tested. Then, a rectangular section reinforced by transverse stirrups is simulated. Further, a circular section wrapped with a CFRP jacket is simulated. Finally, a rectangular concrete filled tube is analyzed. The results obtained with the proposed model are compared against experimental data available in literature.

In the six cases concerning reinforced concrete sections, perfect bond is assumed. The constitutive law for the steel fibers is a 1D elastic-plastic model with kinematic hardening. Concerning the constitutive modelling of concrete, it is worth mentioning that the presented sectional model can be used with any tri-dimensional constitutive law. If different failures modes are to be reproduced, the constitutive model has to be able to trace a wide range of loading conditions namely shear stresses and high confinement. To this end, the plastic-damage model with evolutive dilatancy introduced in the previous chapter is used. The evolutive dilatancy parameter presented there, proved to be able to reproduce shear softening and passive confinement with different confining materials in an

accurate manner without recalibration of dilatancy parameters.

The material properties are obtained from the experimental reported data on each case. The concrete material parameters are estimated by means of Eqs.(3.30) to (3.32).

4.4.1 Sections under shear or torsion

Elastic triangle under pure torsion

An equilateral triangular elastic section is tested under pure torsion, whose closed-form analytical solution was obtained in Timoshenko, Goodier (1972). The section height is 200 mm, four points are selected as interpolation grid to construct the b-splines leading to 83 degrees of freedom, and 219 isotropic elastic fibers with the material properties described in Table 4.1 are used. See Fig.(4.4).

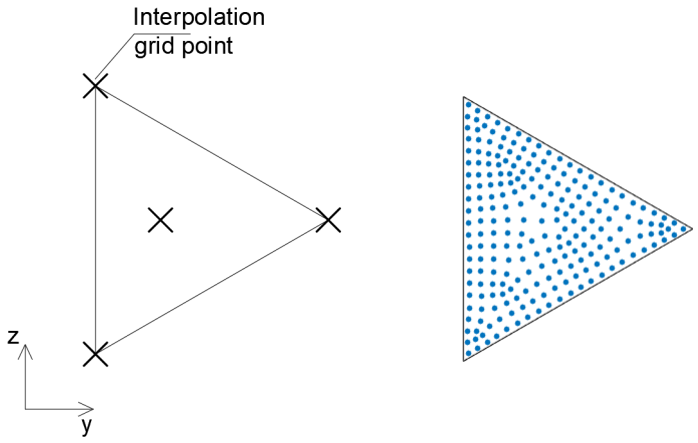

(a) (b)

Figure 4.4: Triangular section: a) Interpolation grid, b) Fiber distribution.

Table 4.1: Material properties validation case 4.4.1

E [MPa]	G [MPa]	ν
30000	12500	0.2

A torsional curvature of $\phi_x = 1e^{-6}\ rad/mm$ is applied on the centroid of the section. It can be seen, in Fig.(4.5), that by means

of the warping-distortion displacement field, the tangential stresses and the bi-dimensional shear stress flow are obtained and agree with the theoretical stress pattern.

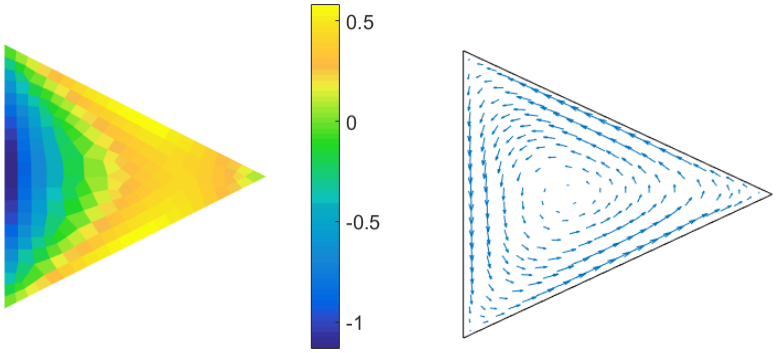

(a) (b)

Figure 4.5: Triangle under pure torsion: a) τ_{xz} stresses [MPA], b) Shear stress flow.

The maximum tangential stresses as well as the torsional moment are obtained with the presented model and with the model FE TINSA Bairán, Marí (2006b). Besides, four additional b-spline models are analyzed varying first the number of fibers and then the number of degrees of freedom involved in the solution. Table 4.2 presents numerical results compared against the theoretical solution obtained by Timoshenko, Goodier (1972). The computational time of each numerical model is addressed as well.

A good agreement with the theoretical solution is obtained regarding the predicted torsional moment. Concerning the maximum stress value all the numerical solutions predict a smaller value than the closed-form solution. This difference can be explained as the maximum value on the theoretical solution is obtained exactly on the edge of the section, while the numerical solutions calculate stresses on discrete locations which are inside the cross-section. The stress field presented by Timoshenko, Goodier (1972) varies quadratically with the y coordinate, which explains that small distances from the edge produce significant variations on the stresses. In Table 4.2, the error calculated against the theoretical stress value

Table 4.2: Triangular Section in Torsion

	Analytical[a]	FE TINSA	B-Splines	B-Splines	B-Splines	B-Splines	B-Splines
DOF		767	83	83	83	56	134
Fibers		219	219	1007	91	219	219
T_x [KNm]	0.770	0.764	0.759	0.767	0.731	0.758	0.764
Error [%]		0.78	1.43	0.39	5.06	1.56	0.78
τ_{xz}^{max} [MPa]	1.250	1.128	1.129	1.192	1.044	1.131	1.153
Error [b] [%]		9.76	9.68	4.64	16.5	9.52	7.76
Error [c] [%]		0.18	0.27	0.04	0.32	0.05	0.49
Time [sec]		10.7	0.37	1.54	0.17	0.31	1.02

[a] Theoretical solution by Timoshenko, Goodier (1972)
[b] Error with respect to the maximum theoretical stress value.
[c] Error with respect to the theoretical stress value on the same location of the fiber.

on the exact same location of the fiber shows that the proposed model captures the stress field in a good manner.

In this case, it can be seen that the most effective way to improve the numerical solution is increasing the number of fibers. This is due to the fact that the displacement field on the theoretical solution Timoshenko, Goodier (1972) has a cubic shape, which can be represented with a reduced number of b-spline functions.

A significant reduction in the number of internal degrees of freedom used can be seen in comparison with the FE solution using the TINSA model. However, results remain on the same level of accuracy. The reduction is translated to the computational time, the b-splines model is faster than the FE model in identical computational conditions.

Reinforced concrete section in pure shear

In the following, the response of a reinforced concrete section tested by Kani (1977) under pure shear loading, is simulated with the proposed model. The analyzed cross-section is situated on the inflection point of a beam in order to reproduce the pure shear load. The geometry and reinforcement arrangement can be seen in Fig.(4.6a). In addition, the reported values of the material properties are indicated in Table (4.3).

Table 4.3: Material properties validation case 4.4.1

Concrete	f_c	28.2 MPa
	f_t	1.75 MPa
	E_c	25600 MPa
	ν	0.2
Longitudinal Steel	f_y	442 MPa
	E_s	200000 MPa
Transverse Steel	f_y	400 MPa
	E_s	200000 MPa

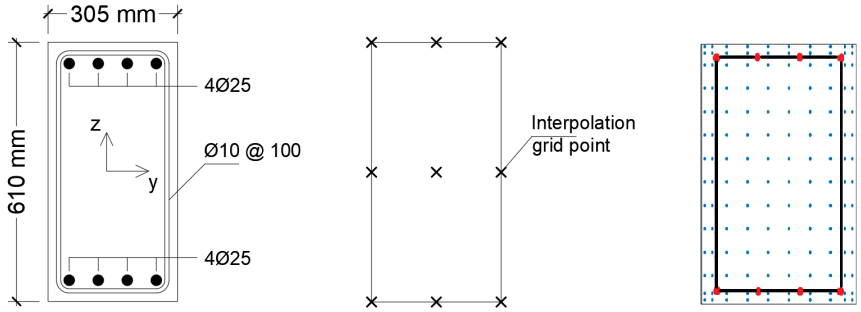

Figure 4.6: Specimen: a) Cross-section, b) Interpolation grid, c) Fiber distribution.

The interpolation grid consist on 9 points, 180 material points were used consisting on 140 concrete fibers, 32 fibers for the stirrups and 8 for the longitudinal reinforcement, see Fig.(4.6b) and (4.6c). The simulation is performed applying shear strains to the section instead of shear loads in order to capture eventual softening. A total of 70 steps are used to apply the shear strains.

The numerical shear force-strain curve obtained with the presented model is compared against the experimental response in Fig.(4.7). Further, the numerical response obtained with the model FE TINSA Bairán, Marí (2006a) is plotted. Good prediction of the ultimate load was obtained with the presented model. Small differences between both numerical responses exists even though the number of degrees of freedom is appreciably less in the proposed model (83 DOF) than in the FE TINSA model with the same num-

ber of fibers (503 DOF). The computational time is reduced nearly 3 times using the B-spline model compared to the FE solution in similar computational conditions. It is worth to mention that the computational time depends not only on the number of DOF but also on the number of material points or fibers.

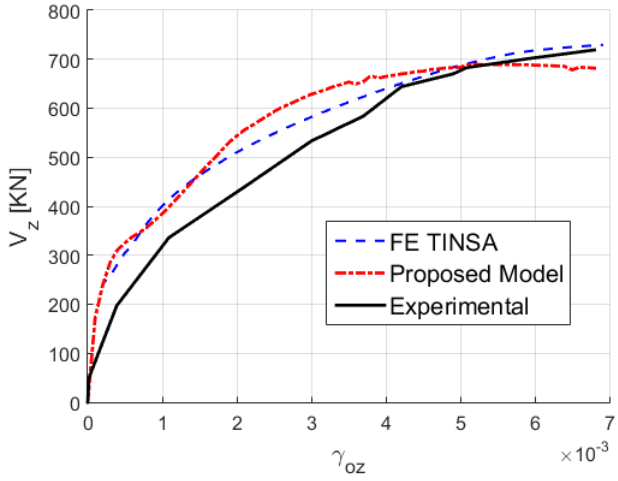

Figure 4.7: Shear force-strain curve. Experimental results by Kani (1977)

Fig.(4.8) shows part of the information obtained with the presented model. In particular, Fig.(4.8a) presents the stress distribution on the stirrups at a load level where the vertical branches of the stirrups begin to yield. On Fig.(4.8b) the tangential stress τ_{xz} pattern is shown. It can be seen that it varies along the vertical axis and on the horizontal one, stresses concentrate where the theoretical compressive strut intersects the section.

Reinforced concrete section under combined torsion and bending moments

The response of a reinforced concrete section under the combined action of torsion and bending moments tested by Onsongo (1978) is simulated using the proposed approach. The selected specimen, named TBU2, was part of a larger experimental campaign where different bending to torsion ratios were studied. The main features

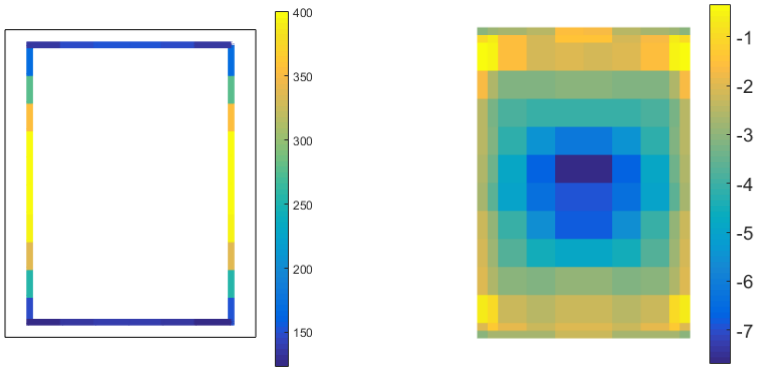

(a) σ_{st} [MPa] (b) τ_{xz} [MPa]

Figure 4.8: a) Stirrups stresses, b) Concrete tangential stresses

of the studied cross-section can be seen in Fig.(4.9a), the material properties are summarized in Table(4.4).

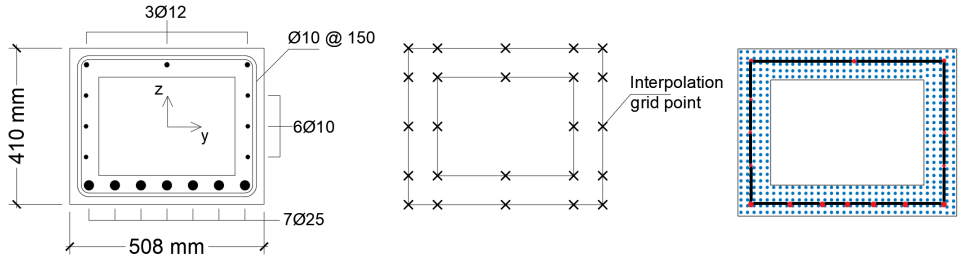

(a) (b) (c)

Figure 4.9: Specimen: a) Cross-section, b) Interpolation grid, c) Fiber distribution.

The interpolation grid can be seen in Fig.(4.9b). The fibers distribution is shown in Fig.(4.9c); it consists of 500 concrete fibers, 104 stirrup fibers and 16 fibers representing the longitudinal reinforcement.

The analysis of the section is performed controlling the torsional curvature and constraining the internal force vector to represent the bending to torsion ratio of the selected specimen which was $R = T/M = 0.261$. A total of 220 increments are applied to the section before it reaches the ultimate curvature.

Fig.(4.10) shows the response curves obtained with the proposed

Table 4.4: Material properties validation case 4.4.1

Concrete	f_c	34.8 MPa
Longitudinal Steel	$\varnothing 25$ f_y	436 MPa
	$\varnothing 12$ f_y	393 MPa
	$\varnothing 10$ f_y	552 MPa
	E_s	200000 MPa
Transverse Steel	$\varnothing 10 f_y$	379 MPa
	E_s	200000 MPa

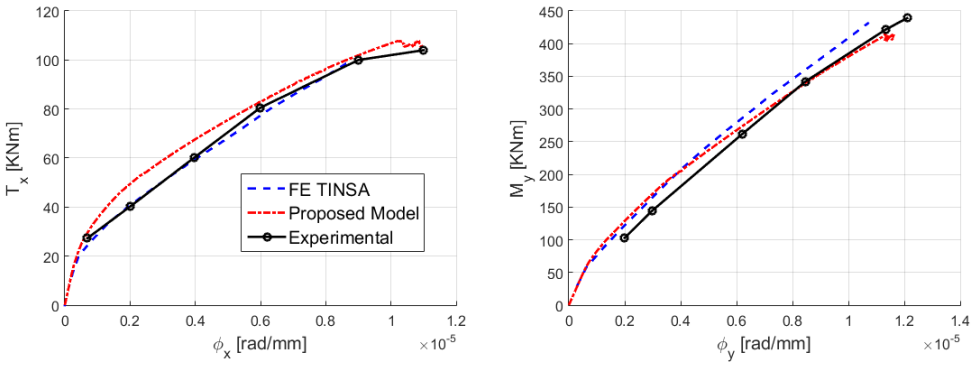

(a) (b)

Figure 4.10: a)Torsion-curvature and b) Moment-curvature curves. Experimental results by Onsongo (1978)

model, the experimental curves and the obtained with the TINSA model by Bairán, Marí (2007a) are traced as well, with good agreement with the experimental results. Good predictions of both the ultimate load and curvature are obtained. The response predicted by the proposed model shows numerical oscillations near the ultimate load. These are due to the failure of some material points. On the contrary, the TINSA model fails to converge once the ultimate load is reached. The convergence test in the TINSA model is performed evaluating the unbalanced nodal forces of the finite element mesh. The proposed model performs the convergence test using energetically conjugated forces to the weight factors of the b-splines in Eq.(4.13), which are obtained integrating over the whole cross-section. This makes the proposed model less sensitive to the

failure of a single material point than the TINSA model.

As in the previous cases, a significant decrease of the degrees of freedom used by the proposed model (243 DOF) with respect to the FE model of TINSA Bairán, Marí (2007a) with the same number of fibers (1808 DOF) is made. A speedup of around 5 is obtained with the proposed model in comparison with the FE model in similar computational conditions.

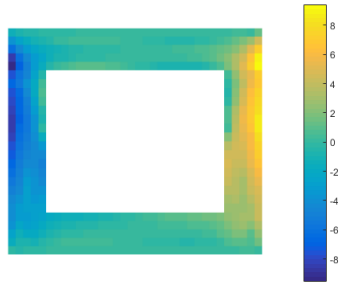

(a) τ_{xz} [MPa]

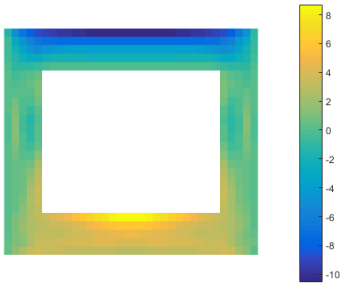

(b) τ_{xy} [MPa]

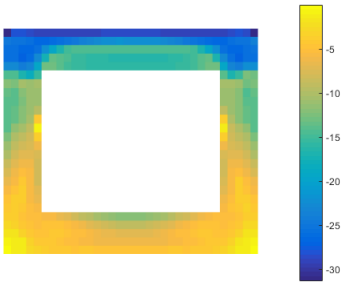

(c) σ_{xx} [MPa]

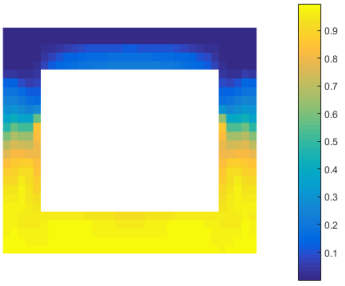

(d) Concrete Damage

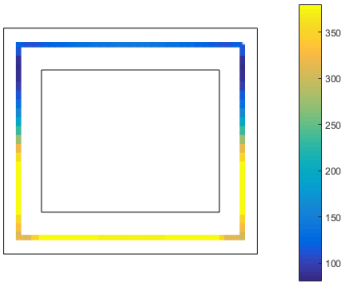

(e) σ_{st} [MPa]

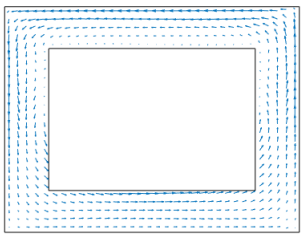

(f) Shear stress flow

Figure 4.11: Section state for ultimate load: a) Shear stresses τ_{xz}, b) Shear stresses τ_{xy}, c) Longitudinal stresses σ_{xx}, d) Concrete tensile damage, e) Stirrups stress, f) Shear stress flow

The section state at the ultimate load is shown in Fig.(4.11). Figs.(4.11a) and (4.11b) shows the shear stresses, it can be seen that the upper flange carries slightly bigger stresses than the bottom flange, this is due to the bending moment that produces compression on the upper flange, see Fig.(4.11c), and tension in the lower flange which is also fully damaged as it is shown in Fig.(4.11d); consequently, the upper flange is less damaged than the bottom one. Besides, the presence of shear stresses in the bottom flange is an evidence of the aggregate interlock phenomena. This is reproduced at the material level by means of the evolutive dilatancy parameter introduced in Poliotti, Bairán (2019). The contribution of the stirrups, see Fig.(4.11e), shows that the horizontal lower branch has fully yielded, also the vertical branches have reached the yielding stress but plasticity is not developed in its full length.

4.4.2 Study of confinement of concrete sections

As it was previously stated, the complementary displacement field reproduces the distortion of the section. This enables the model to capture explicitly the contribution of transverse reinforcements. A particular problem where this takes relevance is the case of confinement in concrete sections.

Confinement is of major importance in the design and assessment of new, existing, and repaired reinforced concrete structures, as it increases both strength and ductility. Confinement effects are consequence of the interaction between concrete and transverse reinforcement; when compression is applied to concrete, it has a transverse expansion, which is constrained by the transverse reinforcement providing the confinement pressure that increases the strength and ductility of the material. Transverse reinforcement is usually provided by steel stirrups or spirals in the case of new structures, or by steel or fiber-reinforced-polymers (FRP) jackets typically in the reinforcement of existing structures.

Classic fiber-beam models simulate confinement through 1D constitutive models that include transverse reinforcement by means

of reinforcements ratios at the material level. Currently, those constitutive laws have to be calibrated for different confining materials or for different arrangements of the transverse reinforcement Mander et al. (1988b); Bisby et al. (2005). This approach is not objective, as it masks the 3D behavior of concrete while it interacts with the confinement material. Hence, if different confinement materials are used, the model needs to be recalibrated.

In order to test the capabilities of the presented model to represent confinement in an objective manner, four concrete sections with different confining materials and arrangements are simulated under pure axial loading.

Confinement of a circular column with steel spiral

In the following, a circular section of a reinforced concrete column tested by Mander et al. (1988a) is simulated with the presented model. This specimen is the unit number 4 of a larger experimental campaign, which was the basis of the well-known 1D constitutive model for confined concrete of Mander et al. (1988b). Table (4.5) shows the material properties.

Table 4.5: Material properties validation case circular section

Concrete	f_c	28 MPa
Longitudinal Steel	f_y	295 MPa
	E_s	200000 MPa
Transverse Steel	f_y	320 MPa
	E_s	200000 MPa

The test setup can be seen in Fig.(4.12a), the interpolation grid consisting on 5 points is shown in Fig.(4.12b). The interpolation grid is set to trace the higher strain gradient that it is produced on the perimeter of the section. The fiber distribution in Fig.(4.12c) consists of 484 concrete fibers, 60 stirrup fibers and 12 fibers representing the longitudinal reinforcement. The test is performed applying axial strains in 45 increments, then the model fails to converge.

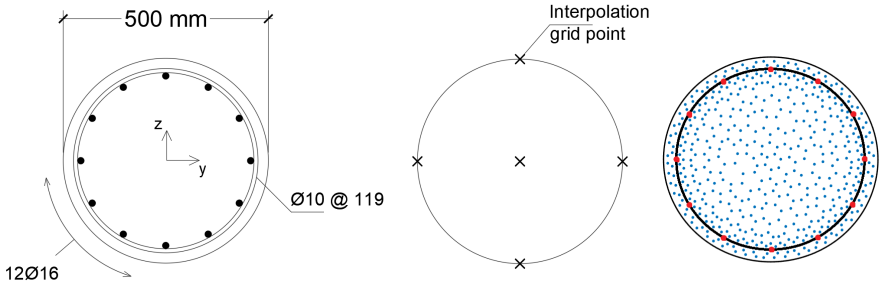

(a) (b) (c)

Figure 4.12: Specimen: a) Cross-section, b) Interpolation grid, c) Fiber distribution.

Three pairs of numerical and experimental curves are presented in Fig.(4.13a). The total axial load carried by the whole section is plotted against the axial strain, also the axial load carried by the longitudinal reinforcements and by the concrete cover are plotted as well. Fig.(4.13b) shows the predicted strains on the transverse reinforcements compared against the experimental curve.

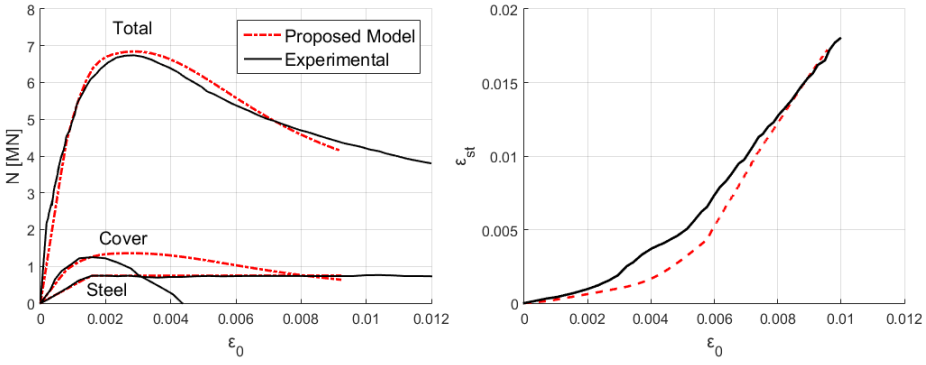

(a) (b)

Figure 4.13: (a) Axial force-strain curves. (b) Spiral strains. Experimental results by Mander et al. (1988a)

The model shows to predict in a good way the strength and the post-peak stiffness. However, it can be seen that the model fails to converge before the ultimate experimental strain is reached.

Furthermore, as the numerical model fails to converge, the strain level where hoop fracture occurs is not reached. Nevertheless, the total axial load, the load carried by the reinforcements and the strains in the transverse reinforcement have a good agreement with the experimental data. In the case of the concrete cover, it can be seen that the maximum strength is well captured but the post-peak behavior predicted by the proposed model differs from experimental evidence. This can be explained by the fact that the proposed model solves the equilibrium equations at the sectional level in a weak form as in Eq.(4.4), thus the local error in a single fiber could be greater than the error at the sectional level, as it is evidenced in this case.

Fig.(4.14a) shows the longitudinal stress field and Fig.(4.14d) shows the longitudinal stress along a radius of the section. It can be seen that longitudinal stresses are higher on the section core than on the perimeter of the section, being minimum in the section cover, this coincides with the observed response. In Fig.(4.14c) the stresses on the steel spiral are presented at the ultimate state, it can be seen that the spiral has fully yielded. Fig.(4.14b) shows the radial strains are bigger on the cover than on the core of the section, this is evidence of the existence of more damage in that region or spalling of concrete.

Fig.(4.14e) shows the confining stresses in the radial (σ_{rr}) and circumferential ($\sigma_{\theta\theta}$) directions at different distances from the center. Theoretically, these curves should be constant, but it can be seen that oscillations appear as the distance from the center increases. The reason of the oscillations is the fact that the interpolation functions in Eq.(4.15) are constructed in a Cartesian reference system rather than in a cylindrical one, which in this case would be more suitable. Nevertheless, the average σ_{rr} at radius of $r/R = 0.9$, which coincides with the position of the transverse reinforcement, is equal to $0.90MPa$. This almost coincides with the lateral confining stress predicted by Mander et al. (1988b) which was $0.85MPa$.

The proposed model shows to be able to predict well the overall behavior with a single definition of the concrete properties. In

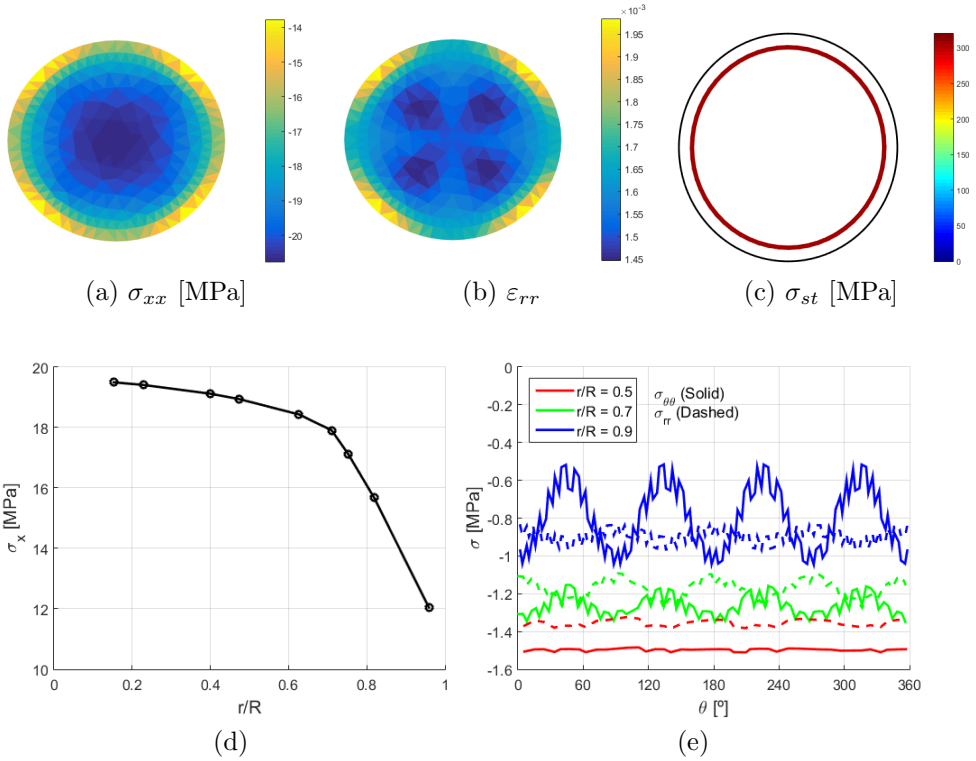

(a) σ_{xx} [MPa] (b) ε_{rr} (c) σ_{st} [MPa]

(d) (e)

Figure 4.14: Section state: a) Longitudinal stresses, b) Radial strains, c) Stirrups stresses, d) Longitudinal stresses-radius curve, e) σ_{rr} and $\sigma_{\theta\theta}$ - θ curves.

contrast, classical fiber-beam models Spacone et al. (1996b) define different zones in the cross-section with different material parameters in order to capture the confinement phenomena.

Confinement of a rectangular column with steel stirrups

A rectangular section of a reinforced concrete column tested by Mander et al. (1988a) is simulated with the presented model. This specimen is the unit number 13 of the experimental of Mander et al. (1988b). Table (4.6) shows the material properties.

The test setup can be seen in Fig.(4.15a), the interpolation grid consisting on 9 points is shown in Fig.(4.15b). The fiber distribution in Fig.(4.15c) consists of 324 concrete fibers, 84 stirrup fibers and 12 fibers representing the longitudinal reinforcement. The axial strain

Table 4.6: Material properties validation case rectangular section

Concrete	f_c	24.8 MPa
Longitudinal Steel	f_y	434 MPa
	E_s	200000 MPa
Transverse Steel	f_y	309 MPa
	E_s	200000 MPa

is applied in 90 increments when the simulation presents significant loss of the carried load.

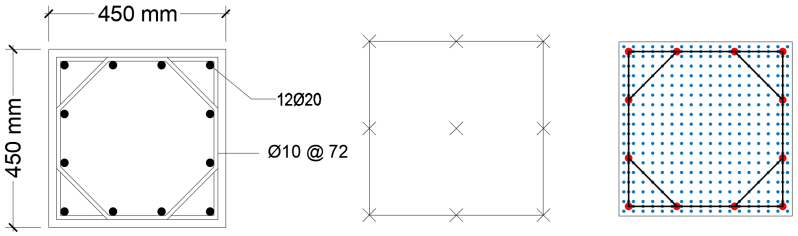

(a) (b) (c)

Figure 4.15: Specimen: a) Cross-section, b) Interpolation grid, c) Fiber distribution.

The numerical axial force-strain curve is compared against the experimental one in Fig.(4.16). Good prediction of the ultimate load is obtained. The increase on the ductility is also well captured. The analysis stopped when the internal stirrups reached its ultimate stress and softening starts to develop, as it is evident in Fig.(4.17b).

Figs.(4.17a) and (4.17c) show the behavior of the section at the ultimate load. The stress distribution shows that the non-uniform confinement is well captured by the proposed model.

Confinement of a circular section with a CFRP jacket

A circular concrete section wrapped with a CFRP sheet tested by Micelli, Modarelli (2013) is simulated with the proposed model. The specimen, named CC1, is part of a larger experimental campaign studying the behaviour of FRP confined concrete. The test setup can be seen in Fig.(4.18a), and the material properties are

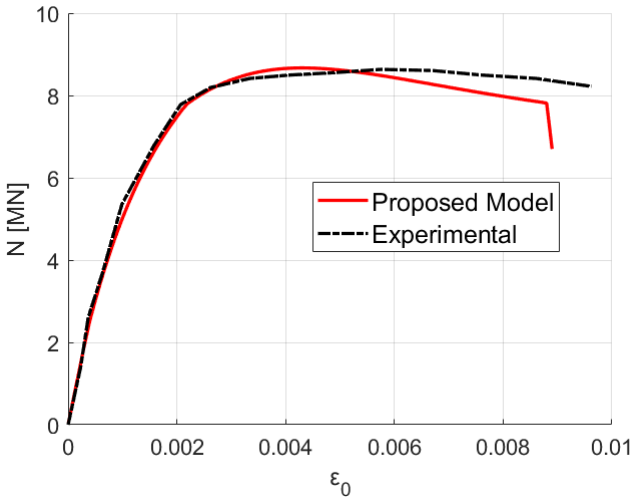

Figure 4.16: Axial force-strain curve. Experimental results by Mander et al. (1988a)

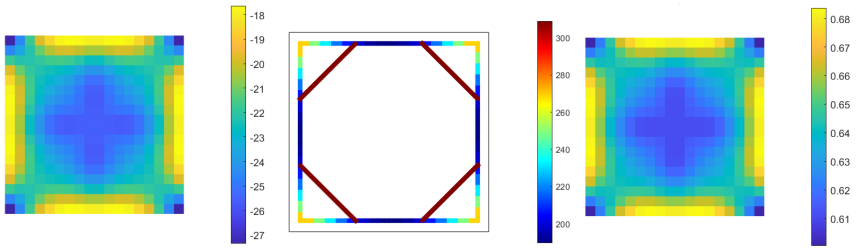

(a) σ_{xx} [MPa] (b) σ_{st} [MPa] (c) κ_c

Figure 4.17: Section state: a) Longitudinal stresses, b) Stirrup stresses, c) Compression damage in concrete fibers.

shown in Table (4.7). The interpolation points and the fiber distribution can be seen in Figs.(4.18b) and (4.18c). The axial strain is applied in 50 increments when the ultimate strain is reached.

The numerical axial force-strain curve is compared against the experimental one in Fig.(4.19). Good prediction of the ultimate load is obtained. The increase on the ductility is also well captured. The analysis stopped when the transverse jacket reached its ultimate stress and softening starts to develop, as it is evident in Fig.(4.20b), this coincides with the observed experimental failure. Hence, the model allows assessing the capacity of the element with-

Table 4.7: Material properties validation case circular CFRP section

Concrete	f_c	28 MPa
CFRP	f_u	3070 MPa
	E	221000 MPa

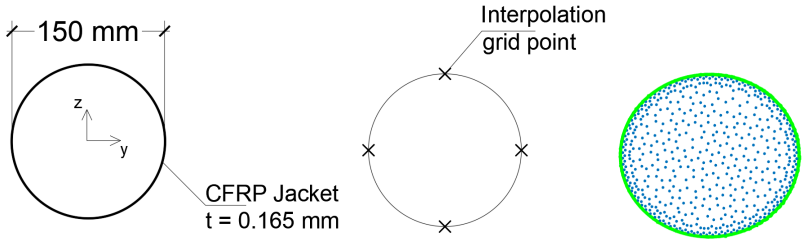

(a) (b) (c)

Figure 4.18: Specimen: a) Cross-section, b) Interpolation grid, c) Fiber distribution.

out the need of the empirical effective strain concept in the FRP Wu, Jiang (2013).

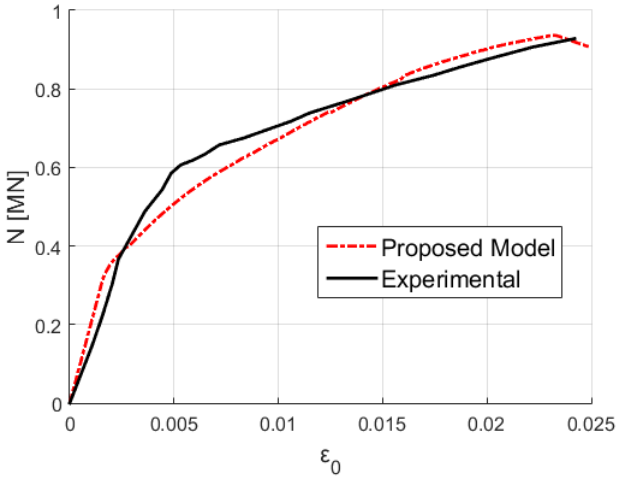

Figure 4.19: Axial force-strain curve. Experimental results by Micelli, Modarelli (2013)

Figs.(4.20a) and (4.20b) show the behavior of the section at

the ultimate load. As the confining element is on the perimeter of the section, giving a uniform confinement to the whole section, the longitudinal stresses are almost constant over the cross-section. The small variations of the stress are due to the interpolation.

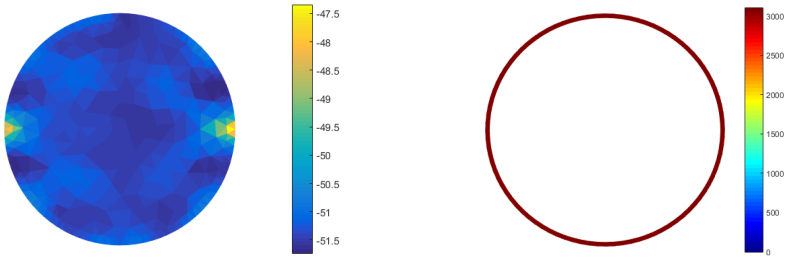

(a) σ_{xx} [MPa] (b) σ_{st} [MPa]

Figure 4.20: Section state: a) Longitudinal stresses, b)Stirrup stresses.

Confinement of a concrete filled steel tube column

In the following, a rectangular concrete filled steel tube (CFST) is simulated and compared against the experimental results of the specimen HSS1 tested by Uy (2001). The test setup can be seen in Fig.(4.21a) and the material properties are addressed in Table (4.8). The analysis is performed applying 45 axial strain increments.

Table 4.8: Material properties validation case CFST

Concrete	f_c	28 MPa
Steel jacket	σ_y	750 MPa
	E	200000 MPa
	ν	0.3

The numerical simulation is performed using the interpolation grid as in Fig.(4.21b) and the fiber distribution as in Fig.(4.21c). In the experimental test, both the steel and concrete were subjected to the axial load. To model the steel plates, a classic Von-Mises constitutive law with isotropic hardening is used.

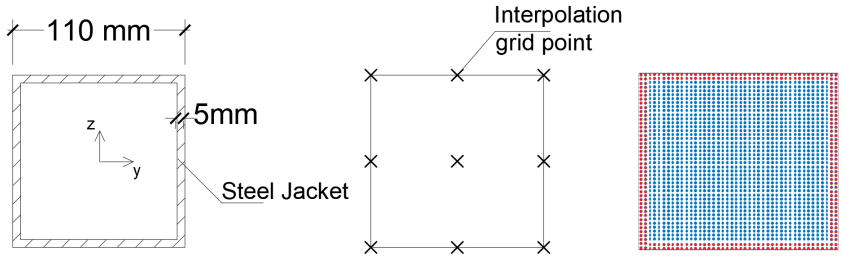

Figure 4.21: Specimen: a) Cross-section, b) Interpolation grid, c) Fiber distribution.

Fig.(4.22) shows both the numerical and experimental axial force-strain curves. Good agreement is achieved by the sectional model. The enhancement in strength and ductility is well captured.

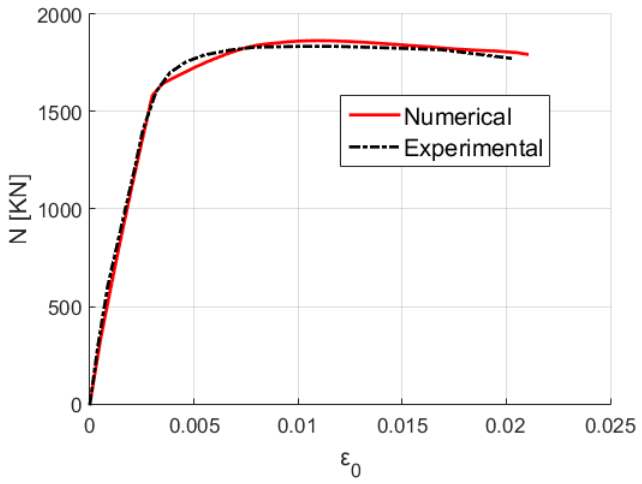

Figure 4.22: Axial force-strain curve. Experimental results by Uy (2001)

The longitudinal stresses at the ultimate state in the steel jacket and in the concrete core can be seen in Fig.(4.23a). The non-uniform confinement given by the jacket causes regions with different degrees of compressive damage in concrete, this can be seen in Figs.(4.23b) and (4.23c).

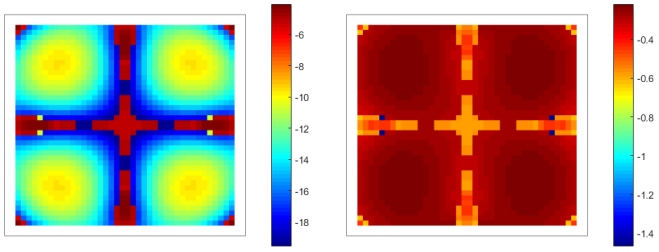

(a) σ_{xx} [MPa] (b) σ_{yy} [MPa]

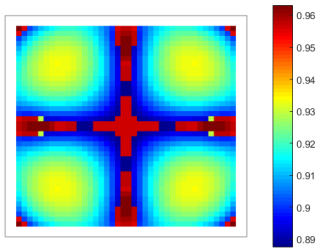

(c) κ_c

Figure 4.23: Section state: a) Longitudinal stresses, b) Transverse stresses, c) Compression damage in concrete fibers.

4.5 Closure

A new sectional model for the nonlinear analysis of reinforced concrete elements is proposed. The model is based on the original model of Bairán, Marí (2006a,b, 2007a), which proposed a formulation based on the decomposition of the displacement field of a beam into a plane-section displacement field and a complementary warping-distortion field. The complementary field is obtained by considering explicitly the inter-fiber equilibrium which in the original model was solved by means of a 2D FE model. In order to make a more efficient sectional formulation, an alternative solution is proposed in this chapter.

The displacement field is here calculated as a weighted sum of b-splines functions defined on the cross-section domain, this method avoids the FE solution reducing significantly the number of unknowns involved in the sectional problem.

The model considers a displacement field independent of the

beam-axis coordinate, which allows the formulation of a completely local model, which can be used as a cross-section constitutive model on each integration point of any standard frame formulation without the need of additional degrees of freedom at the frame level.

The model is validated through a series of experiments where the capabilities of the model are tested and compared against experimental results. It is shown that the model is able to trace the response of reinforced concrete section under complex loading until failure. Pure shear loading and coupling between torsion and bending is accurately reproduced.

A remarkable reduction in the DOFs involved in the solution compared with the FE model is obtained. This enabled the model to have significant speedups proving its lower computational demand with respect to the FE solution.

The sectional model is used to study confinement in reinforced concrete sections. As the formulation considers the distortion of the section, it is able to capture the interaction of transverse reinforcements and the concrete mass. Then confinement is simulated in an objective manner for different confining materials, section shapes and reinforcement arrangements.

The sectional model presented in this chapter constitutes an efficient framework capable of reproducing the nonlinear behavior of concrete elements under different loading states and reproducing complex failure modes. This, in conjunction with its reduced computational demand, in comparison with other solution methods, makes it suitable for the analysis of complete structures.

Chapter 5

A variable order framework for 3D nonlinear analysis of reinforced concrete frames under general loading

In this chapter, a frame model for the analysis of three-dimensional reinforced concrete structures capable of reproducing general failure modes is presented. A force-based model which guarantees the equilibrium between nodal and sectional forces is enhanced by means of a cross-sectional model. It is capable of capturing the complex coupling between all the internal forces. Consequently, different failure modes can be reproduced such as shear, torsional, flexural or axial failures. Material modeling of concrete is made using a plastic-damage model that incorporates a variable dilatancy parameter. The sectional and constitutive models are implemented in *OpenSees*. The sectional model can be used at each integration point of the force-based element. Alternatively, it can be used only where high coupling between the internal forces is expected, producing a variable order structural model, allowing the optimization of the computational effort. The validation shows that the frame element is capable of accurately reproduce the behavior of beams and columns under monotonic and cyclic loads. The framework pre-

sented is a powerful numerical instrument for the analysis, design and assessment of reinforced concrete buildings and bridges.

5.1 Introduction

Modern guidelines for seismic design or assessment of reinforced concrete buildings and bridges CALTRANS (2019); FEMA (2018); ACI Committee 341 (2007); AASHTO (2011) require nonlinear static pushover or dynamic analysis of those structures. In that sense, three dimensional finite element (FE) model is a powerful tool. However, the high computational cost of such models makes them prohibitive for the analysis of full scale structures in most practical cases. Hence, practicing engineers use one dimensional elements when analyzing reinforced concrete structures mainly composed by beams, girders or columns. Frame elements are computationally cheaper and robust. In addition, they are easy to pre- and post- process, and they are directly related to the engineers reasoning.

Classic fiber-beam models Carol, Murcia (1989); Taucer et al. (1991); Spacone et al. (1996a,b); Neuenhofer, Filippou (1997) consist on mixed or force-based frame formulations where, on each integration point the cross-section is discretized into fibers. The fibers are represented by their area and by uniaxial nonlinear constitutive laws for concrete or steel. Fiber-beam models are capable of tracing coupling between axial load and bending moments in a robust manner. Consequently, these models are able to capture axial or flexural failures accurately in many practical cases.

However, most fiber-beam models neglect the coupling between axial and tangential forces, such as shear or torsion Ranzo, Petrangeli (1998); Ceresa et al. (2007); Bairán, Marí (2007b). As a result, they are not able to reproduce shear or torsional failures. Moreover, as the presence of high shear forces affects the bending response of reinforced concrete elements Bairán, Marí (2007b), they loose accuracy on the prediction of flexural failure. Another shortcoming of these models, is that they only consider transverse

reinforcements at the material level by means of reinforcement ratios that affect the uniaxial constitutive law of concrete. In order to reproduce confinement, different material properties are defined within the same cross-section and the constitutive laws are re-calibrated for different confining materials and arrangements of transverse reinforcements. Consequently, a lost of accuracy and objectivity of fiber-beam models on the reproduction of axial load failure is produced.

Some frame models exist that take into account the shear failure of reinforced concrete elements with different degrees of accuracy and robustness. Detailed state of the art reviews were made by Ceresa et al. (2007); Bairán, Marí (2007b). More recent models were developed with aims to incorporate to fiber-beam models different failures modes such as shear or torsion in a coupled way Mohr et al. (2010); Le Corvec (2012); Li et al. (2016); Kagermanov, Ceresa (2017); Kolozvari et al. (2018); Re et al. (2018); Kagermanov, Ceresa (2018); Rajapakse et al. (2019); Nguyen et al. (2019). In most cases, this is made by enhancing the beam kinematics altogether with the use of 2D or 3D constitutive models for concrete.

In this chapter, a 3D frame model capable of tracing the response of reinforced concrete elements under general coupled loading is presented. The model involves three different levels: the element level, the cross-section level and the material point. At the frame level, the beam-column formulation introduced in Spacone et al. (1996a); Neuenhofer, Filippou (1997); Scott et al. (2004); Scott, Fenves (2006); Scott et al. (2008) is used as framework. Then, each integration point of the frame element is simulated by means of the total interaction cross-sectional model introduced in Poliotti, Bairán (2020). Further, each material point of the concrete cross-section is represented by a 3D plastic-damage model with evolutive dilatancy presented by Poliotti, Bairán (2019). The frame model is validated against experimental data available in literature. First, two reinforced concrete beams under combined bending and shear are numerically reproduced. Then, a cyclically loaded reinforced

concrete column is tested. Finally, in order to demonstrate the capability of the framework for seismic assessment in shear-sensible structures, the performance of a bridge under seismic loads is studied.

5.2 Proposed Framework

The structural analysis of a bridge or building can be divided into four levels, as it is shown in Fig.(5.1). The structural level involves the determination of global forces $\boldsymbol{Q}$, global displacements $\boldsymbol{D}$ and the structural stiffness matrix that relates them $\boldsymbol{K}$. These variables are obtained by a proper assembly of nodal forces $\boldsymbol{q}$, nodal displacements $\boldsymbol{d}$ and element stiffness $\boldsymbol{K_e}$, respectively.

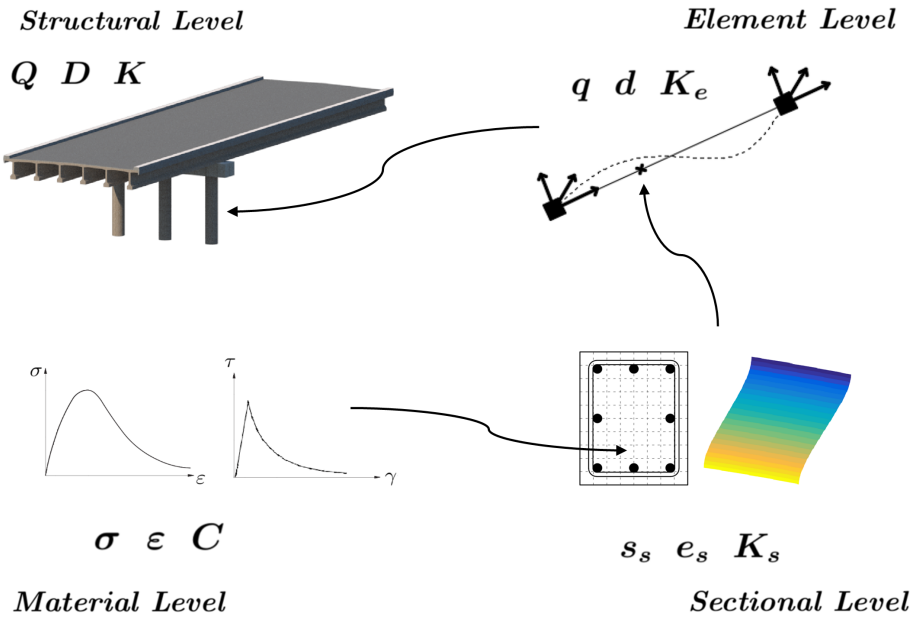

Figure 5.1: Proposed Framework

Each column, beam or girder, in most cases, can be represented by a frame element with two nodes. In a general 3D structure, the degrees of freedom on each node are three displacements and three rotations. The corresponding forces of the element are three forces and three moments on each node. At the element level, equilibrium

between nodal forces and internal forces is verified. In order to do so, a proper sectional constitutive relation is required.

The sectional level deals with equilibrium within the cross-section at each integration point of the frame element. It relates the sectional or internal forces $\boldsymbol{s_s}$, with the generalized sectional deformations $\boldsymbol{e_s}$, see Eq.(5.1).

$$\begin{aligned} \boldsymbol{s_s} &= \{N\ V_y\ V_z\ T\ M_y\ M_z\}^T \\ \boldsymbol{e_s} &= \{\varepsilon_0\ \gamma_{0y}\ \gamma_{0z}\ \phi_x\ \phi_y\ \phi_z\}^T \end{aligned} \tag{5.1}$$

where ε_0 is the axial elongation; γ_{0y} and γ_{0z} are the generalized shear deformations; and ϕ_x, ϕ_y and ϕ_z are the torsional and bending curvatures, respectively. A sectional stiffness matrix $\boldsymbol{K_s}$ is needed to perform the element state determination. $\boldsymbol{K_s}$ is a 6x6 matrix that, in general, is full, when full coupling of the six internal forces is accounted for.

The material level represents the description of the local response at a differential point. The variables are stress $\boldsymbol{\sigma}$ and strain $\boldsymbol{\varepsilon}$ tensors, and the material tangent matrix, $\boldsymbol{C}$. Depending on the constitutive model used, other internal variables are involved, such as plastic strains or damage variables. In a general 3D case, the concrete model needed to reproduce a general failure mode has to be triaxial.

In this chapter, the problem of reproducing the response of a structure under general loading with different failure modes is tackled in a multilevel scheme, with 3 levels. At the element level, a force-based formulation that ensures the equilibrium between nodal and sectional forces is used. At the sectional level, a model that captures the coupling between the six internal forces while considering both longitudinal and transverse reinforcement is used. Finally, at the material level a 3D constitutive law for concrete is used to simulate the material behavior. In the following the models for the element, sectional and material levels are presented.

5.2.1 Beam-column formulation

The beam-column model developed in Spacone et al. (1996a); Neuenhofer, Filippou (1997); Scott et al. (2004); Scott, Fenves (2006); Scott et al. (2008) and implemented in McKenna et al. (2010) is used at the element level. Assuming that there are no loads applied on the element, the force or flexibility approach consists on obtaining the force field as in Eq.(5.2).

$$\boldsymbol{s_s}(x) = \boldsymbol{b}(x)\,\boldsymbol{q} \tag{5.2}$$

where $\boldsymbol{b}(x)$ contains the force interpolation functions that relates the nodal forces $\boldsymbol{q}$ with the internal forces on each cross-section $\boldsymbol{s_s}(x)$. The proper choice of the interpolation function leads to a strict satisfaction of equilibrium between nodal forces and section forces. The model requires the definition of a sectional constitutive relation that is written in an incremental way, as shown in Eq.(5.3).

$$\Delta\boldsymbol{e_s}(x) = \boldsymbol{f_s}(x)\,\Delta\boldsymbol{s_s}(x) = \boldsymbol{f_s}(x)\,\boldsymbol{b}(x)\,\Delta\boldsymbol{q} \tag{5.3}$$

where $\boldsymbol{f_s}(x) = \boldsymbol{K_s^{-1}}(x)$ is the sectional flexibility matrix. A compatibility condition between nodal displacement and sectional deformations can be written in a weak form, as in Eq.(5.4).

$$\boldsymbol{d} = \int_0^L \boldsymbol{b}^T(x)\,\boldsymbol{e_s}(x)\,dx \tag{5.4}$$

Following this approach, the element flexibility matrix that relates the nodal displacements with the nodal forces can be obtained as in Eq.(5.5).

$$\boldsymbol{F_e} = \int_0^L \boldsymbol{b}^T(x)\,\boldsymbol{f_s}(x)\,\boldsymbol{b}(x)\,dx \tag{5.5}$$

where $\boldsymbol{F_e} = \boldsymbol{K_e^{-1}}$.

Two different procedures for the element state determination were proposed by Spacone et al. (1996a) and Neuenhofer, Filippou (1997). The proposed state determination in Spacone et al. (1996a) iteratively computes the element forces and stiffness matrix while

enforcing the element equilibrium and compatibility. In contrast, the algorithm proposed in Neuenhofer, Filippou (1997) avoids the iterative procedure by introducing the residual nodal displacement in the force determination.

It can be seen in Eqs.(5.3) to (5.5) that the ability of reproducing any type of coupling between the internal forces relies directly on the sectional model. The cross-section discretization into uniaxial fibers is the most classical sectional model in the nonlinear analysis of reinforced concrete structures. This model robustly captures the axial-bending interaction while neglecting the coupling with tangential internal forces.

5.2.2 Sectional model

The cross-sectional model used in this framework is based on the displacement decomposition introduced in Bairán, Marí (2006a,b). The displacement field that follows the plane section hypothesis $\boldsymbol{u}_{ps}$ is enhanced by means of a complementary displacement field that incorporates distortion and warping $\boldsymbol{u}_w$, see Eq.(5.6).

$$\boldsymbol{u} = \boldsymbol{u}_{ps} + \boldsymbol{u}_w = \left\{ \begin{array}{c} u_{ps} \\ v_{ps} \\ w_{ps} \end{array} \right\} + \left\{ \begin{array}{c} u_w \\ v_w \\ w_w \end{array} \right\} \tag{5.6}$$

The complementary field is determined by means of solving the three-dimensional equilibrium equations at the sectional level. The 3D stress and strain states are obtained on each material point of the cross section. As a result, the model is capable of reproducing the coupling of the six sectional internal forces for a general anisotropic material behavior as is the case of cracked concrete.

The three-component complementary field is capable of reproducing the in-plane stretching of the cross section. Thus, the model includes explicitly the transverse reinforcements as stirrups or jackets. Considering the transverse reinforcements is crucial to reproduce shear or torsional failures. In addition, the interaction between stirrups or jackets with the surrounding concrete is the source of

confinement. Therefore, confinement is reproduced naturally without the need of defining different constitutive law or material parameters on the same cross-section.

The numerical solution of the sectional equilibrium equations requires discretization of the complementary field. In Bairán, Marí (2006a,b) a FE model of the cross-section is used, see Eq.(5.7). In that FE context, $\boldsymbol{N}_w(y,z)$ represents the sectional interpolation matrix shape functions, and $\boldsymbol{d}_w$ is the vector of complementary nodal displacements.

$$\boldsymbol{u}_w = \boldsymbol{N}_w(y,z)\,\boldsymbol{d}_w \tag{5.7}$$

The sectional model is capable of reproducing in a consistent manner axial, shear, torsion and bending failures as well as coupled failures, as it was demonstrated in Bairán, Marí (2006a,b, 2007a). The main shortcoming of this model is its computational demand. The model was modified in chapter 4 and in Poliotti, Bairán (2020) replacing the FE discretization by means of pre-defined functions on the cross-section domain, particularly in chapter 4 b-splines functions are used. There, the interpolation matrix $\boldsymbol{N}_w(y,z)$ contains the b-splines shape functions, and the vector $\boldsymbol{d}_w$ are the weights factors of the b-spline interpolation and represent the additional internal degrees of freedom of the section.

This numerical technique reduces significantly the number of degrees of freedom involved in the solution of the sectional problem, while the accuracy remains on the same level as in the original sectional model in Bairán, Marí (2006a,b, 2007a). Hence, the reduced computational demand of the b-spline sectional model makes it more suitable for the analysis of complete structures.

The sectional model introduced in chapter 4 is used as response model on the integration points of the frame formulation described before. The model proved to capture the sectional behavior in a consistent manner, with a reduced computional demand. Further details of the model can be found in Bairán, Marí (2006a,b, 2007a,b); Poliotti, Bairán (2020).

5.2.3 Concrete constitutive model

Concrete is a complex material that exhibits several nonlinear phenomena. Within the same structure, there are different elements that may be under a wide range of loading conditions. Beams under high shear forces or columns with high levels of axial force and confinement are evidence of this. The sectional model presented in the previous section requires a 3D constitutive law. As the model aims to capture different failure modes, the constitutive equation has to be able to reproduce different stress conditions in a consistent manner.

The 3D plastic-damage model for concrete introduced in Lubliner et al. (1989); Lee, Fenves (1998) and then implemented in ABAQUS (2012) reproduces many of the main characteristic of concrete behavior. The model in Lee, Fenves (1998) introduces two internal variables, one for tension and other compression, that play the role of hardening variables in a classic plasticity theory. Each one is defined as a measure of the dissipated energy during an uniaxial inelastic process. In a tensile case, the dissipated energy is the fracture energy; in a compressive case, it is the so-called crushing energy. Both are normalized by means of a localization length to ensure mesh objectivity. Also, an isotropic stiffness degradation variable is introduced to reproduce damage. The evolution is governed by a non-associative flow rule that controls dilatancy by means of a single and constant parameter α_p.

Dilatancy can be understood as the volume change of a granular material under shear strains. It affects the shear behavior of the material but also its transverse expansion. In chapter 3 and in Poliotti, Bairán (2019), it was shown that a constant parameter fails to provide an objective description of the dilatant behavior. Hence, the original model needed specific calibration for different applications. To overcome this issue, a variable dilatancy parameter was introduced in chapter 3. In this chapter, each concrete material point of each cross-section is simulated using the proposed model in 3. The variable dilatancy parameter depends on the plastic-damage state $\boldsymbol{\kappa}$ and on the effective stress state $\bar{\boldsymbol{\sigma}}$ as in Eq.(3.23).

The dilatancy parameter is equal to zero for low levels of damage. Once dilatancy is activated it increases until it reaches its maximum value $\alpha_{p,max}$, as it can be seen in Fig.(5.2). The presences of confinement reduces the effect of dilatancy. Thus, the maximum value $\alpha_{p,max}$ is made dependent on the confinement level through the first invariant of the stress tensor I_1, see Fig.(5.2).

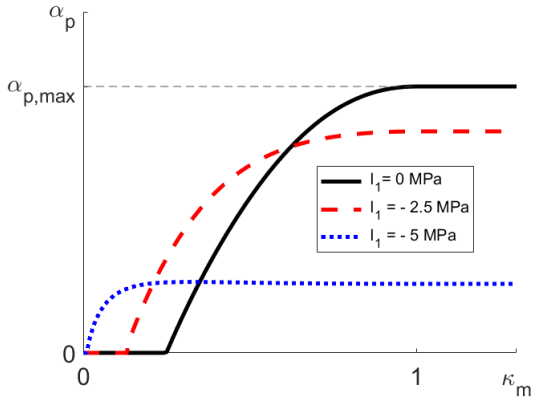

Figure 5.2: Dilatancy evolution with damage and confining pressure

The evolution of dilatancy is controlled by two material parameters: the maximum dilatancy ψ^{max} and internal friction ϕ^{max} angles. The evolutive dilatancy governs the shear softening and the nonlinear expansion of concrete without re-calibration of the material parameters. Thus, the constitutive model is suitable for reproducing shear failure and passive confinement in an objective manner. Further details on the constitutive model can be found in chapter 3.

5.2.4 Implementation

The sectional and constitutive models are implemented on the object-oriented software OpenSees McKenna et al. (2010). The plastic-damage model for concrete is implemented as a *NDMaterial* subclass of order six. The sectional model is implemented as a *SectionForceDeformation* subclass of order six. Both models can be used together with the *forceBeamColumn* element that corresponds to the frame formulation described in section 5.2.1. See Fig.(5.3).

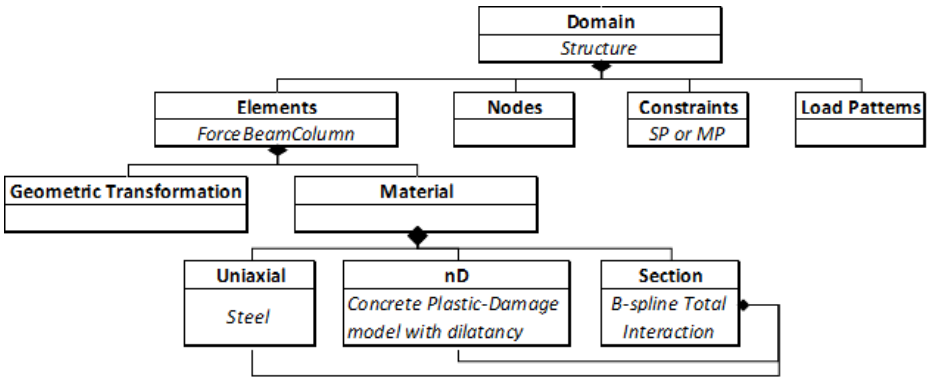

Figure 5.3: Software structure

Thanks to the object-oriented structure of the software, different sectional models can be used within the same element. In this way, the sectional model presented in section 5.2.2 can be used where shear forces have a greater influence while on the rest of the sections a classic fiber discretization can be used. Thus, the computational resources can be optimized concentrating the effort on those regions where the more complex behavior occurs. In addition, several integration methods are available for the frame element Scott, Fenves (2006); Scott, Hamutçuoğlu (2008).

It is a well-known fact that force-beam elements tend to localize deformations when softening takes places Coleman, Spacone (2001); Scott, Hamutçuoğlu (2008). This leads to a loss of objectivity and both the element and sectional responses depend on the number of integration points. To overcome this issue, in this work the energy regularization proposed by Coleman, Spacone (2001) is used. The concrete-plastic damage model introduced in section 5.2.3 already considers a characteristic length, which is made equal to the integration point length.

5.3 Validation

Three validation cases are presented to test the capabilities of the proposed framework. First, two beams belonging to the same experimental campaign carried out by Vecchio, Shim (2004) are nu-

merically reproduced. Then, a reinforced concrete column cyclically loaded tested by Lynn et al. (1996) is simulated.

The following hypotheses are common to all cases: perfect bond is assumed between the reinforcements and the concrete mass. The longitudinal and transverse steel reinforcements are simulated using the *Giuffré-Menegotto-Pinto* uniaxial constitutive model with isotropic strain hardening Filippou et al. (1983).

The material parameters needed to define the concrete behavior are obtained from the reported data on the corresponding experimental campaigns. Those parameters not addressed by the test authors are estimated as proposed in Poliotti, Bairán (2019).

5.3.1 Reinforced concrete beams

The response of two simply supported reinforced concrete beams tested by Vecchio, Shim (2004) is simulated with the proposed model. The selected specimens, named A1 and A3, were monotonically loaded by means of a single load applied in the mid-span. The geometry and reinforcement arrangements of the test can be seen in Fig.(5.4). Materials properties of the reinforcement and concrete are presented in Tables (5.1) and (5.2), respectively.

Table 5.1: Reinforcement properties Vecchio, Shim (2004)

Bar Size	Diameter [mm]	f_y [MPa]	f_u [MPa]	E_s [MPa]
M10	11.3	315	460	200000
M25	25.2	445	680	220000
M30	29.9	436	700	200000
D4	3.7	600	651	200000
D5	6.4	600	649	200000

Taking into account the symmetry of the test, only half of the beams is modeled using a single element. The integration of the element response is made by means of three Gauss-Lobato integration points. The sectional model requires the definition of an interpolation grid to construct the b-spline interpolation functions.

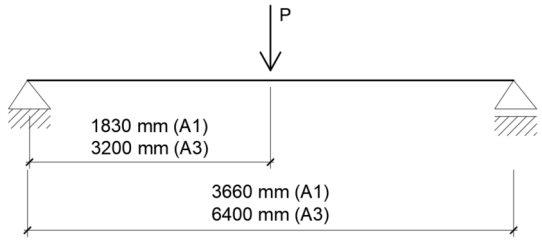

(a) Geometry A1 and A3

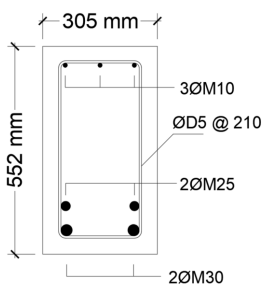

(b) Cross-section A1

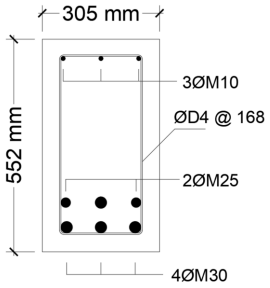

(c) Cross-section A3

Figure 5.4: Vecchio, Shim (2004) test setup. Specimens A1 and A3

Table 5.2: Concrete properties Vecchio, Shim (2004)

Beam	f_c [MPa]	ε_0
A1	22.6	0.0016
A3	43.5	0.0019

In both beams, 24 points are used to define the interpolation grid at the sectional domain, as it is shown in Fig.(5.5a). The fiber distribution of both beams can be seen in Figs.(5.5b) and (5.5c). A total of 128 concrete material points are used on each cross-section; 32 fibers represent the transverse reinforcements; 7 and 9 fibers represent the longitudinal reinforcement in A1 and A3 specimens, receptively. To simulate the test loading conditions, the mid-span vertical displacement is imposed in several steps.

The experimental response reported in Vecchio, Shim (2004) is compared against the load-deflection curves obtained with the proposed model for each specimen, see Figs.(5.6) and (5.8) . In addition, two numerical responses obtained with beam models devel-

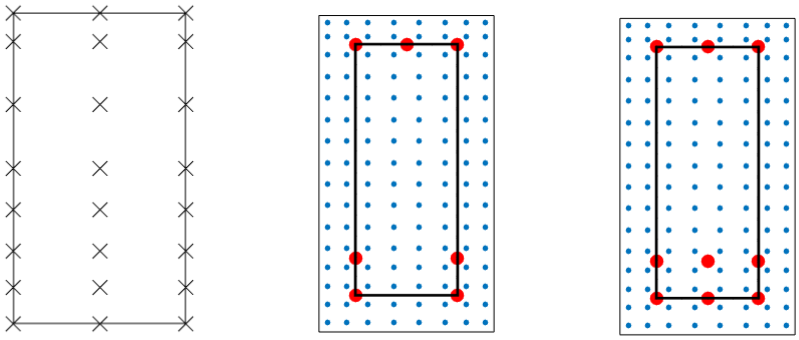

(a) Interpolation grid

(b) Fiber distribution A1

(c) Fiber distribution A3

Figure 5.5: Modeling details at the section domain of specimens A1 and A3

oped by other authors are presented. In Saritas, Filippou (2009b), a plastic-damage model with constant dilatancy is properly condensed to be used in a mixed frame element. The 2D frame element in Mohr et al. (2010) uses a sectional model that takes into account the inter-fiber equilibrium with a rotating smeared-crack constitutive model.

A very good agreement with the experimental response is obtained with the proposed model. Both the stiffness and ultimate load are well estimated. The softening branch on the response of specimen A1, is numerically captured even that a smaller ultimate displacement is predicted. In the case of A3, the analysis lost convergence after the initiation of the softening branch. It can be seen that the combined use of the plastic-damage model presented in Poliotti, Bairán (2019) and with the sectional model in Poliotti, Bairán (2020) results in an improvement with respect to the other frame elements. The model in Mohr et al. (2010) and the proposed model are both able to accurately trace the stiffness of the element. This is due to the fact that both models consider shear and flexural interaction at the sectional level. In addition, using the constitutive model in Poliotti, Bairán (2019) represents an improvement as it is also able to capture shear softening.

Notice that the two beams have identical cross-section dimen-

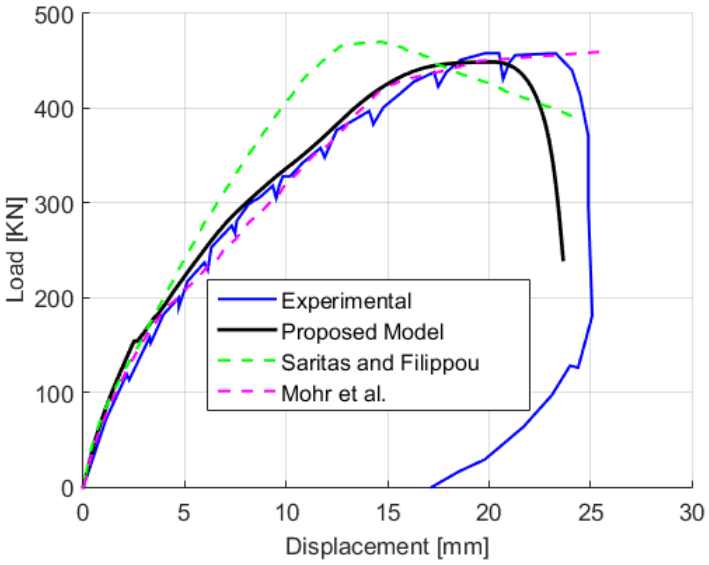

Figure 5.6: Load-displacement curve for VS-A1 specimen. Experimental by Vecchio, Shim (2004)

sions while they differ on the span length and on the amount of reinforcements. On the experimental campaign, the shorter beam A1 exhibited a shear type failure while specimen A3 had a flexural type. It can be seen that the proposed model is able to capture both failure modes.

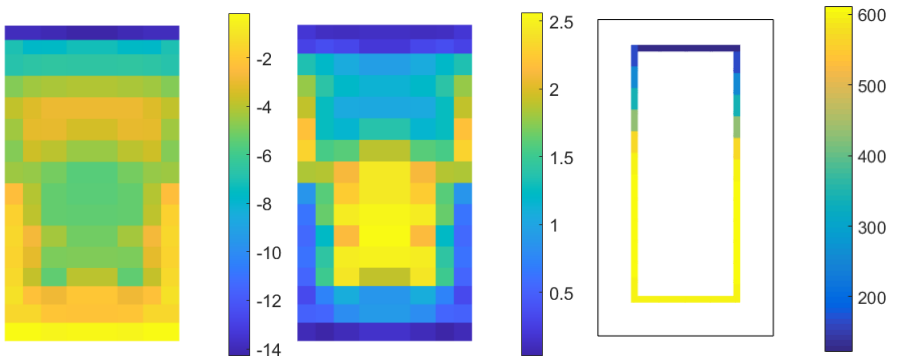

(a) σ_{xx} [MPa] (b) τ_{xz} [MPa] (c) σ_{st} [MPa]

Figure 5.7: Sectional state A1. Section located at 0.25L. Maximum load.

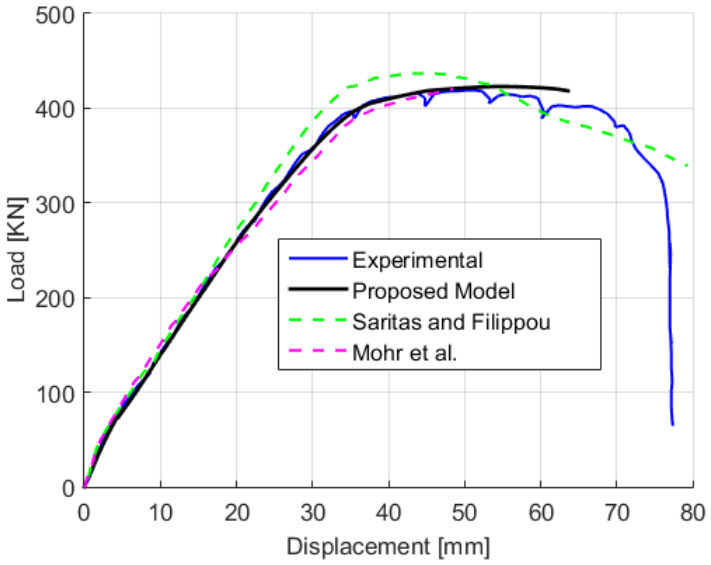

Figure 5.8: Load-displacement curve for VS-A3 specimen. Experimental by Vecchio, Shim (2004)

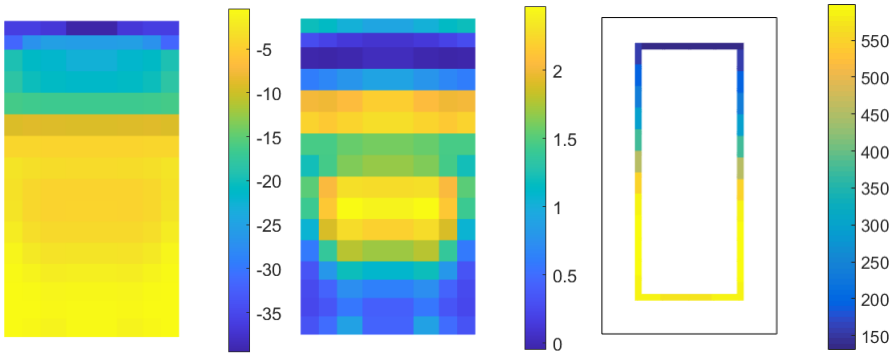

(a) σ_{xx} [MPa] (b) τ_{xz} [MPa] (c) σ_{st} [MPa]

Figure 5.9: Sectional state A3. Section located at 0.25L. Maximum load.

In Figs.(5.7) and (5.9) the state of a section located at $0.25L$ at the maximum load is presented. The different failure modes are reflected on the sectional state. The longitudinal stress distribution on both beams are different. In Fig.(5.7a), specimen A1 shows a well defined region in the cracked part of the cross-section with compressive stresses, which can be interpreted as the projection of

a compression strut intersecting the section. The stress distribution of specimen A3 in Fig.(5.9a) is closer to a pure bending case, showing that in this case shear forces have a smaller influence. In addition, Figs.(5.7c) and (5.9c) show that on the vertical branches of the stirrups in beam A1 the yielding stress is reached while in the case of specimen A3 the stresses in the transverse reinforcement are on the elastic range ($f_y = 600\ MPa$).

5.3.2 Reinforced concrete column

The cyclic test of a reinforced concrete column in Lynn et al. (1996) is simulated with the proposed framework. Specimen 2CLH18 was first submitted to an axial load of $N = 503KN$ which remained constant during the rest of the test. Afterwards, the horizontal displacement at the top of the column was imposed in three cycles for different increments exceeding the yielding displacement. The geometry, reinforcement arrangements of the cross-section and boundary conditions are shown in Fig.(5.10). Concrete and steel material properties are presented in Table 5.3.

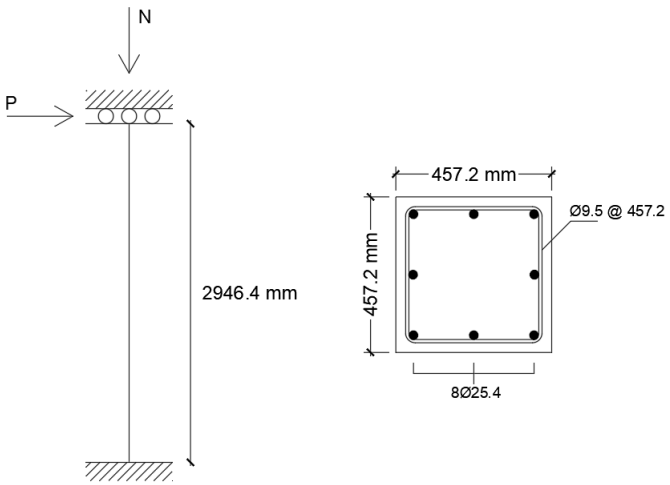

Figure 5.10: Test setup specimen 2CLH18 Lynn et al. (1996).

Thanks to the symmetry of the test, only one half of the column is modeled using a single element. The integration of the el-

Table 5.3: Material properties Lynn et al. (1996)

Concrete			
f_c [MPa]	E_c [GPa]	ε_0	f_t [MPa]
33.1	28.77	0.002	2.2

Steel		
f_y long. [MPa]	f_y trans. [MPa]	E_s [GPa]
331	400	200

ement response is made by means of six Gauss-Lobato integration points. The interpolation grid in the cross-section domain consist of 4 points, corresponding with the corners of the cross-section, see Fig.(5.11a). The fiber distribution that can be seen in Fig.(5.11b) comprises 100 concrete fibers, 32 and 8 fibers for the transverse and longitudinal reinforcements, respectively.

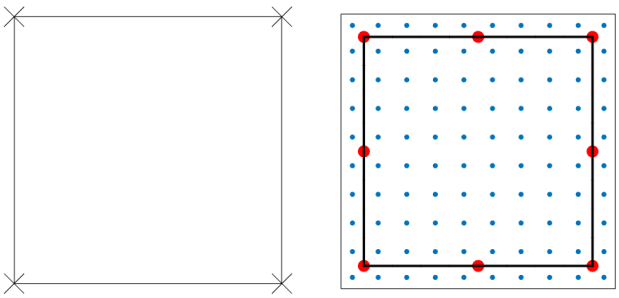

(a) Interpolation grid (b) Fiber distribution

Figure 5.11: Modeling details of specimen 2CLH18

Fig.(5.12) shows both the experimental and predicted load-displacement responses of the column. The overall behavior is suitably captured. The maximum strength of the column is well captured, as well as the ductility at the initiation of softening. The differences between experimental and simulated responses can be explained as follows. The tested column exhibited a strength loss on the last cycle due to the buckling of longitudinal bars. In addition, the experimental behavior shows more pinching, which is attributed to bond slip of the reinforcement. Neither the buckling of bars or the bond-slip effect are taken into account by the proposed model.

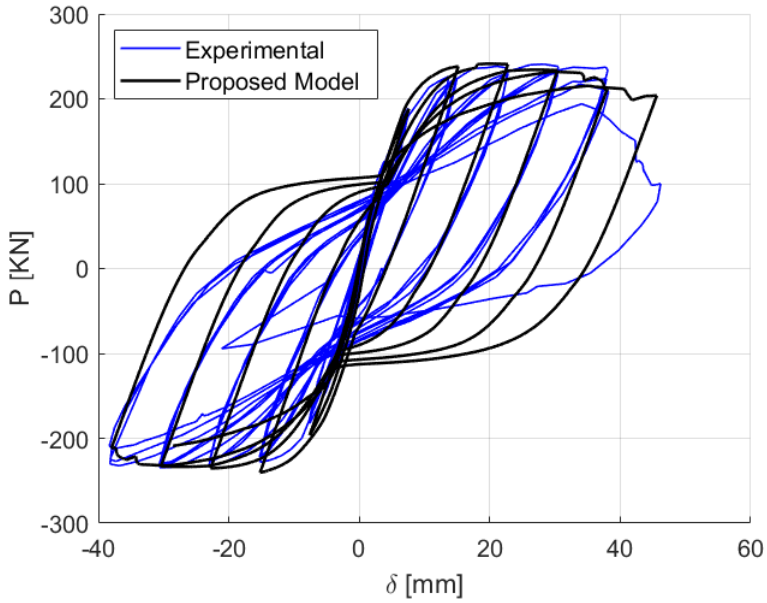

Figure 5.12: Load-displacement curve for 2CLH18 specimen. Experimental by Lynn et al. (1996)

Fig.(5.13) presents the simulated moment, curvature and shear deformation distribution on the upper half of the column for three different levels of top displacement. It can be seen that curvatures tend to concentrate on the upper region which matches with the experimental observations reported in Lynn et al. (1996). The maximum moment is almost identical on the displacements levels of $\delta = 15.20mm$ and $\delta = 30.30mm$ while on the last cycle $\delta = 45.25mm$ presents a strength loss of 11%.

The sectional state at the last level of top displacement can be seen in Fig.(5.14). Fig.(5.14d) shows stresses on the longitudinal reinforcement, it is noticeable that the top and bottom bars have all reached the yielding stress. Stresses on the stirrups are presented in Fig.(5.14c), the model does not predict yielding of the transverse reinforcement. Experimental observations report that yielding of the stirrups took place on the last cycle of the test. This difference can be explained by the fact that the transverse reinforcement is taken into account by the model in a smeared way while in the

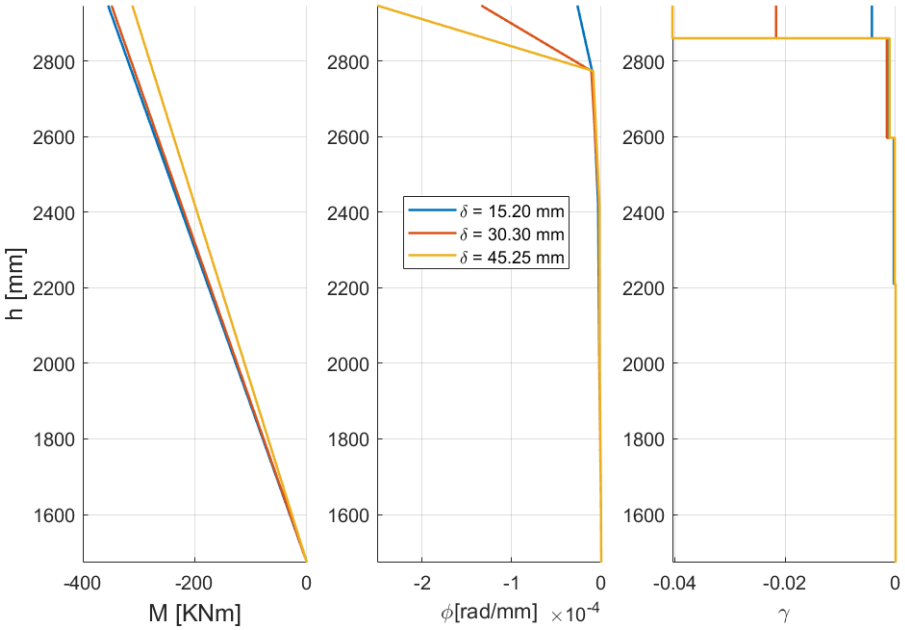

Figure 5.13: Moment, curvature and shear deformations distributions on the upper part of the column.

column stirrups are located at discrete positions. The measured strains on the experiment depend on how many discrete cracks have crossed the section, while the values obtained with the proposed model are smeared. Figs.(5.14a-5.14b) present the longitudinal and transverse stress distribution on the cross section which correspond to the stresses distributions of a flexural failure. Even that the model can be improved by including other effects such as bond slip, the obtained response constitutes a good approximation and shows the capabilities of the model to handle dynamic loading conditions.

5.4 Application: Seismic performance of a road bridge

The seismic performance of a two-30m-span bridge is analyzed using the proposed framework. Each span is formed by six simply-supported precast prestressed I girders; the bent comprises three circular columns of 1.20 m diameter and a cap beam; each end of

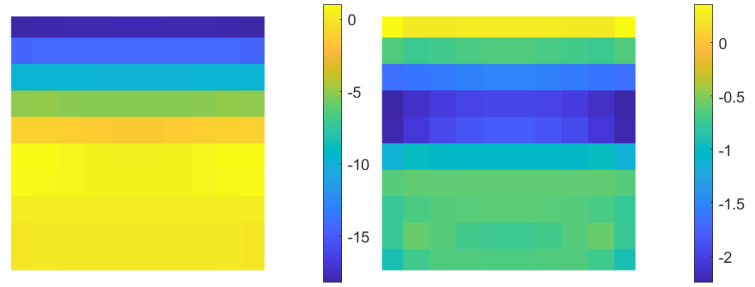

(a) σ_{xx} [MPa] (b) τ_{xz} [MPa]

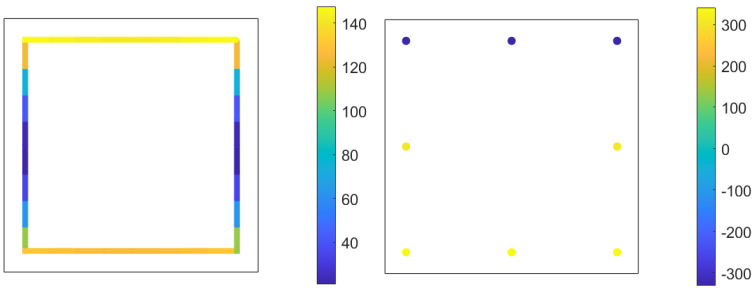

(c) σ_{st} [MPa] (d) σ_s [MPa]

Figure 5.14: Sectional state at $\delta = 45.25$mm

the bridge has spill-through abutments to support the deck. See Fig.(5.15).

The bridge is simulated using only frame elements, the deck slab is replaced by a diaphragm constraint, see Fig.(5.16). The abutments are represented by zero-length elements that take into account neoprene bearings stiffness, gaps, shear keys and the soil embankment behind the abutment, following the guidelines in CALTRANS (2019). The nonlinear behavior is expected to concentrate on the bent columns. Thus, girders and the cap beam are modeled using elastic elements. Furthermore, the connection between girders and the cap beam is made with two-node links taking into account the bearing flexibility, gaps, and shear keys. The mass of the deck is considered as additional distributed mass on the girder elements.

Each column is simulated by means of two force-based elements with four Gauss-Lobato integration points. One b-spline section

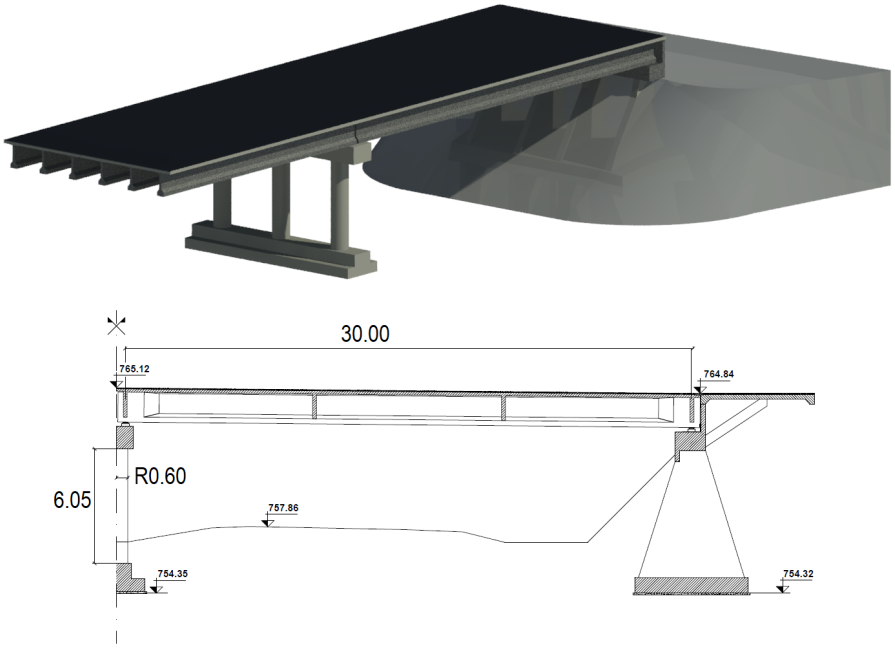

Figure 5.15: Analyzed bridge

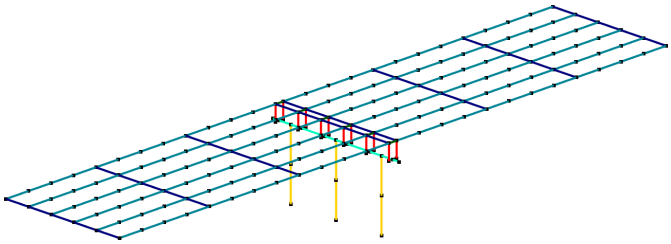

(a) Bridge mesh

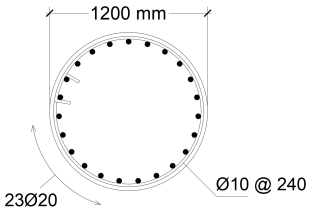

(b) Column cross-section

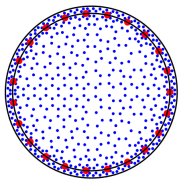

(c) Fiber distribution

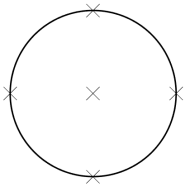

(d) Interpolation grid

Figure 5.16: Bridge model

and 3 classic fiber models are used in each element. This is made in order to reduce the computational effort. The b-spline sections are located outside the D region of the element, where the shear failure may occur. The column reinforcement is defined in Fig.(5.16b). Concrete strength is $f_c = 30\ MPa$ and steel yielding stress is $f_y = 420\ MPa$. The cross-section is discretized into 508 concrete fibers, 70 transverse reinforcement fibers and 23 longitudinal reinforcement fibers, see Fig.(5.16c). Five points are used to construct the b-spline interpolation functions as it is shown in Fig.(5.16d).

The structure is subjected to the three component earthquake signal of the Chi-Chi 1999 event. The record is first scaled to match the maximum effective acceleration of $0.35g$, which corresponds to the return period of 475 years at the site. Then, in order to study the bridge performance, the nonlinear time history analysis is made for six intensities of the same earthquake representing different return periods ranging from 43 to 2475 years. Table 5.4 presents the different seismic intensities used in the analysis of the bridge.

Table 5.4: Seismic intensities

Return Period [years]	Annual Frequency	Intensity a_G [g]
43	0.02326	0.10
72	0.01389	0.14
108	0.00926	0.17
475	0.00211	0.35
1033	0.00097	0.48
2475	0.00040	0.64

Fig.(5.17) presents the maximum displacements in the longitudinal and transversal directions on the top of the central column for each one of the analyzed intensities. The analysis is also made with a classic fiber beam model in order to compare both simulations. It can be seen that both models predict a similar response on the longitudinal direction while, on the transverse one, the proposed model predicts bigger displacements. This is a consequence of considering additional deformations induced by shear damage in

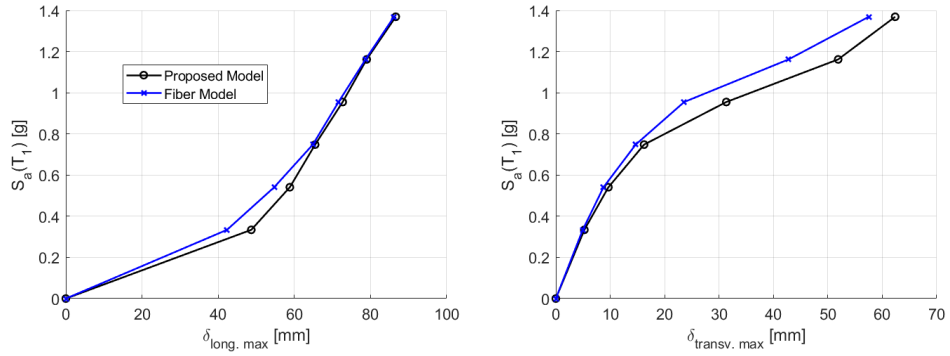

(a) Longitudinal (b) Transversal

Figure 5.17: Incremental dynamic analysis response

the column. The influence of shear deformations is greater on the higher intensities.

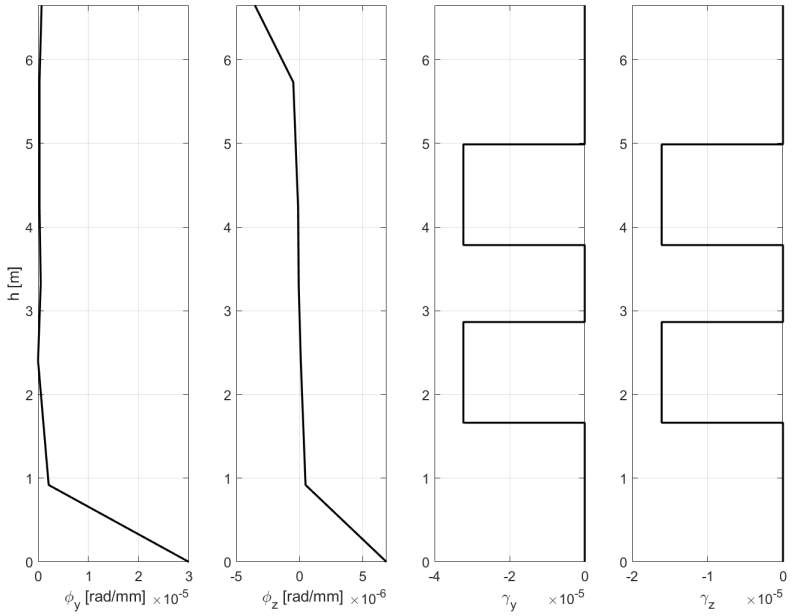

Figure 5.18: Central column deformations at maximum displacement

Fig.(5.18) presents the curvatures and shear deformations distribution on the central column height for the fifth intensity at the maximum displacement. It can be seen that curvatures tend to con-

centrate on the bottom sections for the longitudinal direction where the column acts as a cantilever column while on the transverse direction a double curvature profile is obtained. With regards to the shear deformations, they are only obtained on the b-spline sections while on the classic fiber models they are not calculated. The framework shows to be able to provide more information than classic models, such as shear deformations, concentration of damage, that improve decision taking in the design and assessment process.

5.5 Closure

A new framework for the analysis of frame structures under general loading is proposed. The framework is based on three levels: element, sectional and concrete constitutive levels. The combined use of the presented models enables the numerical reproduction of different failures modes such as flexural, shear, torsion or axial, as well as coupled modes. Furthermore, as it explicitly considers the transverse reinforcement, it can naturally reproduce the effect of confinement and the steel contribution on the shear strength.

Validation shows that the model fits well the experimental data for beams and columns under monotonic and cyclic loads. Consequently, the same framework can be used in all the elements of a complete structure. Furthermore, as the element allows the use of different sectional models on the integration points, the framework gives the user the flexibility to use the more refined sectional model only where coupling between the internal forces is more important or where local sectional information is needed.

Even that the frame model and sectional models can be used with any 3D constitutive model, the use of a proper material model shows to be crucial for reproducing different failures modes in a consistent way.

The study of a bridge performance shows that the model is robust and that is able to analyze full-scale structures. The model can be used to make performance assessments including all the possible failures modes. This, cannot be done with classic fiber-beam mod-

els showing the major improvement of the presented framework.

Chapter 6

Conclusions

6.1 Summary

In this thesis the development of a novel numerical tool for the simulation of three-dimensional line elements under general loading has been addressed. The robustness and efficiency of the models was the main focus of this study.

At the sectional level, emphasis was made in the enhancement of the model presented by Bairán, Marí (2006a). It was demonstrated that the proposed model is able to reproduce the complex cross-sectional behavior of reinforced concrete elements. A new integration technique has been used in this thesis to replace the finite element solution at the sectional level, reducing the degrees of freedom involved in the solution.

At the constitutive level, the capabilities of the well-known plastic-damage model developed by Lubliner et al. (1989); Lee, Fenves (1998), have been extended by means of a new dilatancy control. As it was demonstrated, the proper representation of the dilatancy phenomenon is crucial for the accurate simulation of the material response.

The sectional and constitutive models have been incorporated to a frame formulation that ensures the equilibrium and compatibility at the element level. The models have been implemented into an open-source and collaborative finite element software specialized in

the non linear analysis of seismic structures.

The developed models have been validated by comparison with experimental results available in literature. The models were validated both individually and jointly. Validation included a wide range of concrete types with strengths between 11 and 80 MPa. Different cross-section geometries have been tested such as rectangular, circular, triangular and box sections. Several materials and arrangements for the longitudinal and transverse reinforcement have been reproduced with the proposed models. A wide range of loading conditions have been simulated: elements in pure shear, coupled torsion and bending moments, coupled axial, shear and bending in both monotonic and cyclic conditions.

The incremental dynamic analysis of a real bridge has been made to study the capabilities of the proposed model to simulate the response of full scale structures.

6.2 General conclusions

The numerical model developed in this research is robust. This was demonstrated as it is able to reproduce different complex failure modes and other important physical phenomena such as confinement, without recalibration of sectional and material parameters. The sectional model demonstrated to be efficient, as it reduces significantly the degrees of freedom involved in the sectional analysis compared to a finite element solution.

The possibility to incorporate different sectional models of different order within the same frame element allows to optimize the computational effort. This is of special interest on elements where the nonlinear behavior is concentrated on zones that can be identified before the analysis such as columns or beams in seismic buildings and bridges.

The joint use of a sectional model, capable of capturing the interaction between the different components of the cross-section, with a constitutive model that reproduces variable dilatancy has prove essential to accurately simulate complex phenomena such as

shear and torsional failures.

Confinement has been reproduced in a rational way without defining confined zones in a cross-section domain and without recalibration of material parameters. This enables an objective representation of confinement phenomenon which is important in the design and assessment of structures. This represents one of the main contributions of this work.

The sectional model developed in this thesis, is general and can be used with generic geometries and materials. Furthermore, the constitutive plastic-damage model with variable dilatancy for concrete can be used on any three-dimensional finite element model. Thus, both models constitute independently original contributions of this thesis.

The study of beams failing with different modes such as shear and bending, as wells as the simulation for cyclic columns has demonstrated that the developed models are suitable for the simulation of critical elements of structures thanks to their ability to reproduce multiple failure modes.

The simulation of a full-scale real bridge under seismic loads of different intensity showed the capabilities and potential of the developed model. It has been demonstrated that the model captures additional information compared with traditional models, such as shear deformations, transverse reinforcements stress and strains, among others. This information can be used in the design of new structures and improve decision process in the assessment and repair of existing structures.

At the end of this research it is considered that both the general and specific objectives stated in section 1.2 were achieved.

6.3 Specific conclusions

The specific conclusions obtained on each stage of this work are described in the following.

- The constitutive model presented in this work incorporates the variability of the dilatancy and friction angle parameters

as explicit functions of the plastic-damage and stress states. This function produces the maximum dilatancy for uniaxial compression and pure shear states. The resulting dilatancy is automatically reduced when the confinement stresses increase. It is demonstrated that a constant value of the dilatancy parameter is not adequate to accurately predict the free expansion of concrete.

- The new concrete model shows to be capable of accurately trace the volumetric expansion of concrete in uniaxial compressive tests including softening and confinement. It is also shown to be capable of capturing the enhancement in strength and ductility when passive confinement is applied by means of different confining materials. Good estimation of concrete shear strength and softening behavior is obtained. The model response is objective on different modes of failure with the same material parameters.

- The adequate control of the dilatant behavior of concrete is shown to be of paramount importance as it controls the volumetric expansion and, consequently, affects the strength and ductility of confined concrete as well as the shear strength and softening.

- The sectional model presented in this thesis is based on the displacement decomposition. The complementary field which is obtained by considering explicitly the inter-fiber equilibrium, allows the calculation of the complete stress and strain tensors on each point of the cross-section domain. Furthermore, it is able to trace the complete coupling between all the internal forces.

- The cross-sectional model considers a displacement field independent of the beam-axis coordinate, which allows the formulation of a completely local model, which can be used as a cross-section constitutive model on each integration point

of any standard frame formulation without the need of additional degrees of freedom at the frame level.

- The b-spline numerical solution produces a remarkable reduction in the degrees of freedom involved in the solution compared with the FE model. This enabled the model to have significant speedups proving its lower computational demand with respect to the FE solution.

- The sectional model is used to study confinement in reinforced concrete sections. As the formulation considers the distortion of the section, it is able to capture the interaction of transverse reinforcements and the concrete mass. Then confinement is simulated in an objective manner for different confining materials, section shape and reinforcement arrangements.

- The force-based element and the object oriented structure of the FE software allows the use of different sectional models on the integration points, the framework gives the user the flexibility to use the more refined sectional model only where coupling between the internal forces is more important or where local sectional information is needed.

- The frame element with the sectional and constitutive models is a suitable tool for large scale simulations of structures under general loading and can be used in the assessment of building and bridges as well as in reliability analyses.

6.4 Recommendations for future research

The present research work has opened several possibilities for future studies. Some of these are summarized in the following:

- To use the sectional and constitutive models developed to train artificial neural networks (ANN) that approximate the sectional behavior of typical cross-sectional geometries. The ANN could be used as a replacement of the sectional model

reducing even more the computational cost for typical cases such as rectangular or circular sections.

- To use the developed models to study in detail the effect of shear and torsional forces in seismic structures. Furthermore, based on this study, new approaches and practical methodologies could be developed for the design and assessment of structures.

- To incorporate in a consistent way other physical phenomena that affects the behavior reinforced concrete elements such as bar buckling and bond-slip. In addition, the effect of debonding could be incorporated to improve the simulation of elements reinforced by composite materials.

- To incorporate on the sectional formulation surface loads on the cross sectional domain. In this way, the model will be able to reproduce the effect of distributed and hanging loads.

- To develop a solid element to simulate discontinuity regions, such as joints or load concentration zones, that is compatible with the developed models and that can be used on the simulation of three-dimensional frame structures.

- To incorporate on the sectional formulation the variation of warping and distortion on the beam axis. In this way, the model will be able to reproduce shear-lag and non-uniform warping phenomena.

- To study the behavior of full scale structure making emphasis on repaired structures by means of advanced materials such as composite materials and shape-memory alloys.

- To use the developed sectional model with composite and orthotropic materials to study the behavior of typical aeronautical cross-sections

- To develop experimental test that will allow the improvement and extension of the constitutive model, in particular on the

dilatancy control. This could be done by means of uniaxial tests under different confining pressures measuring the transverse expansion.

- To study and extend the plastic-damage model to simulate high and ultra-high performance concretes.
- To use the constitutive model in two and three-dimensional finite element simulations to study different complex phenomena such as aggregate interlock and shear size-effect.
- To use the developed element to perform full probabilistic analyses of structures and reliability studies. The robustness of the model and its reduced computational demand make the model suitable for the large amount of simulation required in a full probabilistic approach.

Bibliography

AASHTO . Guide Specification for LRFD Seismic Bridge Design, 2nd Edition. Washington, DC: American Association of State Highway and Transportation Officials, 2011.

ABAQUS . Theory Manual Version 6.12 // Abaqus Documentation. 2012.

ACI Committee 318 . Building code requirements for structural concrete : (ACI 318-14) ; and commentary (ACI 318R-14). Farmington Hills: American Concrete Institute, 2014.

ACI Committee 341 . ACI 341.3R07: Seismic Evaluation and Retrofit Techniques for Concrete Bridges. Farmington Hills: American Concrete Institute, 2007.

Aire C. Estudio experimental del comportamiento del hormigón confinado sometido a compresión. Departament D'Enginyeria de la Construcció, Universitat Politècnica de Catalunya, Barcelona, 2002.

Alejano L.R., Alonso E. Considerations of the dilatancy angle in rocks and rock masses // International Journal of Rock Mechanics and Mining Sciences. 2005. 42, 4. 481 – 507.

Alfarah B., López-Almansa F., Oller S. New methodology for calculating damage variables evolution in Plastic Damage Model for RC structures // Engineering Structures. 2017. 132. 70 – 86.

Bažant Zdeněk P., Gambarova Pietro G. Crack Shear in Concrete: Crack Band Microplane Model // Journal of Structural Engineering. 1984. 110, 9. 2015–2035.

Bairán Jesus Miguel, Marí Antonio R. Coupled model for the non-linear analysis of anisotropic sections subjected to general 3D loading. Part 1: Theoretical formulation // Computers & Structures. 2006a. 84, 31. 2254 – 2263.

Bairán Jesus Miguel, Marí Antonio R. Coupled model for the nonlinear analysis of sections made of anisotropic materials, subjected to general 3D loading. Part 2: Implementation and validation // Computers & Structures. 2006b. 84, 31. 2264 – 2276.

Bairán Jesus Miguel, Marí Antonio R. Multiaxial-coupled analysis of RC cross-sections subjected to combined forces // Engineering Structures. 2007a. 29, 8. 1722 – 1738.

Bairán Jesus Miguel, Marí Antonio R. Shear-Bending-Torsion Interaction in Structural Concrete Members: A Nonlinear Coupled Sectional Approach // Archives of Computational Methods in Engineering. Sep 2007b. 14, 3. 249–278.

Balduzzi Giuseppe, Morganti Simone, Füssl Josef, Aminbaghai Mehdi, Reali Alessandro, Auricchio Ferdinando. Modeling the non-trivial behavior of anisotropic beams: A simple Timoshenko beam with enhanced stress recovery and constitutive relations // Composite Structures. 2019. 229. 111265.

Bazant Zdenek P. Instability, ductility, and size effect in strain-softening concrete // Journal of Engineering Mechanics - ASCE. 1 1976. 102, 2. 331–344.

Bažant Zdeněk P, Oh Byung H. Crack band theory for fracture of concrete // Matériaux et construction. 1983. 16, 3. 155–177.

Bazant Zdensk P. Comment on orthotropic models for concrete and geomaterials // Journal of Engineering Mechanics - ASCE. 1 1983. 109, 3. 849–865.

Bentz E. Sectional analysis of reinforced concrete members. University of Toronto, Toronto, 2000.

Bisby Luke, Dent A.J.S., Green Mark. Comparison of Confinement Models for Fibre-Reinforced Polymer-Wrapped Concrete // ACI Structural Journal. 01 2005. 102. 62–72.

CALTRANS . Seismic Design Criteria Ver.2.0. Sacramento, CA: State of California Department of Transportation, 2019.

CEB-FIB . Model Code 2010. London: Thomas Telford, 2010.

Carol I., Murcia J. Nonlinear time-dependent analysis of planar frames using an 'exact' formulation—I. Theory // Computers & Structures. 1989. 33, 1. 79 – 87.

Ceresa P., Petrini L., Pinho R., Sousa R. A fibre flexure–shear model for seismic analysis of RC-framed structures // Earthquake Engineering & Structural Dynamics. 2009. 38, 5. 565–586.

Ceresa Paola, Petrini Lorenza, Pinho Rui. Flexure-Shear Fiber Beam-Column Elements for Modeling Frame Structures Under Seismic Loading — State of the Art // Journal of Earthquake Engineering. 2007. 11, sup1. 46–88.

Chen W.F. Plasticity in Reinforced Concrete. J. Ross Pub., 2007. (J. Ross Publishing Classics).

Coleman J, Spacone Enrico. Localization Issues in Force-Based Frame Elements // Journal of Structural Engineering. 2001. 127, 11. 1257–1265.

De Boor Carl. A practical guide to splines; rev. ed. Berlin: Springer, 2001. (Applied mathematical sciences).

Detournay Emmanuel. Elastoplastic model of a deep tunnel for a rock with variable dilatancy // Rock Mechanics and Rock Engineering. Apr 1986. 19, 2. 99–108.

Di Re P. 3D beam-column finite elements under tri-axial stress-strain states: non-uniform shear stress distribution and warping. Department of Structural and Geotechnical Engineering, Università la Sapienza, Roma, 2017.

EN CEN . EN 1992-1-1 Eurocode 2: Design of concrete structures - Part 1-1: General ruels and rules for buildings. Brussels: Comité Européen de Normalisation, 2005.

Earij Alrazi, Alfano Giulio, Cashell Katherine, Zhou Xiangming. Nonlinear three–dimensional finite–element modelling of reinforced–concrete beams: Computational challenges and experimental validation // Engineering Failure Analysis. 2017. 82. 92 – 115.

Elwi Alaa A, Murray David W. A 3D hypoelastic concrete constitutive relationship // Journal of the Engineering Mechanics Division. 1979. 105, 4. 623–641.

FEMA . P-58: Seismic Perfomance Assesment of Buildings. Washington, DC: Federal Emergency Management Agency, 2018.

Faria Rui, Oliver Javier, Cervera Miguel. Modeling Material Failure in Concrete Structures under Cyclic Actions // Journal of Structural Engineering. 2004. 130, 12. 1997–2005.

Farin Gerald E. NURBS: From Projective Geometry to Practical Use. Natick, MA, USA: A. K. Peters, Ltd., 1999. 2nd.

Fenves Gregory L, Filippou Filip C. Methods of analysis for earthquake-resistant structures // Earthquake Engineering. 2004. 332–410.

Filippou Filip C, Bertero Vitelmo Victorio, Popov Egor P. Effects of bond deterioration on hysteretic behavior of reinforced concrete joints. Report EERC 83-19, Earthquake Engineering Research Center, University of California Berkeley, 1983.

Genikomsou Aikaterini S., Polak Maria Anna. Finite element analysis of punching shear of concrete slabs using damaged plasticity model in ABAQUS // Engineering Structures. 2015. 98. 38 – 48.

Gregori J Navarro, Sosa P Miguel, Prada MA Fernández, Filippou Filip C. A 3D numerical model for reinforced and prestressed concrete elements subjected to combined axial, bending, shear and torsion loading // Engineering Structures. 2007. 29, 12. 3404–3419.

Höllig Klaus, Hörner Jörg. Programming finite element methods with weighted B-splines // Computers & Mathematics with Applications. 2015. 70, 7. 1441 – 1456. High-Order Finite Element and Isogeometric Methods.

Hsu Thomas Tseng Chuang. Torsion of reinforced concrete. New York: Van Nostrand Reinhold, 1984.

Huang Xu, Kwon Oh-Sung. Numerical models of RC elements and their impacts on seismic performance assessment // Earthquake Engineering & Structural Dynamics. 2015. 44, 2. 283–298.

Hughes T.J.R., Cottrell J.A., Bazilevs Y. Isogeometric analysis: CAD, finite elements, NURBS, exact geometry and mesh refinement // Computer Methods in Applied Mechanics and Engineering. 2005. 194, 39. 4135 – 4195.

Hughes Thomas J.R., Evans John A., Reali Alessandro. Finite element and NURBS approximations of eigenvalue, boundary-value, and initial-value problems // Computer Methods in Applied Mechanics and Engineering. 2014. 272. 290 – 320.

Ibarra Luis F., Medina Ricardo A., Krawinkler Helmut. Hysteretic models that incorporate strength and stiffness deterioration // Earthquake Engineering & Structural Dynamics. 2005. 34, 12. 1489–1511.

Kagermanov Alexander, Ceresa Paola. Fiber-Section Model with an Exact Shear Strain Profile for Two-Dimensional RC Frame

Structures // Journal of Structural Engineering. 2017. 143, 10. 04017132.

Kagermanov Alexander, Ceresa Paola. 3D Fiber-Based Frame Element with Multiaxial Stress Interaction for RC Structures // Advances in Civil Engineering. 2018. 2018.

Kang Young-Jin, Scordelis Alexander C. Nonlinear analysis of prestressed concrete frames // Journal of the structural division. 1980. 106, ASCE 15191.

Kani M. An experimental investigation of reinforced and prestressed beams in shear. University of Toronto,Toronto, 1977.

Karttunen Anssi T., Hertzen Raimo von. On the foundations of anisotropic interior beam theories // Composites Part B: Engineering. 2016. 87. 299 – 310.

Kolozvari Kristijan, Orakcal Kutay, Wallace John W. New opensees models for simulating nonlinear flexural and coupled shear-flexural behavior of RC walls and columns // Computers & Structures. 2018. 196. 246 – 262.

Le Corvec V. Nonlinear 3D frame element with multi-axial coupling under consideration of local effects. Department Civil and Environmental Engineering, University of California, Berkeley, 2012.

Lee Chin-Long. Hu-Washizu three-dimensional frame formulations including bond-slip and singular section response. University of California, Berkeley, 2008.

Lee Jeeho, Fenves Gregory L. Plastic-Damage Model for Cyclic Loading of Concrete Structures // Journal of Engineering Mechanics. 1998. 124, 8. 892–900.

Lee Jeeho, Fenves Gregory L. A return-mapping algorithm for plastic-damage models: 3-D and plane stress formulation // International Journal for Numerical Methods in Engineering. 2001. 50, 2. 487–506.

Lemaitre Jean. Coupled elasto-plasticity and damage constitutive equations // Computer Methods in Applied Mechanics and Engineering. 1985a. 51, 1. 31 – 49.

Lemaitre Jean. Coupled elasto-plasticity and damage constitutive equations // Computer methods in applied mechanics and engineering. 1985b. 51, 1-3. 31–49.

Li Zhong-Xian, Gao Ying, Zhao Qiuhong. A 3D flexure–shear fiber element for modeling the seismic behavior of reinforced concrete columns // Engineering Structures. 2016. 117. 372 – 383.

Lubliner J., Oliver J., Oller S., Oñate E. A plastic-damage model for concrete // International Journal of Solids and Structures. 1989. 25, 3. 299 – 326.

Luccioni B.M., Rougier V.C. A plastic damage approach for confined concrete // Computers & Structures. 2005. 83, 27. 2238 – 2256.

Luccioni Bibiana, Oller Sergio. A directional damage model // Computer Methods in Applied Mechanics and Engineering. 2003. 192, 9. 1119 – 1145.

Luccioni Bibiana, Oller Sergio, Danesi Rodolfo. Coupled plastic-damaged model // Computer Methods in Applied Mechanics and Engineering. 1996. 129, 1. 81 – 89.

Lynn Abraham C., Moehle Jack P., Mahin Stephen A., Holmes William T. Seismic Evaluation of Existing Reinforced Concrete Building Columns // Earthquake Spectra. 1996. 12, 4. 715–739.

Mander J. B., Priestley M. J. N., Park R. Observed Stress-Strain Behavior of Confined Concrete // Journal of Structural Engineering. 1988a. 114, 8. 1827–1849.

Mander J. B., Priestley M. J. N., Park R. Theoretical Stress-Strain Model for Confined Concrete // Journal of Structural Engineering. 1988b. 114, 8. 1804–1826.

Mari Antonio R. Nonlinear geometric, material and time dependent analysis of three dimensional reinforced and prestressed concrete frames. Department of Civil Engineering, University of California, 1984.

Marini Alessandra, Spacone Enrico. Analysis of reinforced concrete elements including shear effects // ACI Structural Journal. 2006. 103, 5. 645.

Martinez Xavier, Oller Sergio, Rastellini Fernando, Barbat Alex H. A numerical procedure simulating RC structures reinforced with FRP using the serial/parallel mixing theory // Computers & Structures. 2008. 86, 15. 1604 – 1618.

Mazars J., Kotronis P., Ragueneau F., Casaux G. Using multifiber beams to account for shear and torsion: Applications to concrete structural elements // Computer Methods in Applied Mechanics and Engineering. 2006. 195, 52. 7264 – 7281. Computational Modelling of Concrete.

Mazars Jacky. A description of micro- and macroscale damage of concrete structures // Engineering Fracture Mechanics. 1986. 25, 5. 729 – 737.

Mazars Jacky, Hamon François, Grange Stéphane. A new 3D damage model for concrete under monotonic, cyclic and dynamic loadings // Materials and structures. 2015. 48, 11. 3779–3793.

McKenna Frank, Scott Michael H., Fenves Gregory L. Nonlinear Finite-Element Analysis Software Architecture Using Object Composition // Journal of Computing in Civil Engineering. 2010. 24, 1. 95–107.

Micelli Francesco, Modarelli Rossella. Experimental and analytical study on properties affecting the behaviour of FRP-confined concrete // Composites Part B: Engineering. 2013. 45, 1. 1420 – 1431.

Moharrami Mohammadreza, Koutromanos Ioannis. Triaxial Constitutive Model for Concrete under Cyclic Loading // Journal of Structural Engineering. 2016. 142, 7. 04016039.

Mohr Steffen, Bairán Jesús M., Marí Antonio R. A frame element model for the analysis of reinforced concrete structures under shear and bending // Engineering Structures. 2010. 32, 12. 3936 – 3954.

Neuenhofer Ansgar, Filippou Filip C. Evaluation of Nonlinear Frame Finite-Element Models // Journal of Structural Engineering. 1997. 123, 7. 958–966.

Nguyen Tuan-Anh, Nguyen Quang-Huy, Somja Hugues. An enhanced finite element model for reinforced concrete members under torsion with consistent material parameters // Finite Elements in Analysis and Design. 2019. 167. 103323.

Nzabonimpa J.D., Hong Won-Kee, Kim Jisoon. Nonlinear finite element model for the novel mechanical beam-column joints of precast concrete-based frames // Computers & Structures. 2017. 189. 31 – 48.

Oliver J. A consistent characteristic length for smeared cracking models // International Journal for Numerical Methods in Engineering. 1989. 28, 2. 461–474.

Oller S., Oliver J., Lubliner J., Oñate E. Un modelo constitutivo de daño plástico para materiales friccionales. Parte I: Variables Fundamentales, funciones de fluencia y potencial // Revista Internacional de Métodos Numéricos para Cálculo y Diseño en Ingeniería. 1988. 4, 4. 397–431.

Omidi O., Lotfi V. and. Finite Element Analysis of Concrete Structures Using Plastic Damage Model in 3-D Implementation // International Journal of Civil Engineering. 2010. 8, 3.

Onsongo W.M. The diagonal compression field theory for reinforced concrete beams subject to combined torsion, flexure and axial load. University of Toronto, Toronto, 1978.

Osorio Edison, Bairán Jesús M., Marí Antonio R. Analytical modeling of reinforced concrete columns subjected to bidirectional shear // Engineering Structures. 2017. 138. 458 – 472.

Pantazopoulou S. J. Role of Expansion on Mechanical Behavior of Concrete // Journal of Structural Engineering. 1995. 121, 12. 1795–1805.

Pantazopoulou S. J., Mills R. H. Microstructural Aspects of the Mechanical Response of Plain Concrete // ACI Materials Journal. 1995. 92, 6.

Papachristidis Aristidis, Fragiadakis Michalis, Papadrakakis Manolis. A 3D fibre beam-column element with shear modelling for the inelastic analysis of steel structures // Computational Mechanics. 2010. 45, 6. 553–572.

Park Robert, Paulay Thomas. Reinforced Concrete Structures. New York: John Wiley & Sons, 1975.

Petrangeli Marco. Fiber element for cyclic bending and shear of RC structures. II: Verification // Journal of engineering mechanics. 1999. 125, 9. 1002–1009.

Petrangeli Marco, Pinto Paolo Emilio, Ciampi Vincenzo. Fiber element for cyclic bending and shear of RC structures. I: Theory // Journal of Engineering Mechanics. 1999. 125, 9. 994–1001.

Poliotti Mauro, Bairán Jesús-Miguel. A new concrete plastic-damage model with an evolutive dilatancy parameter // Engineering Structures. 2019. 189. 541 – 549.

Poliotti Mauro, Bairán Jesús-Miguel. B-spline sectional model for general 3D effects in reinforced concrete elements // Engineering Structures. 2020. 207. 110200.

Rahai AR, Sadeghian P, Ehsani MR. Experimental behavior of concrete cylinders confined with CFRP composites // The 14th World Conference on Earthquake Engineering. 2008. 12–17.

Rahjoo M., Eberhardt E. A Simplified Dilation Model for Modeling the Inelastic Behavior of Rock // American Rock Mechanics Association. 2016. 16, 760.

Rajapakse R.M.C.M., Wijesundara K.K., Nascimbene R., Bandara C.S., Dissanayake R. Accounting axial-moment-shear interaction for force-based fiber modeling of RC frames // Engineering Structures. 2019. 184. 15 – 36.

Ranzo Giulio, Petrangeli Marco. A fibre finite beam element with section shear modelling for seismic analysis of RC structures // Journal of Earthquake Engineering. 1998. 2, 3. 443–473.

Re Paolo Di, Addessi Daniela, Filippou Filip C. Mixed 3D Beam Element with Damage Plasticity for the Analysis of RC Members under Warping Torsion // Journal of Structural Engineering. 2018. 144, 6. 04018064.

Reddy J.N. On locking-free shear deformable beam finite elements // Computer Methods in Applied Mechanics and Engineering. 1997. 149, 1. 113 – 132. Containing papers presented at the Symposium on Advances in Computational Mechanics.

Reddy J.N., Wang C.M., Lee K.H. Relationships between bending solutions of classical and shear deformation beam theories // International Journal of Solids and Structures. 1997. 34, 26. 3373 – 3384.

Roca P., Molins C., Barbat H. A. Una formulación matricial generalizada. Parte 2: Análisis dinámico // Revista Internacional de Métodos Numéricos para Cálculo y Diseño en Ingeniería. 1995. 11, 1. 23–36.

Roca P., Molins C., Marí A. R. Una formulación matricial generalizada: 1-Análisis estático // Revista Internacional de Métodos

Numéricos para Cálculo y Diseño en Ingeniería. 1994. 10, 4. 317–339.

Saritas Afsin. Mixed formulation frame element for shear critical steel and reinforced concrete members. University of California, Berkeley, 2006.

Saritas Afsin, Filippou Filip C. Inelastic axial-flexure–shear coupling in a mixed formulation beam finite element // International Journal of Non-Linear Mechanics. 2009a. 44, 8. 913–922.

Saritas Afsin, Filippou Filip C. Numerical integration of a class of 3d plastic-damage concrete models and condensation of 3d stress–strain relations for use in beam finite elements // Engineering Structures. 2009b. 31, 10. 2327 – 2336.

Scott M. H., Hamutçuoğlu O. M. Numerically consistent regularization of force-based frame elements // International Journal for Numerical Methods in Engineering. 2008. 76, 10. 1612–1631.

Scott Michael H., Fenves Gregory L. Plastic Hinge Integration Methods for Force-Based Beam-Column Elements // Journal of Structural Engineering. 2006. 132, 2. 244–252.

Scott Michael H., Fenves Gregory L., McKenna Frank, Filippou Filip C. Software Patterns for Nonlinear Beam-Column Models // Journal of Structural Engineering. 2008. 134, 4. 562–571.

Scott Michael H., Franchin Paolo, Fenves Gregory L., Filippou Filip C. Response Sensitivity for Nonlinear Beam-Column Elements // Journal of Structural Engineering. 2004. 130, 9. 1281–1288.

Simo Juan C., Ju Jiann-Wen, Pister Karl S., Taylor Robert L. Assessment of Cap Model: Consistent Return Algorithms and Rate-Dependent Extension // Journal of Engineering Mechanics. 1988. 114, 2. 191–218.

Spacone E., Ciampi V., Filippou F.C. Mixed formulation of nonlinear beam finite element // Computers & Structures. 1996a. 58, 1. 71 – 83.

Spacone E., Filippou F. C., Taucer F. F. Fibre beam column model for non-linear analysis of R/C frames: Part I. Formulation // Earthquake Engineering & Structural Dynamics. 1996b. 25, 7. 711–725.

Taucer F.F., Spacone E., Filippou F.C. A fiber beam-column element for seismic response analysis of reinforced concrete structures. 91, 17. Earthquake Engineering Research Center, 1991.

Taylor RL, Filippou FC, Saritas A, Auricchio F. A mixed finite element method for beam and frame problems // Computational mechanics. 2003. 31, 1-2. 192–203.

Timoshenko S.T., Goodier J.N. Teoría de la elasticidad (Theory of elasticity). Ed. Urmo, Bilbao, 1972. 549.

Uy B. Strength of short concrete filled high strength steel box columns // Journal of Constructional Steel Research. 2001. 57, 2. 113 – 134.

Vecchio F., Collins M.P. The response of reinforced concrete to in-plane shear and normal stresses. Department of Civil Engineering, University of Toronto, 1982.

Vecchio F. J., Shim W. Experimental and Analytical Reexamination of Classic Concrete Beam Tests // Journal of Structural Engineering. 2004. 130, 3. 460–469.

Vecchio F.J., Collins M.P. Predicting the response of reinforced concrete beams subjected to shear using the modified compression field theory // ACI Structural J. 1988. 85, 3. 258 – 268.

Vecchio FJ, Selby RG. Toward compression-field analysis of reinforced concrete solids // Journal of Structural Engineering. 1991. 117, 6. 1740–1758.

Vecchio Frank J. Finite element modeling of concrete expansion and confinement // Journal of Structural Engineering. 1992. 118, 9. 2390–2406.

Vecchio Frank J. Towards cyclic load modeling of reinforced concrete // ACI Structural Journal. 1999. 96. 193–202.

Vecchio Frank J, Collins Michael P. The modified compression-field theory for reinforced concrete elements subjected to shear. // ACI J. 1986. 83, 2. 219–231.

Vermeer P.A., de Borst R. Non associated plasticity for soils, concrete and rock // Heron. 1983. 29, 3. 1–64.

Wei Xiaodong, Zhang Yongjie, Liu Lei, Hughes Thomas J.R. Truncated T-splines: Fundamentals and methods // Computer Methods in Applied Mechanics and Engineering. 2017. 316. 349 – 372. Special Issue on Isogeometric Analysis: Progress and Challenges.

Wu Jian Ying, Li Jie, Faria Rui. An energy release rate-based plastic-damage model for concrete // International Journal of Solids and Structures. 2006. 43, 3. 583 – 612.

Wu Yu-Fei, Jiang Jia-Fei. Effective strain of FRP for confined circular concrete columns // Composite Structures. 2013. 95. 479 – 491.

Zhao X.G., Cai M. A mobilized dilation angle model for rocks // International Journal of Rock Mechanics and Mining Sciences. 2010. 47, 3. 368 – 384.

Červenka Jan, Papanikolaou Vassilis K. Three dimensional combined fracture–plastic material model for concrete // International Journal of Plasticity. 2008. 24, 12. 2192 – 2220.